PONTIFICIA UNIVERSIDAD CATOLICA DE CHILE
SCHOOL OF ENGINEERING

POINT-SPREAD FUNCTION RECONSTRUCTION AT NICI ADAPTIVE OPTICS SYSTEM

RODRIGO OLGUIN MUÑOZ

Thesis submitted to the Office of Research and Graduate Studies
in partial fulfillment of the requirements for the degree of
Master of Science in Engineering

Supervisor:
ANDRES GUESALAGA

Santiago de Chile, August 2014

PONTIFICIA UNIVERSIDAD CATOLICA DE CHILE
SCHOOL OF ENGINEERING

POINT-SPREAD FUNCTION RECONSTRUCTION AT NICI ADAPTIVE OPTICS SYSTEM

RODRIGO OLGUIN MUÑOZ

Members of the Committee:
ANDRES GUESALAGA
DANI GUZMAN
MARKUS HARTUNG
JOSE MIGUEL CEMBRANO

Thesis submitted to the Office of Research and Graduate Studies
in partial fulfillment of the requirements for the degree of
Master of Science in Engineering

Santiago de Chile, August 2014

Ever obliged to Vanessa and my family

ACKNOWLEDGEMENTS

First, my sincere gratitude towards my advisor and mentor Prof. Andres Guesalaga for his patience, trust and granting me the golden opportunity to undertake this challenging endeavor. His unrestricted support and motivation- especially during hard times- was what truly allowed me to reach the end of this adventure. Besides my advisor, I want to thank Dr.Markus Hartung who kindly taught me the first secrets of PSF reconstruction and guided me along my research process; and Dr. Thomas Hayward who took the time to recover datasets from tape and sat to discuss the results with me. Special thanks to Prof. Dani Guzman who supported me throughout my courses, also giving me germane advice from time to time. My gratitude towards the Professors from the Department of Electrical Engineering who understood my absences when having to leave to work in ALMA. None of all this strenuous effort would have been possible without my moral and spiritual support, my beloved Vanessa. My deep and utmost gratitude to her for her everlasting patience, for staying with me through every moment and for her infinite love. Lastly, my deepest thanks to my mother for all the sacrifices she did for me and to my family as well.

TABLE OF CONTENTS

LIST OF FIGURES

LIST OF TABLES

ABSTRACT

In order to achieve the current scientific goals on astronomy - such as the study of star formation, the detection of exoplanets, or the discovery of Earth like planets - a new generation of extremely large telescopes (ELTs) is currently being developed. Such telescopes need to be capable of generating diffraction-limited images. In view of the aforementioned, they will be equipped with Adaptive Optics (AO) systems which will correct the phase perturbations caused by turbulences in the atmosphere and that affect the angular resolution of the telescope's imaging system. Notwithstanding, the correction provided by AO systems is not perfect; therefore, image post-processing techniques based on deconvolution with the system point-spread function (PSF), are needed to acquire the diffraction-limited image. PSF reconstruction is one of the procedures aimed to solve the problem of getting an accurate estimation of the long exposure PSF associated to the AO observation. This is done by processing the AO phase measurements, and the AO phase correction commands to characterize the atmosphere turbulence and estimate the atmosphere Optical Transfer Function (OTF); which multiplied by the telescope OTF, provides the system OTF for an observation. The long exposure PSF is obtained from the inverse Fourier transform of the system OTF. This thesis explores the real world implementation of the point-spread function reconstruction algorithm applied to the Near-Infrared Coronographic Imager (NICI) that is currently operative at the Gemini South Telescope.

The results presented in this thesis show consistency on the estimation of the Fried parameter r_0 and the long exposure PSF for each observation. The Long Exposure PSF estimation accuracy is $\sim 95\%$ for bright stars, which allows diffraction limited imaging using deconvolution correction.

Keywords: Point-Spread Function, PSF, reconstruction, Adaptive, Optics, Algorithm, NICI, Gemini..

RESUMEN

Para lograr las metas científicas actuales de la astronomía, tales como el estudio de estrellas en formación, la detección de exoplanetas o el descubrimiento de gemelos del planeta Tierra, una nueva generación de telescopios extremadamente grandes esta siendo desarrollada. Estos telescopios debe ser capaces de proveer imágenes en límite de difracción. Para este propósito ellos estarán equipados con sistemas de óptica adaptativa que corregirán las perturbaciones de fase causados por las turbulencias atmosféricas y que afectan la resolución angular del sistema de imágenes del telescopio. Sin embargo, la corrección entregada por el sistema de óptica adaptativa no es perfecta y técnicas de post-procesamiento de imágenes son necesarias para obtener imágenes en límite de difracción. La reconstrucción de la función de dispersión de punto es una de las técnicas desarrolladas con este propósito. Este trabajo de tesis explorara la implementación de un algoritmo especifico de reconstrucción de la función de dispersión de punto basado en los datos de telemetría del sistema de óptica adaptativa colectados durante observaciones y entregara la implementación para un caso del mundo real, aplicando el algoritmo al Near-Infrared Coronographic Imager que se encuentra en operaciones en el telescopio Gemini Sur.

Los resultados obtenidos muestran consistencia en la estimación del parámetro de Fried r_0 y en la PSF de larga exposición para cada observación. La precisión de la estimación de la PSF de larga exposición es $\sim$ 95%, lo que permite imagenes en límite de difracción utilizando deconvolución.

Palabras Claves: Función de dispersión de punto, PSF, reconstrucción, Adaptativa, Óptica, Algoritmo, NICI, Gemini..

1. INTRODUCTION

A new generation of extremely large telescopes (ELTs) is being or will be constructed in the coming years. Members of this list, among others, are the Giant Magellan Telescope (GMT), with a 24.5-meter primary mirror (Johns et al., 2012); the Thirty Meter Telescope (TMT) (Stepp, 2012); and the European Extremely Large Telescope (E-ELT) with a 39-meter diameter aperture (Liske et al., 2012). These gigantic instruments will offer a sensitivity and angular resolution level never seen before by the astronomy community, which will allow the imaging and study of the universe on a totally new scale (Vazquez et al., 2010). There are many scientific drives that justify the construction of these large instruments. For the last two decades, the detection of exoplanets and planetary systems has been possible; however, these detections are limited to Jupiter-size and Uranus-size objects. Today, the limits have to be pushed beyond to make possible the detection of rocky planets with the size of the earth; also to be able to study the possibility of life in an earth-twin, and know the composition of its atmosphere (Perryman et al., 2005). Another science driver is the study of star and planet formation, including its chemical composition; and the formation of galaxies, that will help to understand how life is originated and how the universe has developed from the big bang to the present time (Jacoby et al., 2012). For these purposes, the universe boundaries have to be explored, meaning the observation of small and faint objects in the sky. The study of fundamental physics, the understanding of dark matter; dark energy and the accelerating expansion of the universe are also investigating subjects that will be possible with ELTs (Sweeney, 2012). In order to achieve all these scientific targets, telescopes must operate on diffraction limited imaging.

1.1. Diffraction limited imaging in astronomy

The resolution of ground-based telescopes is dramatically limited by atmospheric turbulence, as a solution to this problem Adaptive Optics (AO) appears to allow diffraction limited imaging and obtain the usage of the resolution offered by the telescope (Glindemann et al., 2000). Present and future AO systems aim for the correction of atmospheric turbulence over a large field of view combined with large sky coverage (Simard et al., 2012). AO systems have proved to play a critical role in the acquisition of diffraction limited images; nevertheless the correction they can provide is partial, and thus the long exposure image is affected by a residual blur which reduces the contrast of the fine details. However, these images obtained with AO systems can be improved using restoration techniques (Gal et al., 2014), but they require an accurate knowledge of the Point-Spread Function (PSF) associated with each observation.

1.2. Existing Techniques/Existing Approaches

Image blur removing techniques are mainly based on a deconvolution of the image with a known, estimated or guessed PSF. For astronomy, the range of available methods is limited due to the unique characteristics of telescopes and AO systems.

1.2.1. General methods

The methods for AO image residual blur correction aim to determine the fine detail structure of the PSF system, and then deconvolve the long exposure image or a set of short exposure images if they are available. The following methods are currently used:

- Imaging the AO guide star as a point source is the simplest way to characterize the PSF of a telescope with an AO system; however, this method is not very efficient. The obtained PSF is not synchronized with the acquisition of the science image and is not representative of the local conditions of the atmosphere during the observation; additionally this process wastes telescope observation time (Sheehy et al., 2006).
- Compensated speckle holography or compensated deconvolution from wavefront sensing is usable when a set of short exposure images, which makes the long exposure image, is available. This method uses AO wavefront sensor measurements to make corrections on each short exposure image and improves the integrated long exposure image (Schodel et al., 2013).

- Long exposure PSF estimation or PSF reconstruction for AO telemetry data is a more recent technique; first proposed and tested around 15 years ago. This method covers the case when speckle holography is not applicable because only the long exposure image is available. It uses data obtained from the wavefront sensor (WFS) measurements, and the commands for the deformable mirror during the observation. This method does not require extra observing time; however a deep characterization of the system has to be done, which is in many cases a problem for its implementation in observatories. This technique has become critical for diffraction limited science (Exposito et al., 2013).
- Blind/myopic deconvolution techniques, where a PSF is assumed and applied to the image with typical deconvolution algorithms to find whether the image was improved or not (Tian et al., 2009).

1.3. Summary of Contributions/Original Contributions

The main contributions of this thesis are:

- The improvements to the PSF estimation done by APETy (A PSF Estimation Tool for Yorick) through finding the sources of error and implementing a filtered phase screen method for evaluating the high order phase contributions to the long exposure PSF.
- Implementation of the PSF reconstruction algorithm for a real instrument as NICI, the Near-Infrared Coronograph Imager.
- Analysis of the effect of the AO loop gain in the estimation of r_0 and the PSF.
- Test of the V_{ii} method (Gendron et al., 2006) for reducing the PSF reconstruction time.
- Evaluate the impact of non common-path aberrations in the PSF estimation.

1.4. Thesis Outline/Document Organization

This thesis is organized in a way that the PSF reconstruction algorithm can be progressively assimilated. In chapter 2, a full review of the theoretical fundaments behind PSF reconstruction is given; starting with the scalar diffraction theory, the definition of the PSF and the OTF. An explanation is presented for the electromagnetic wave propagation through turbulent atmosphere and Kolmogorov's atmospheric turbulence theory. The effects of the atmosphere on astronomical imaging and the introduction of the Adaptive Optics theory are discussed. Finally, deconvolution and J.P. Veran's algorithm for PSF reconstruction (Véran, Rigaut, Maître, & Rouan, 1997) are explained in detail. Chapter 3 presents a survey in the complete history of PSF reconstruction from its first proposal to present days. Chapter 4 shows the case studied in this thesis with the implementation of the PSF Reconstruction algorithm for NICI. Chapter 5 presents conclusions, future work and future perspectives for PSF Reconstruction.

2. THE POINT SPREAD FUNCTION AND PSF RECONSTRUCTION

2.1. Overview on Systems and Signals

The general concepts of signal analysis and linear systems are widely covered in literature; please refer to Allen and Mills (2004) and Hespanha (2009) for a complete revision of the theory.

The abstract notion of taking an input signal, performing an operation on it, and obtaining an output is called a system.

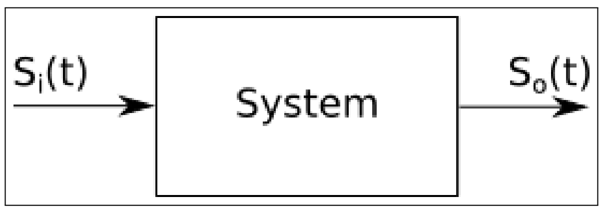

FIGURE 2.1. System block diagram.

A system can be described by the way it transforms or maps an input signal into an output signal. From figure 2.1, considering $S_i(t)$ the input signal entering the system and $S_o(t)$ the output signal from the system, then:

$$S_o(t) = H\{S_i(t)\} \tag{2.1}$$

with $H\{\bullet\}$ being the transformation function applied by the system that maps the input to the output.

2.1.1. Linear and time-invariant systems

A system is linear if having 2 input signals $S_{i1}(t)$, $S_{i2}(t)$ such that:

$$S_{o1}(t) = H\{S_{i1}(t)\}, S_{o2}(t) = H\{S_{i2}(t)\}$$

Then:

$$\alpha S_{o1}(t) + \beta S_{o2}(t) = H\{\alpha S_{i1}(t) + \beta S_{i2}(t)\} \tag{2.2}$$

where α and β are scalars.

Also a system is time-invariant if:

$$S_o(t-\tau) = H\{S_i(t-\tau)\} \tag{2.3}$$

for every $\tau > 0$.

A system that is both linear and time-invariant is called an LTI system.

2.1.2. Unit impulse function

The Dirac delta function or unit impulse function may well be regarded as the idealization of a very narrow pulse with unit area. Defining the finite pulse $x(t)$ as:

$$x(t) = \begin{cases} \frac{1}{a} & \text{if } \frac{-a}{2} < t < \frac{a}{2} \\ 0 & \text{otherwise} \end{cases} \tag{2.4}$$

The impulse function can be defined as:

$$\delta(t) = \lim_{a \to \infty} x(t) \tag{2.5}$$

$\delta(t)$ satisfies:

$$\begin{gathered} \int_{-\infty}^{\infty} \delta(t) dt = 1 \\ \delta(t) = 0 \text{ for every } t \neq 0, \end{gathered} \tag{2.6}$$

$\delta(t)$ has the shifting property given by:

$$\int_{t_1}^{t_2} \delta(t-\tau)h(\tau)dt = \int_{t_1}^{t_2} \delta(\tau-t)h(\tau)d\tau = h(t) \tag{2.7}$$

where $h(t)$, a given function, is continuous at $\tau = t$, and $t_1 < t < t_2$.

2.1.3. Impulse Response

Let H be an LTI system and $\delta(t)$ be the Dirac delta function. Then the impulse response of H is

$$h(t) = H\{\delta(t)\} \tag{2.8}$$

For any LTI system the following relationship applies:

$$S_o(t) = S_i(t) * h(t) \tag{2.9}$$

Where the $*$ operator represents the convolution process defined as:

$$(x * h)(t) = \int_{-\infty}^{\infty} x(\tau)h(t-\tau)d\tau \tag{2.10}$$

The output signal of a system can be estimated for every possible input by knowing the impulse response.

2.1.4. Optical Imaging systems

The following definition for optical imaging is found in Born and Wolf (1970):

> Consider the propagation of light from a point source situated at P_0 in a medium specified by a refractive index function $n(x, y, z)$. An infinite number of rays will then proceed from P_0, but in general only a finite number will pass through any other point of the medium. In special cases, however, a point P_1 may be found through which an infinity of rays pass. Such a point P_1 is said to be a *stigmatic* (or a *sharp*) image of P_0.

> In an ideal optical instrument every point P_0 of a three-dimensional region, called the *object space*, will give rise to a stigmatic image P_1. The totality of the image points defines the *image space*. The corresponding points in the two spaces are said to be *conjugate points*. In general not all the rays which proceed from P_0 will reach the image space. Those rays which reach the image space will be said *to lie in the field of the instrument*. When P_0 describes a curve C_0 in the object space, P_1 will describe a conjugate curve C_1. The two curves will not necessarily be geometrically similar to each other.

In general, an optical imaging system will map the electric field spatial distribution in the object space by detecting the time average of the intensity in the image space.

2.2. Review on propagation of light and diffraction theory

This section introduces some preliminary notions and mathematical background on the propagation of light and the scalar diffraction theory. The presented contents are extracted from Glindeman (2011), Kenyon (2008) and Ersoy (2007). For a detailed discussion and mathematical deductions please refer to Born and Wolf (1970) and Goodman (2005).

2.2.1. Basic Properties of the Electromagnetic Wave

The wave theory of electromagnetic radiation, including light, was put on a sound theoretical basis around 1864 by Maxwell. It emerged that ray optics works in everyday situations because the wavelength of light is very small compared to everyday objects. The fundamental equations treating the propagation of electromagnetic waves are the *Maxwell's equations*. They describe the propagation of both the electric and the magnetic field vectors $\boldsymbol{E}$ and $\boldsymbol{H}$, respectively, through coupled partial differential equations. The simplest electromagnetic wave is a *plane wave* traveling in what we can define to be the z-direction.

The electric field vector $\boldsymbol{E}$ of the electromagnetic wave is a function of space and time. Assuming a monochromatic plane wave in vacuum propagating in the z-direction, the x-component of $\boldsymbol{E}$ can be written as:

$$E_x = E_{x0} cos(\omega t - kz) \tag{2.11}$$

with $\omega = 2\pi\nu$, time t, and $k = 2\pi/\lambda$, where ν is the frequency, λ is the wavelength and E_{x0} is the amplitude of the monochromatic wave. The y-component of $\boldsymbol{E}$ can be described in the same way.

For propagation in isotropic media the magnetic field $\boldsymbol{H}$ could be used just as well $\boldsymbol{E}$ to describe the electromagnetic wave.

The flow of energy in an electromagnetic wave is the energy crossing unit area per unit time perpendicular to the wave direction. It is therefore a vector quantity, called the Poynting vector given by $\boldsymbol{S} = \boldsymbol{E} \times \boldsymbol{H}$.

The Poynting vector oscillates with twice the frequency ν of the electromagnetic wave. With the current detector technologies it is only possible to measure the time average of the Poynting vector defined as:

$$< S_z >= \lim_{T\to\infty} \frac{1}{2T} c\epsilon_0 \int_{-T}^{T} E_{x0}^2 cos^2(\omega t - kz) dt = \frac{c\epsilon_0}{2} E_{x0}^2 \tag{2.12}$$

where $< . >$ denotes the time average as defined above.

The time average of the Poynting vector is called the *flux* (in astronomy) or the *irradiance* (in radiometry) of the electromagnetic wave in units of Wm^{-2}. The measurable quantity in an optical detector is the integral of the flux over the area of the detector, i.e., the power in units of Watt.

The *optical disturbance* $v(\mathbf{r}, t)$ is a dimensionless scalar defined to be proportional to one component, e.g., E_x of the electric field vector. For the mathematical treatment, it is very convenient to extend the optical disturbance by an imaginary part so that v becomes a complex quantity.

For a plane wave propagating along the z-axis, the extension of the optical disturbance by an imaginary part reads as

$$v(z,t) = v_0 e^{-i(\omega t - kz)} \tag{2.13}$$

The time average of the product vv^*,the superscript * denoting the complex conjugate, can be used to define the *intensity* as

$$I(z) = v_0^2. \tag{2.14}$$

The intensity is a dimensionless quantity that is proportional to the flux $< S_z >$ and is the quantity that we usually measure with optical detectors.

For the propagation of light in space it is convenient to introduce the time independent dimensionless *amplitude* $V(z)$ at frequency ν so that the monochromatic optical disturbance can be written as

$$v(z,t) = V(z)e^{-i2\pi\nu t} \tag{2.15}$$

With 2.14 the intensity $I(z) = |V(z)|^2$.

2.2.2. Huygens' Principle and Superposition principle

Huygens' principle states that all points on a wavefront can be treated as point sources of secondary spherical waves. Then at a later time the new position of the wavefront is the surface tangential to the forward going secondary waves. Huygens' construction is adequate away from any obstruction in the wave path. However at the edge of an aperture the construction predicts that the wave spills round this edge. Light of wavelength λ passing through an aperture of width a shows departures in angle of order λ/a from straight line propagation.

The superposition principle states that If the electromagnetic radiation from several sources is incident on any given point, the total electric field is simply the vector sum of the electric fields produced at that point by each source acting alone

$$E = E_1 + E_2 + ... \tag{2.16}$$

Equally, adding the individual magnetic fields vectorially gives the overall magnetic field.

2.2.3. Interference

The wave nature of light was experimentally demonstrated by Thomas Young in 1802. Young illuminated a screen with two pinholes with light from a single pinhole at a large distance. The light passing through the pinholes was projected on a second screen, where Young observed bright and dark fringes; he realized that the fringes were due to the *interference* of the light coming out from the two slits.

Figure 2.2a shows a simulation of Young's experiment. The red points indicates the position of the slits, it can be seen that in some directions the waves from the sources are in phase and give large amplitude waves which show up as the alternating white peaks and black troughs: the waves interfere *constructively*. In other directions the waves arrive out of phase and interfere *destructively* leaving the medium undisturbed, which appear in grey in the figure. The eye and light detectors respond to the time average of the intensity, as defined in 2.14. Figure 2.2b shows the detected intensity of light for Young's experiment. The regions of constructive interference would be brightly illuminated: and the destructive interference would be in darkness. A screen placed anywhere in front of the slits would show bright and dark interference fringes, so that these are called *non-localized* fringes. The average intensity over the fringe pattern is the same as the sum of the intensities for the two independents slits. No light is lost or gained, it is simply redistributed.

Fresnel, shortly after Young's observations, used the superposition principle to add secondary Huygens' spherical waves from apertures in an obstructed light beam. At any

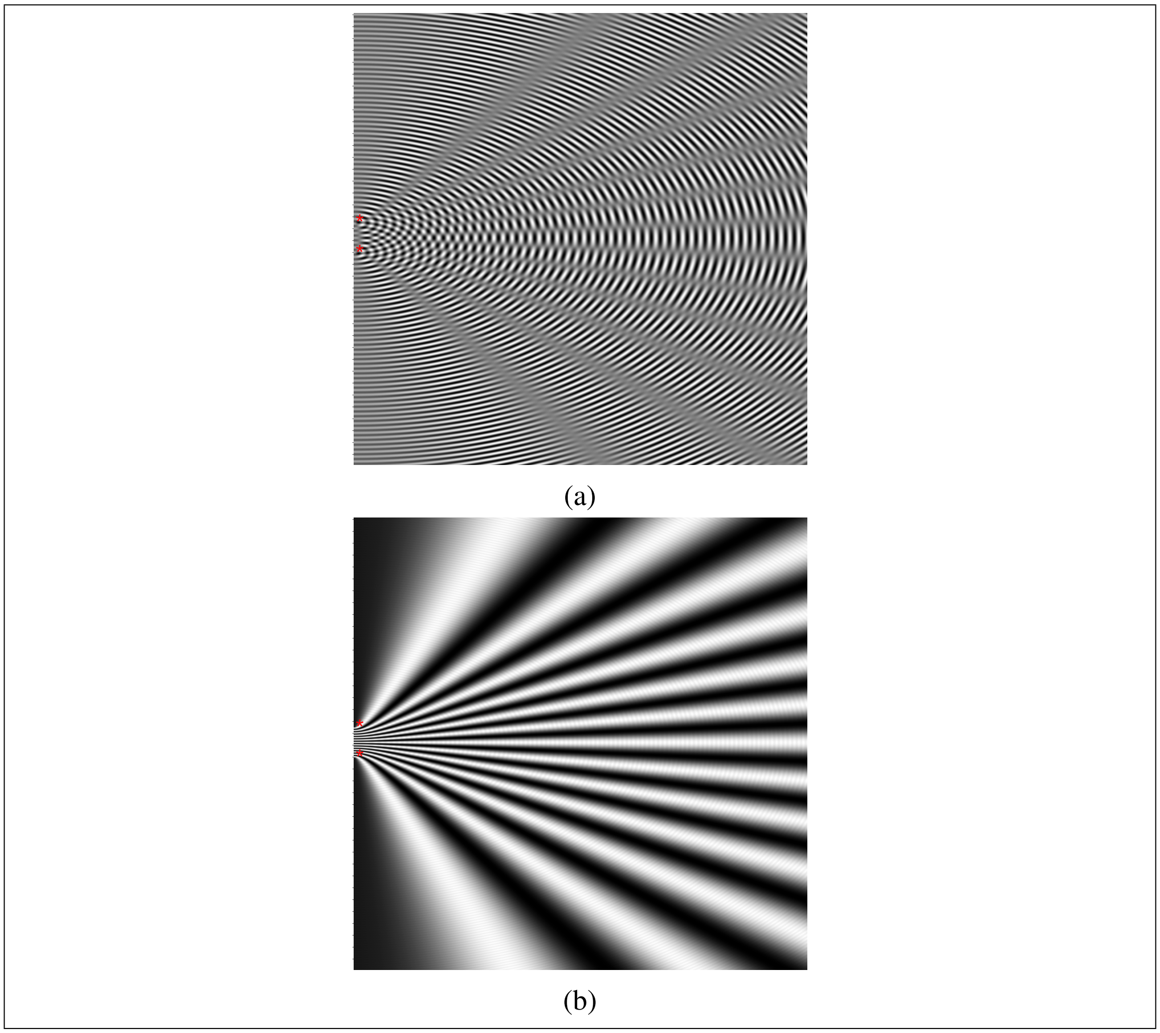

FIGURE 2.2. Young's experiment simulations. (a) Simulation showing constructive and destructive interference. (b) Time averaged intensity pattern.

point beyond the apertures the total electric field is the sum of secondary wave electric fields. When the path lengths of secondary waves to the point of observation are different there is a phase difference and this is the origin of interference effects such as that seen by Young.

Provided that the apertures are narrow, separated by a distance d, and the distance of the slits from source and screen are large, then the angle separation between adjacent bright fringes is:

$$\Delta\theta = \lambda/d \tag{2.17}$$

If the source slit is so wide that the path length from different points on the source to the slit varies by more than a fraction of a wavelength the interference pattern will be blurred. The Huygens-Fresnel principle of elementary waves, forms the basis of scalar diffraction theory.

2.2.4. Diffraction

Diffraction is interpreted as any interference effect due to the interruption of a wavefront by apertures or obstacles, often disposed in regular arrays. The pattern of illumination is very different when the plane of observation is near to the diffracting surface and when it is a large distance away. In the limit where the source and image plane can be considered to be infinitely far from the diffracting surface (see section 2.2.5.3 for criteria definition), the pattern is called *Fraunhoffer* diffraction and for finite distances is called *Fresnel* diffraction.

2.2.5. Scalar Diffraction Theory

When forming images in optical instruments, the propagation of light and the diffraction at physical boundaries needs to be dealt with. The fundamental equations treating the propagation of electromagnetic waves are Maxwells equations. They describe the propagation of both the electric and the magnetic field vectors E and H, respectively, through coupled partial differential equations.

In the scalar diffraction theory a number of assumptions and approximations are made for the imaging process. First, light is treated as a scalar quantity by using the optical disturbance $\upsilon(\mathbf{r}, t)$, as defined in section 3.2.1, that is proportional to one component of the electric field vector $\boldsymbol{E}$. Second, one assumes that the propagation of the two orthogonal vector components of $\boldsymbol{E}$ (E_x and E_y), which are perpendicular to the direction of propagation, can be treated independently.

These assumptions and approximations are valid if (1) diffracting apertures are large compared to the wavelength, and if (2) the diffracted fields are not observed too close to the diffracting apertures. Both conditions are easily fulfilled in optical systems in general, and in astronomical telescopes in particular.

2.2.5.1. The Helmholtz equation

The *Helmholtz equation*, is the time-independent form of the wave equation:

$$(\nabla^2 + k^2)V(\mathbf{r}) = 0 \tag{2.18}$$

with $V(r)$ the amplitude defined in 2.15, ∇^2 the Laplace operator $\frac{\delta^2}{\delta x^2} + \frac{\delta^2}{\delta y^2} + \frac{\delta^2}{\delta z^2}$, and $k = 2\pi/\lambda$. Solutions of this differential equation are a monochromatic plane wave, for example $V(r) = V_0 exp(ikz)$ for a wave propagating along the z-axis, or a monochromatic spherical wave $V(r) = \frac{V_0}{r} exp(ikr)$ with $r = |\mathbf{r}|$.

In optical systems, one is interested in the amplitude V in the plane of observation, the image plane, as a function of the amplitude in the aperture plane, or as a function of the amplitude of the object. Any solution for V needs to satisfy the Helmholtz equation at all points $\mathbf{r}$.

2.2.5.2. The Rayleigh-Sommerfeld Diffraction Formula

Figure 2.3 defines the variables involved in the calculation of the diffraction at an aperture **A**. The aperture plane has coordinates (ξ, ζ) and the coordinate vector $\boldsymbol{\xi}$, the plane of observation is denoted by (x, y) with the vector $\boldsymbol{x}$. The distance between the planes is z_1 and the vector between two points (ξ, ζ) and (x, y) is $\mathbf{r} = (x - \xi, y - \zeta, z_1)$, with the notation $r = |\mathbf{r}|$. The z-axis is the *optical axis*.

The *Rayleigh-Sommerfeld diffraction formula* makes use of the *Huygens-Fresnel principle* to compute the propagation of the amplitude from the aperture plane $\boldsymbol{\xi}$ into the plane of observation $\boldsymbol{x}$ by

$$V(x) = \frac{1}{i\lambda} \int \int_A V(\xi) \frac{e^{ikr}}{r} d\xi \tag{2.19}$$

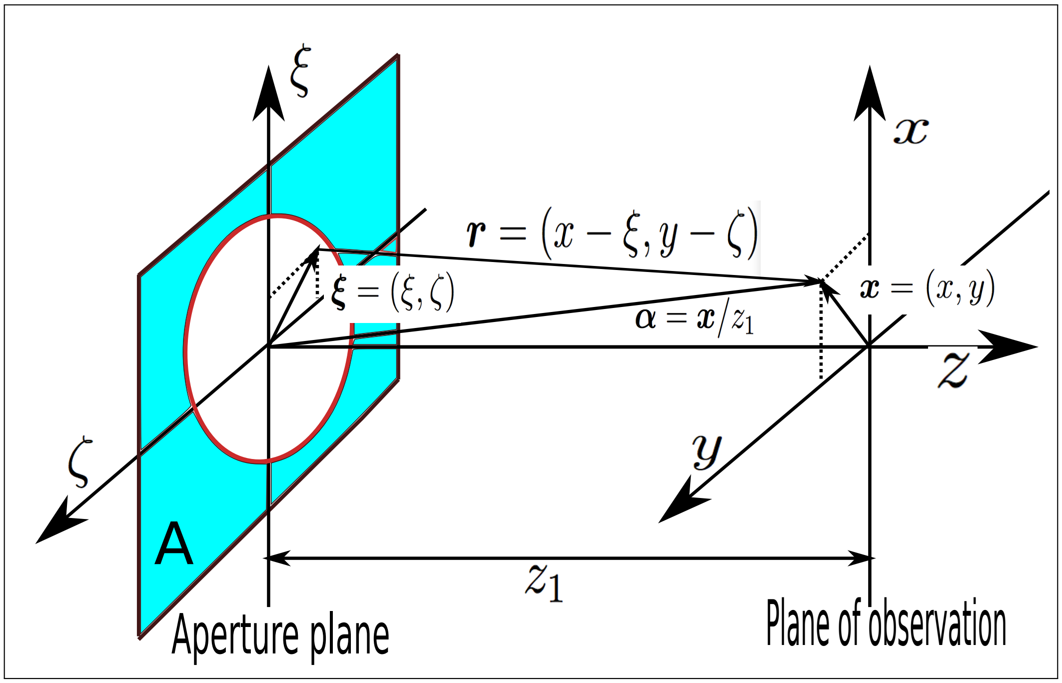

FIGURE 2.3. Geometry for the diffraction at an aperture **A**.

2.2.5.3. Fresnel and Fraunhoffer Approximations

For small angles formed by the distance vector $\boldsymbol{r}$ with respect to the z-axis, $|\boldsymbol{x} - \boldsymbol{\xi}|/z_1$, its length r can be approximated by the *quadratic Fresnel approximation*:

$$r = z_1 + \frac{|\boldsymbol{x} - \boldsymbol{\xi}|^2}{2z_1} - .... \tag{2.20}$$

The shape of the aperture **A** is called $A(\xi)$, and it is incorporated under the integral in 2.19 through $V_{ap}(\xi) = A(\xi)V(\xi)$. Later, replacing r with the quadratic Fresnel approximation, the amplitude for the *Fresnel diffraction* can be written as:

$$V(\boldsymbol{x}) = \frac{1}{i\lambda z_1} \int\int_{-\infty}^{\infty} V_{ap}(\boldsymbol{\xi}) e^{ik|\xi|^2/(2z_1)} e^{-ik\boldsymbol{x}\cdot\boldsymbol{\xi}/z_1} d\xi \tag{2.21}$$

At a very large distance from the aperture, i.e., for $|\xi|^2/2z_1 \ll \lambda$, the argument of the first exponential under the integral in 2.21 goes to zero. This approximation is called the

Fraunhofer approximation. Then the amplitude $V(\boldsymbol{x})$ in the plane of observation and the amplitude $V_{ap}(\boldsymbol{\xi})$ in the aperture are linked through a Fourier transform.

$$V(\boldsymbol{x}) = \frac{1}{i\lambda z_1} \int \int_{-\infty}^{\infty} V_{ap}(\boldsymbol{\xi}) e^{-ik\boldsymbol{x}\cdot\boldsymbol{\xi}/z_1} d\xi \tag{2.22}$$

the Fraunhofer approximation $|\xi|^2/(2z_1) \ll \lambda$ requires not only a large distance z_1 but also a very small angular size $|\xi|/z_1 \ll \sqrt{\lambda/z_1}$ of the aperture. If the aperture is of infinite extent the Fraunhofer approximation cannot be applied.

A lens (or a parabolic mirror), can be regarded as a simple focusing element that converts an incoming plane wave into a spherical wave converging in the focus. The distance between the lens and the focus is called the focal length.

In quadratic approximation, the lens can be described by:

$$L(\xi) = e^{-ik|\xi|^2/(2F)}, \tag{2.23}$$

with F the focal length. The ideal lens has no absorption, hence $|L(\xi)| = 1$ and it is infinitely thin. A lens in this definition is called a *thin lens*, and a mirror a *thin mirror*.

Replacing the spatial coordinate $\boldsymbol{x}$ in the focal plane by the angle coordinate $\boldsymbol{\alpha} = \boldsymbol{x}/F$ and regarding that in the focal plane $z_1 = F$, then the amplitude $V(\boldsymbol{\alpha})$ in the focal plane can be expressed as the Fourier transform of the amplitude $V_{ap}(\xi)$ in the aperture

$$V(\boldsymbol{\alpha}) = \frac{1}{i\lambda F} \int \int V_{ap}(\xi) e^{-ik\boldsymbol{\alpha}\cdot\boldsymbol{\xi}} d\boldsymbol{\xi} \tag{2.24}$$

With this formula we can describe the situation in a telescope. The incoming plane wave stems from a point-like star approximately at infinity, i.e., the phase $\varphi(\boldsymbol{\xi})$ of the complex amplitude is zero, and $V(\boldsymbol{\xi}) = V_0 =$ constant so that $V_{ap}(\boldsymbol{\xi}) = V_0 A(\boldsymbol{\xi})$. The light is diffracted at the aperture, and the telescope optics form the Fraunhofer diffraction pattern of the aperture in the telescope focal plane with the intensity distribution given by $I(\boldsymbol{\alpha}) = |V(\boldsymbol{\alpha})|^2$. Thus, this intensity distribution is the diffraction limited image of the point-like star, and the star is called *unresolved*. In the theory of linear systems, the diffraction pattern represents the response of the optical system to an impulse, in this case the approximately point-like intensity distribution of an unresolved star. This response is called the point-spread function (PSF) of the optical system. The PSF is dimensionless and describes the spread of the intensity in the focal plane.

Aberrations of the telescope optics are incorporated in the phase $\varphi(\boldsymbol{\xi})$ of the aperture function $A(\boldsymbol{\xi})$. Then, the subsequent PSF no longer describes the diffraction limited but the aberrated image of the point source.

2.2.6. PSF for circular apertures

The circular aperture is the most common case of a telescope aperture. The circular aperture is described by the circ-function that is defined as

$$circ(\frac{|\xi|}{R}) = \begin{cases} 1 & \text{if } |\xi| \leq R \\ 0 & \text{elsewhere} \end{cases} \tag{2.25}$$

A circular aperture with diameter D is then given by $circ(\frac{|\xi|}{D/2})$. $A(\xi)$ is illuminated by a point source at infinity with $V(\xi) = V_0$ =constant in the aperture plane. Using 2.24, and defining the dimesionless PSF as

$$PSF(\alpha) = \frac{I(\alpha)}{V_0^2}, \tag{2.26}$$

then the diffraction limited intensity distribution in the focal plane can be written as (see Goodman (2005) for mathematical derivation):

$$PSF(\alpha) = \frac{1}{(\lambda F)^2} A_0^2 \left(\frac{2J_1(k\alpha D/2)}{(k\alpha D/2)} \right)^2 \tag{2.27}$$

with $J_1(x)$ the first order Bessel function, A_0 the area of the circular aperture and k the wave number. The intensity distribution for uniformily-illuminated circular apertures has a

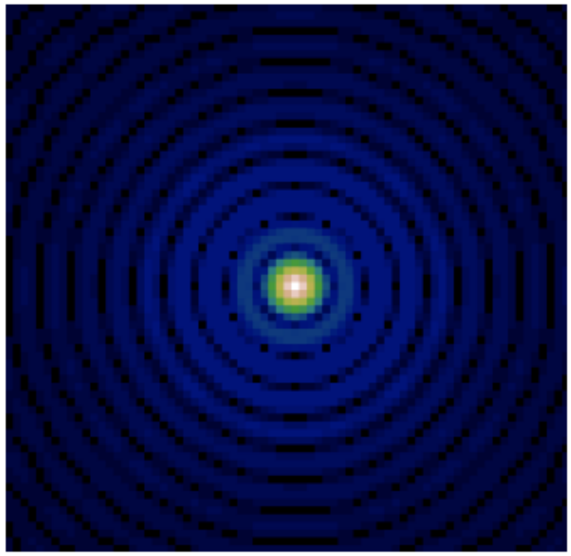

FIGURE 2.4. Circular aperture PSF.

series of concentric bright rings, called the *Airy pattern*, which is shown in figure 2.4. The bright region in the center of the diffraction pattern is called the Airy disk.

The first minimum of the PSF, the first dark ring is at $\alpha_{min} = 1.22\lambda/D$. For telescopes this criteria is called the *Rayleigh criterion* of resolution of a telescope. Another criterion that is often used is the *full width at half maximum (FWHM)*, i.e., the diameter of the Airy disk at half its maximum intensity, which is in good approximation $\alpha_{FWHM} = \lambda/D$. About 50% of the total intensity is within the FWHM of the Airy disk.

It should be noted that both quantities, α_{min} and α_{FWHM}, depend on the shape of the telescope aperture that usually has a central obscuration due to the telescope design with the secondary mirror centrally above the primary mirror. In general, any telescope element that is in the optical path, will affect the aperture and will bring additional diffraction to the optical system. Figure 2.5 shows the effects in the PSF for each of the elements of a reflecting telescope with a secondary mirror supported by a spider structure.

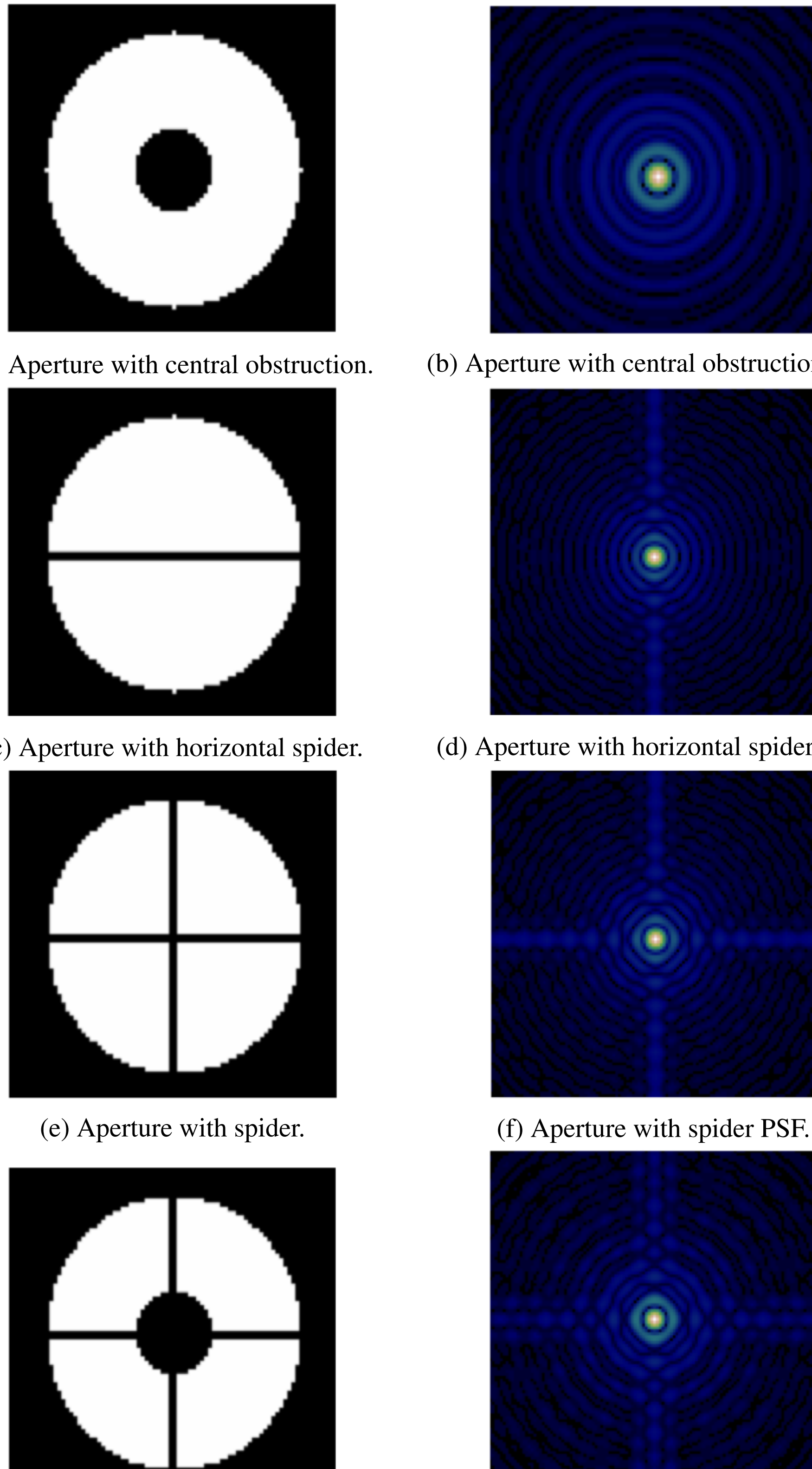

(a) Aperture with central obstruction.

(b) Aperture with central obstruction PSF.

(c) Aperture with horizontal spider.

(d) Aperture with horizontal spider PSF.

(e) Aperture with spider.

(f) Aperture with spider PSF.

(g) Aperture with obstruction and spider.

(h) Aperture with obstruction and spider PSF.

FIGURE 2.5. Reflecting telescope PSF.

2.2.7. Fourier Optics

Assuming monochromatic illumination, *Spatial frequencies* defined as f_ξ are introduced in the aperture plane. f_ξ can be regarded as a spatial coordinate calibrated by the wavelength, and we express the aperture function A as a function of f_ξ. It should be noted that the diameter of a circular aperture, as a function of f_ξ, is now wavelength dependent, $f_{\xi,D} = D/\lambda$. Assuming that the source is at a very large distance z_0, an approximately plane wave arrives in the aperture plane. Introducing the thin lens, $L(f_\xi) = exp(-i2\pi|f_\xi|^2\lambda/(2F)$, in the aperture plane, we write the intensity distribution $I(\alpha)$ in the image plane as

$$I(\boldsymbol{\alpha}) = V_0^2 \frac{\lambda^2}{F^2} \left| \int A(\boldsymbol{f_\xi}) e^{-i2\pi \boldsymbol{f_\xi} \cdot \boldsymbol{\alpha}} d\boldsymbol{f_\xi} \right|^2 = V_0^2 \frac{\lambda^2}{F^2} \left| \mathcal{F}(A) \right|^2 \tag{2.28}$$

with $\mathcal{F}(\mathcal{A})$ the Fourier transform of the aperture function A. This is the diffraction limited image of a point source at infinity. The shape of the amplitude is given by the Fraunhofer diffraction pattern of the aperture in the image plane

The shape of the image intensity distribution is described by the dimensionless point-spread function (PSF) of the optical system defined by 2.26.

To find the intensity distribution in the image plane one has to sum up individual PSFs, each weighted according to the object intensity. This assumes that the PSF is shift-invariant over the field of view, i.e. that the so-called isoplanatic angle is larger than the size of the source.

2.3. The Optical Transfer function

The contents of this section are taken from Schmidt (2010) , for a complete theoretical development on the Optical Transfer Function please refer to Williams and Becklund (1989)

The linear superposition of shift-invariant PSFs is replaced by the integral over the source yielding the convolution of the object intensity distribution that, from now on, we will denote by $O(\alpha')$, with the PSF:

$$\begin{aligned} I(\alpha) &= \int O(\alpha')PSF(\alpha - \alpha')d\alpha' \\ &= O(\alpha) * PSF(\alpha) \end{aligned} \tag{2.29}$$

The convolution of the object intensity with the PSF in image space can be replaced by a multiplication in Fourier space. This very general property, called the *convolution theorem*, can be used when Fourier transforming both sides of 2.29 turning the Fourier transform of the convolution into the product of the individual Fourier transforms of the object intensity $O(\alpha)$ and of $PSF(\alpha)$:

$$\mathcal{F}\{I(\alpha)\} = \mathcal{F}\{O(\alpha)\}\mathcal{F}\{PSF(\alpha)\} \tag{2.30}$$

We can see that the PSF's Fourier spectrum modulates the object irradiance's spectrum to yield the diffraction image.

The Optical Transfer Function (OTF) describes the frequency response of an optical system and is defined as:

$$OTF(\boldsymbol{f_\xi}) = \frac{\mathcal{F}\{PSF(\boldsymbol{x})\}}{\int_{-\infty}^{\infty}\int_{-\infty}^{\infty} PSF(\boldsymbol{x})d\boldsymbol{x}}, \tag{2.31}$$

The OTF is also the autocorrelation of the aperture function:

$$OTF(\boldsymbol{f_\xi}) = \frac{A(\boldsymbol{\xi})A^*(\boldsymbol{\xi})}{\int_{-\infty}^{\infty}\int_{-\infty}^{\infty} |A(\boldsymbol{\xi})|^2 d\boldsymbol{\xi}}\Big|_{\boldsymbol{\xi}=\lambda z_i \boldsymbol{f_\xi}} \tag{2.32}$$

For the case of a circular aperture with diameter D, the OTF is an azimuthally symmetric function of $|\boldsymbol{f_\xi}|$ given by

$$OTF(|\boldsymbol{f_\xi}|) = \begin{cases} \frac{2}{\pi}[cos^{-1}(\frac{|\boldsymbol{f_\xi}|}{f_0}) - \frac{|\boldsymbol{f_\xi}|}{f_0}\sqrt{1-(\frac{|\boldsymbol{f_\xi}|}{f_0})^2}] & \text{for } |\boldsymbol{f_\xi}| \leq f_0 \\ 0 & \text{otherwise,} \end{cases} \tag{2.33}$$

where $f_0 = D/(\lambda z_i)$. This quantity f_0 is the cutoff frequency. Figure 2.6 shows the OTF for the diffraction limited system with a circular aperture. It can be appreciated that the OTF is a low pass filter; this property is common to all optical systems.

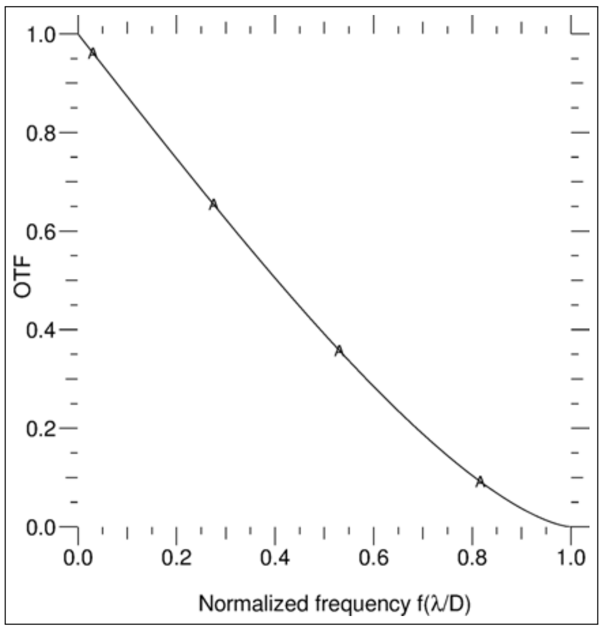

FIGURE 2.6. OTF for circular aperture.

The magnitude of the OTF is called the *Modulation Transfer function*(MTF).

For real optical systems, aberrations must be considered. The aperture function can be redefined in complex notation as a generalized aperture function:

$$\mathcal{A} = A(\boldsymbol{\xi})exp(i(2\pi/\lambda)W(\boldsymbol{\xi})) \tag{2.34}$$

where $W(\boldsymbol{\xi})$ describes the phase effects due to aberrations in the aperture as defocus, astigmatism, etc.

2.3.1. Strehl ratio

The performance of an imaging system is determined by its PSF. It is handy to have a single-number metric to describe performance. The most common metric is the Strehl ratio $\mathcal{S}$, which is defined in Andersen and Enmark (2011) as the ratio between the peak intensity, I_{max}, of the real PSF and the peak intensity, $I_{dl_{max}}$, of the corresponding diffraction limited point spread function with no error sources:

$$\mathcal{S} = \frac{I_{max}}{I_{dl_{max}}} \tag{2.35}$$

Alternatively, the Strehl ratio $\mathcal{S}$ can be computed as

$$\mathcal{S} = \frac{\int_{-\infty}^{\infty} \mathcal{A}(\boldsymbol{\xi}) d\boldsymbol{\xi}}{\int_{-\infty}^{\infty} A(\boldsymbol{\xi}) d\boldsymbol{\xi}} \tag{2.36}$$

where $\mathcal{A}(\boldsymbol{\xi})$ is the generalized aberrated aperture defined by 2.34 and $A(\boldsymbol{\xi})$ is the unaberrated aperture function.

Or equivalently:

$$\mathcal{S} = \frac{\int_{-\infty}^{\infty} OTF(\boldsymbol{f_\xi}) d\boldsymbol{f_\xi}}{\int_{-\infty}^{\infty} OTF_{dl}(\boldsymbol{f_\xi}) d\boldsymbol{f_\xi}} \tag{2.37}$$

where $OTF_{dl}(\boldsymbol{f_\xi})$ is the OTF of an unaberrated (or diffraction-limited) system. For a perfectly unaberrated system, $\mathcal{S} = 1$, and this is the maximum possible value of the Strehl ratio. Low Strehl ratio indicates poor image quality

2.4. Astronomical imaging through the atmosphere

The atmosphere is a gaseous envelope that surrounds the earth and extends to six hundred kilometers above the surface. Astronomers have observed for centuries that atmospheric turbulence limits the resolution of their telescopes. This is why observatories are built on mountain tops; the location minimizes the turbulent path distance through which the light must propagate. Turbulence in Earth's atmosphere is caused by random variations in temperature and convective air motion, which alter the air's refractive index, both spatially and temporally [Schmidt (2010)].

As stated in Roddier (1981), the atmospheric turbulence is a major problem in optical astronomy as it drastically reduces the angular resolution of telescopes. When a stellar image is observed through a telescope, the observed image structure is usually far from the theoretical diffraction pattern and changes rapidly with time. With small apertures a random motion of the image is often the main effect. With large apertures spreading and blurring of the image occur; at short exposure time a speckle structure is often observed.

This section is a brief summary of the results on optical propagation as reviewed by Tatarskii (1968) and presented in Schmidt (2010), Glindeman (2011) and Roddier (1981). Please refer to this last source for the complete detailed development on the propagation of light through atmospheric turbulence.

2.4.1. Common atmospheric effects on optical waves

As explained in Andrews (2004),

> The three primary atmospheric processes that affect optical wave propagation are *absorption*, *scattering*, and *refractive-index fluctuations* (i.e., optical turbulence). Absorption and scattering by the constituent gases and particulates of the atmosphere give rise primarily to attenuation of an optical wave. Index of refraction fluctuations lead to *irradiance fluctuations*, *beam broadening*, and *loss of spatial coherence* of the optical wave, among other effects. Clearly, these deleterious effects have far-reaching consequences on astronomical imaging, optical communications, remote sensing, laser radar, and other applications that require the transmission of optical waves through the atmosphere.

2.4.2. Statistical properties of Atmospheric Turbulence

A flow becomes turbulent, i.e. unstable and random, when the Reynolds number $R_e = v_0 L_0 / k_v$, exceeds a critical value. Here v_0 is a characteristic velocity and L_0 a characteristic size of the flow; k_v is the kinematic viscosity of the fluid. Atmospheric air flow is nearly always turbulent and $R_e \approx 10^7$ in general corresponds to fully developed turbulence.

The most widely accepted theory of turbulent flow, due to its consistent agreement with observation, was first put forward byA. N. Kolmogorov. For the formal development please refer to Kolmogorov (1941).

Differential heating and cooling of Earth by sunlight and the diurnal cycle cause large-scale variations in the temperature of air. This process consequently creates wind. As air moves, it transitions from laminar flow to turbulent flow. In turbulent flow the velocity field is not uniform and it acquires randomly distributed pockets of air, called turbulent eddies. These eddies have varying characteristic sizes and temperatures. Since the density of air, and thus its refractive index, depends on temperature, the atmosphere has a random refractive-index profile.

Kolmogorov suggested that in fully developed turbulence, the kinetic energy of large eddies is transferred to smaller and smaller eddies, see figure 2.7. The average size of the largest eddies, L_0, is called the outer scale. Near the ground, L_0 is on the order of the height above ground, while high above the ground, it can be just tens to hundreds of meters. The average size of the smallest turbulent eddies, l_0, is called the inner scale. At very small scales, smaller than the inner scale, the energy dissipation caused by friction prevents the turbulence from sustaining itself. The inner scale l_0 can be a few millimeters near the ground to a few centimeters high above the ground. The range of eddy sizes between the inner and outer scales is called the inertial subrange.

Kolmogorov assumed that the motion of the turbulent structure is both statistically stationary and isotropic, implying that the second and higher order statistical moments of the turbulence depend only on the distance between any two points in the structure.

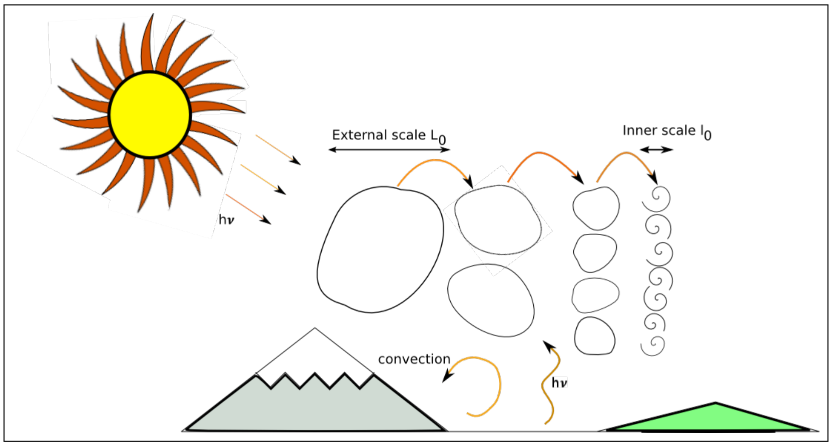

FIGURE 2.7. Atmospheric turbulence as described by Kolmogorov.

Because the amount of energy that is being injected into the largest turbulence structure must be equal to the energy that is dissipated as heat, it can be derived that

$$v_0 \propto \epsilon_0^{1/3} l^{1/3} \tag{2.38}$$

with l the characteristic size of the smaller eddies and ϵ_0 is the rate of viscous dissipation. For the kinetic energy $\hat{E}(k)$ it is obtained that

$$\hat{E} \propto k^{-5/3} \tag{2.39}$$

For isotropic turbulence, the kinetic energy spectrum $\hat{E}_p(\boldsymbol{k})$ can be computed by integrating over the unit sphere:

$$\hat{E}_p(\boldsymbol{k}) \propto k^{-11/3} \tag{2.40}$$

with $\boldsymbol{k}$ the three-dimensional spatial wave vector, $k = |\boldsymbol{k}|$ and $k \propto 2\pi/l$

This relationship expresses the *Kolmogorov spectrum*. It holds in the *inertial range* of turbulence for $l_0 \ll 2\pi/k \ll L_0$.

2.4.2.1. Index of refraction fluctuations

Light travelling through the atmosphere is affected by fluctuations of the index of refraction (or refractive index). The physical source of these fluctuations are temperature inhomogeneities produced by turbulent mixing of air. The refractive index at a point in space r can be written as

$$n(\boldsymbol{r}) = \mu_n(\boldsymbol{r}) + n_1(\boldsymbol{r}) \tag{2.41}$$

where $\mu_n(\boldsymbol{r}) \approx 1$ is the slowly varying mean value of the refractive index, and $n_1(\boldsymbol{r})$ is the deviation of the index from its mean value. At optical wavelengths, the refractive index of air is given approximately by

$$n(\boldsymbol{r}) = 1 + 77.6 \times 10^{-6}(1 + 7.52 \times 10^{-3}\lambda^{-2})\frac{P(\boldsymbol{r})}{T(\boldsymbol{r})} \tag{2.42}$$

where λ is the optical wavelength in micrometers, P is the pressure in millibars, and T is the ordinary temperature in Kelvin. For $\lambda = 0.5um$ the refractive index variation is given by:

$$n1 = 7.99 \times 10^{-5}\frac{d\theta}{T^2} \tag{2.43}$$

where θ is the potential temperature which is linearly related to the ordinary temperature T.

2.4.2.2. Kolmogorov and Von Kármán Spectrum

The refractive index also follows Kolmogorov statistics, then the power spectrum $\Phi_n(\boldsymbol{k})$ of $n(\boldsymbol{r})$ that is called the Kolmogorov spectrum has the same spatial frequency dependency as the kinetic energy and can be expressed as

The Kolmogorov refractive-index power spectral density Φ_n^K is

$$\Phi_n^K(\boldsymbol{k}) = 0.033C_n^2 k^{-11/3} \text{ for } \tfrac{1}{L_0} \ll \tfrac{k}{2\pi} \ll \tfrac{1}{l_0} \tag{2.44}$$

with $\boldsymbol{k}$ the three-dimensional spatial wave vector, $k = |\boldsymbol{k}|$ in rad/m and $k \propto 2\pi/l$. The power spectral density, is power per volume element $d\boldsymbol{k}$, i.e. per m^{-3}. C_n^2 is the *structure* *constant* of the refractive index fluctuations and has units of $m^{-2/3}$ so that $\Phi_n(\boldsymbol{k})$ has units of $1/m^{-3}$. C_n^2 characterises the strength of the fluctuations of n. The Kolmogorov theory predicts a mathematical form for $\Phi_n^K(\boldsymbol{k})$ only inside the inertial range.

An extension beyond this regime is given by the *von Kármán spectrum*, reading as

$$\Phi_n^{vK}(\kappa) = \frac{0.033C_n^2}{(\kappa^2 + \kappa_0^2)^{11/6}} \text{ for } 0 \leq \kappa \ll 1/l_0, \tag{2.45}$$

and the modified von Kármán power spectral density:

$$\Phi_n^{mvK}(\kappa) = 0.033C_n^2 \frac{exp(-\kappa^2/\kappa_m^2)}{(\kappa^2 + \kappa_0^2)^{11/6}} \text{ for } 0 \leq \kappa \ll \infty, \tag{2.46}$$

where $\kappa_m = 5.92/l_0$ and $\kappa_0 = 2\pi/L_0$. Compared to the Kolmogorov spectrum, the power is reduced outside the inertial range, see figure 2.8 .

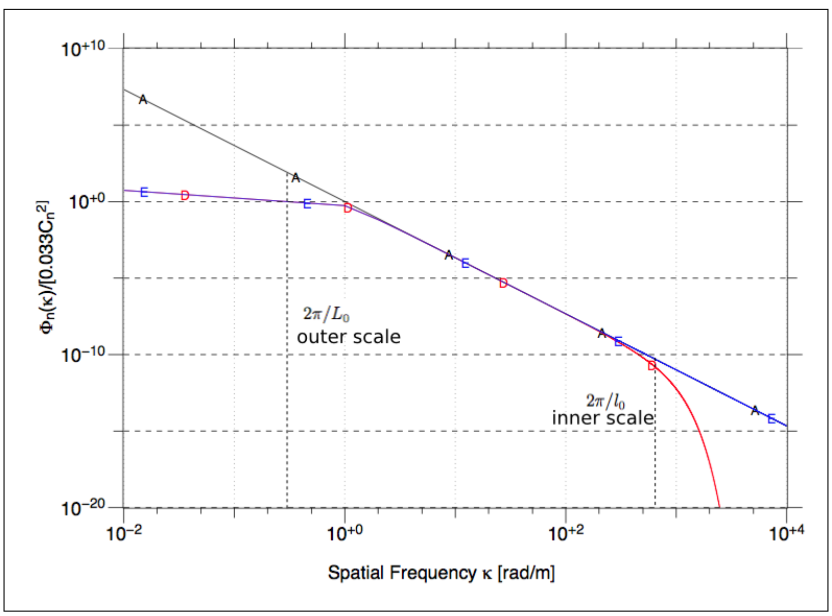

FIGURE 2.8. Normalized Kolmogorov turbulence spectrum (black), Von Karman turbulence spectrum (blue) and modified von Karman spectrum, l_0 = 1cm and L_0 = 10m.

The power spectrum of $n(\boldsymbol{r})$ is related to its autocorrelation $\Gamma_n(\boldsymbol{r}) = \langle n(\boldsymbol{r}')n(\boldsymbol{r}'+\boldsymbol{r})\rangle$ by the Wiener-Khinchine theorem (See Glindeman (2011)):

$$\Gamma_n(\boldsymbol{r}) = \int \Phi_n(\boldsymbol{k}) e^{-i\boldsymbol{k}\cdot\boldsymbol{r}} d\boldsymbol{k} \tag{2.47}$$

2.4.2.3. Structure Function

The structure function of the refractive index, in the mean-square difference of the refractive index at two points separeted by $\boldsymbol{r}$, yielding

$$\begin{aligned} D_n(\boldsymbol{r}) &= \left\langle |n(\boldsymbol{r}') - n(\boldsymbol{r}' - \boldsymbol{r})|^2 \right\rangle \\ &= 2(\Gamma_n(0) - \Gamma_n(\boldsymbol{r})) \end{aligned} \tag{2.48}$$

For Kolmogorov turbulence its functional form was derived in Obukhov (1949), yielding

$$D_n(\boldsymbol{r}) = C_n^2 r^{2/3} \tag{2.49}$$

with $r = |\boldsymbol{r}|$. Temperature and velocity also follow Kolmogorov's law, therefore structure functions for temperature and velocity are also given by

$$D_T(\boldsymbol{r}) = C_T^2 r^{2/3} \quad D_v(\boldsymbol{r}) = C_v^2 r^{2/3} \tag{2.50}$$

The Kolmogorov spectrum and its structure function form the basis for the description of wave propagation through turbulence.

2.4.3. Statistical Properties of the Perturbed Complex Wave

For complete detail see Roddier (1981) and Glindeman (2011). For the sake of simplicity, only horizontal monochromatic plane waves are considered, propagating downwards from a star at zenith, towards a ground-based observer. Each point in the atmosphere will be designated by a horizontal coordinate vector $\boldsymbol{\xi}$ and an altitude h above the ground. The amplitude of the incoming plane wave is defined as $V(\boldsymbol{\xi}) = V_0 exp(ikz) = 1$.

2.4.3.1. Output of a thin turbulence layer

After propagation through a thin turbulent layer at altitude h, the phase is related to the distribution of the refractive index through

$$\varphi_h(\boldsymbol{\xi}) = \frac{2\pi}{\lambda} \int_h^{h+\delta h} n(\boldsymbol{\xi}, z) dz \tag{2.51}$$

where δh is the thickness of the layer and $\boldsymbol{\xi} = (\xi, \zeta)$ denotes the horizontal coordinate vector. The amplitude of a plane wave immediately after propagation through a layer at altitude h can be written as

$$V_{\varphi,h}(\boldsymbol{\xi}) = e^{i\varphi h(\boldsymbol{\xi})} \tag{2.52}$$

To describe the statistical properties of the complex wave we need the correlation function of the amplitude $V_{\varphi,h}(\boldsymbol{\xi})$.

The correlation function, also called the *second order moment*, of the optical disturbances υ at positions $\boldsymbol{x_1}$ and $\boldsymbol{x_2}$ in aplane at times $t+\tau$ and t is called the *mutual coherence function* (MCF), defined as:

$$\Gamma(\boldsymbol{x_1}, \boldsymbol{x_2}, \tau) = \left\langle \upsilon(\boldsymbol{x_1}, t+\tau)\upsilon^*(\boldsymbol{x_2}, t)\right\rangle \tag{2.53}$$

The correlation function $\Gamma_{\varphi,h}(\boldsymbol{\xi})$ for atmospheric turbulence is equivalent to

$$\Gamma_{\varphi,h}(\boldsymbol{\xi}) = \left\langle e^{i[\varphi h(\boldsymbol{\xi}') - \varphi h(\boldsymbol{\xi}' - \boldsymbol{\xi})]}\right\rangle = e^{-\frac{1}{2} < [\varphi h(\boldsymbol{\xi}') - \varphi h(\boldsymbol{\xi}' - \boldsymbol{\xi})]^2 >} \tag{2.54}$$

Taking the phase structure function $D_{\varphi,h}(\boldsymbol{\xi}) =< [\varphi h(\boldsymbol{\xi}') - \varphi h(\boldsymbol{\xi}' - \boldsymbol{\xi})]^2 >$,

$$\Gamma_{\varphi,h}(\boldsymbol{\xi}) = e^{-\frac{1}{2} D_{\varphi,h}(\boldsymbol{\xi})} \tag{2.55}$$

and inversily,

$$D_{\varphi,h}(\boldsymbol{\xi}) = 2[\Gamma_{\varphi,h}(\boldsymbol{0}) - \Gamma_{\varphi,h}(\boldsymbol{\xi})] \tag{2.56}$$

The phase structure function is calculated as

$$D_{\varphi,h}(\boldsymbol{\xi}) = 2.91 \left(\frac{2\pi}{\lambda}\right)^2 \delta h C_n^2 \xi^{5/3} [rad^2] \tag{2.57}$$

with $\xi = |\boldsymbol{\xi}|$.

2.4.3.2. Propagation through multiple layers

The real atmosphere can be regarded as a composition of many turbulent layers, each of them fulfilling the thin screen approximation. The propagation of the correlation function through the atmosphere can be reduced to the product of the correlation functions of the single layers, because they are statistically independent. The correlation function on the ground after propagation through a continuous distribution of turbulent layers is calculated as

$$\left\langle V_\varphi(\boldsymbol{\xi}') V_\varphi^*(\boldsymbol{\xi}' - \boldsymbol{\xi}) \right\rangle = e^{-\frac{1}{2} D_\varphi(\boldsymbol{\xi})} \tag{2.58}$$

When observing at angular distance $\zeta = |\zeta|$ from the zenith one obtains

$$D_\varphi(\boldsymbol{\xi}) = 2.91 \left(\frac{2\pi}{\lambda}\right)^2 (cos\zeta)^{-1} \int C_n^2(h) dh \, \xi^{5/3} \;\; [\text{rad}^2] \tag{2.59}$$

2.4.4. The Fried Parameter r_0

The atmospheric coherence diameter or correlation length r_0 , also known as the Fried parameter, was introduced by D.L. Fried during the 1960's. Fried analyzed the resolution of an imaging telescope as the volume underneath the atmospheric MTF. The expression in 2.59 was simplified by Fried, introducing the correlation length r_0 defined by

$$r_0 = \left(0.423 \left(\frac{2\pi}{\lambda}\right)^2 (cos\zeta)^{-1} \int C_n^2(h) dh \right)^{-3/5} \tag{2.60}$$

The numerical parameter, 0.423, defines r_0 such that the variance of the phase over a circle with a diameter of r_0 is about 1 rad^2. In this sense, the Fried parameter defines the size of a turbulence cell. Typical values of r_0 are 0.6m in the K-band and, correspondingly, 0.11m in the visible.

The phase structure function $D_\varphi(\boldsymbol{\xi})$ in 2.59 can now be expressed by

$$D_\varphi(\boldsymbol{\xi}) = 6.88 \left(\frac{\xi}{r_0}\right)^{5/3} \quad [\mathrm{rad}^2] \tag{2.61}$$

and the Kolmogorov power spectrum is

$$\Phi(\boldsymbol{k}) = 0.0229 r_0^{-5/3} k^{-11/3} \quad [\mathrm{rad}^2/\mathrm{m}^{-2}] \tag{2.62}$$

with $k = |\boldsymbol{k}|$ and $\boldsymbol{k}$ the two-dimensional spatial frequency vector.

2.4.5. The Seeing

The seeing, denoted s, is another parameter that is frequently used to characterize the overall strenght of the turbulence. The seeing connects to the value of r_0 by the relation

$$s = 0.98 \frac{\lambda}{r_0} \tag{2.63}$$

When the diameter of the pupil of the telescope is large compared to the value of r_0, the seeing gives the theoretical angular resolution that can be obtained when observed through turbulence. This condition is called *seeing-limited* observation.

2.4.6. Taylor frozen-turbulence hypothesis

The Taylor frozen-turbulence hypothesis addresses the question regarding the temporal changes of the turbulence pattern. In Lawson (2000) is explained that the time scale for these changes is usually much longer than the time it takes the wind to blow the turbulence past the telescope aperture. According to the Taylor hypothesis of frozen turbulence, the variations of the turbulence can be modeled as a ”frozen” pattern that is transported across the aperture by the wind. The temporal behavior of the turbulence is characterized by the time constant

$$\tau_0 = r_0/v \tag{2.64}$$

where v is the wind speed. The phase at point $\boldsymbol{\xi}$ at time $t + \tau$ can be written as

$$\varphi_{t+\tau}\boldsymbol{\xi} = \varphi_t(\boldsymbol{\xi} - \boldsymbol{v}\tau) \tag{2.65}$$

The temporal phase structure function is

$$D_\varphi(\boldsymbol{v}\tau) = 6.88\left(\frac{v\tau}{r_0}\right)^{5/3} \tag{2.66}$$

2.4.7. Atmosphere MTF

When Fried introduced r_0, he did it as a part of calculating the average MTF of images taken through the atmosphere.

$$\mathcal{H}(f_\xi) = exp\left\{-3.44\left(\frac{f_\xi}{2f_0}\frac{D}{r_0}\right)^{5/3}\left[1 - \alpha\left(\frac{f_\xi}{2f_0}\right)^{1/3}\right]\right\} \tag{2.67}$$

with f_0 the cutoff frequency.

$$\alpha = \begin{cases} 0 & \text{for long-exposure imagery,} \\ 1 & \text{for short-exposure imagery without scintillation,} \\ \frac{1}{2} & \text{for short-exposure imagery with scintillation} \end{cases} \tag{2.68}$$

Long-exposure observations are assumed to be long enough that the image center wanders randomly many times in the image plane, this is achieved with exposure time $t \gg \tau_0$. Conversely, short-exposure observations are assumed to be short enough that only one realization of tilt affects the image ($t \ll \tau_0$).

In Andrews and Phillips (2005) an analytic approximation of the Strehl Ratio S for the long-exposure case without scintillation, $\alpha = 0$, is given by

$$S \approx \frac{1}{\left[1 + (D/r_0)^{5/3}\right]^{6/5}} \tag{2.69}$$

2.4.8. Anisoplanatism

If an optical system's characteristics are not shift-invariant, the system has a property called anisoplanatism. Taking the angular structure function of the phase $D_\phi(\theta)$ defined by

$$D_\phi(\Delta\theta) = \left\langle |\phi(\theta) - \phi(\theta + \Delta\theta|^2 \right\rangle \tag{2.70}$$

where θ is the angular coordinate in the object field and $\Delta\theta$ is an angular separation between two points in the object field. The isoplanatic angle θ_0 is defined by the angle for which

$$D_\phi(\theta_0) = 1 \text{ rad}^2 \tag{2.71}$$

θ_0 is given by

$$\theta_0 = \left[2.91 k^2 (\Delta h)^{5/3} \int_0^{\Delta h} C_n^2(h) \left(1 - \frac{h}{\Delta h}\right)^{5/3} dh\right]^{-3/5} \tag{2.72}$$

This may be considered the largest field angle over which the optical path length through the turbulence does not differ significantly from the on-axis optical path length through the turbulence.

2.4.9. Long exposure OTF for a telescope under the atmosphere

The structure of the image undergoes random related changes related to the motion of atmospheric inhomogenities in front of the telescope. Exposure times as short as a few milliseconds are necessary in order to freeze the image. In conventional astronomy, the exposure time easily exceeds a few seconds, in which case the recorded image is no longer random. It is an average and we shall refer to it as a *long-exposure image*.

Recalling $O(\alpha)$ as the irradiance distribution from the object as a function of the direction α in the sky and $I(\alpha)$ the observed irradiance distribution, in the instantaneous image, as a function of the same variable α. A long-exposure image will be considered as the ensemble average $\langle I(\alpha) \rangle$. Since astronomical objects are entirely incoherent, the relation between $\langle I(\alpha) \rangle$ and $O(\alpha)$ is linear and is given by

$$\langle I(\alpha) \rangle = O(\alpha) * \langle PSF(\alpha) \rangle \tag{2.73}$$

with $\langle PSF(\alpha) \rangle$ being the average image of a point source. In the Fourier space the relationship is given by

$$\langle \mathcal{F}\{I\}(f_\xi) \rangle = \mathcal{F}\{O\}(f_\xi) \, \langle OTF(f_\xi) \rangle \tag{2.74}$$

where $\langle OTF(f_\xi) \rangle$ is the optical transfer function of the whole system, telescope and atmosphere.

Assuming that we are observing, through the atmosphere, a monochromatic point source of wavelength λ, and denoting $V_\varphi(\boldsymbol{\xi})$ as the complex amplitude at the telescope aperture $A(\boldsymbol{\xi}) = circ(\frac{|\xi|}{R})$ and the spatial frequency $f_\xi = |\boldsymbol{\xi}|/\lambda$, the optical transfer function for long exposures is

$$\langle OTF(f_\xi) \rangle = \frac{1}{S} \int \langle V_\varphi(f_\xi) V_\varphi^*(f_\xi + f) \rangle A(f_\xi) A^*(f_\xi + f) df_\xi \tag{2.75}$$

where S the aperture area (in wavelength squared units). Equation 2.75 contains the coherence function of the amplitude, $\Gamma_\varphi(f) = \langle V_\varphi(f_\xi) V_\varphi^*(f_\xi + f) \rangle$. As $\Gamma_\varphi(f)$ depends only upon f, then 2.75 can be written as

$$\langle OTF(f_\xi) \rangle = \Gamma_\varphi(f_\xi \lambda) \frac{1}{S} \int A(f_\xi) A^*(f_\xi + f) df_\xi \tag{2.76}$$

where the integral term corresponds to $OTF_{tel}(f_\xi)$, the telescope diffraction limited OTF. Finally the expression for the long exposure OTF is

$$\langle OTF(f_\xi) \rangle = \Gamma_\varphi(f_\xi \lambda) \, OTF_{tel}(f_\xi) \tag{2.77}$$

Recalling the OTF definition in section 2.3, the autocorrelation function $\Gamma_\varphi(f_\xi\lambda)$ can be interpreted as the OTF of the aperture made by the atmosphere on top of the telescope aperture. Defining $OTF_\varphi(f_\xi)$ as the atmosphere OTF, with

$$OTF_\varphi(f_\xi) = \Gamma_\varphi(f_\xi\lambda) \tag{2.78}$$

Showing the fundamental result that the long exposure OTF of the whole system, telescope and atmosphere, is the product of the telescope OTF with the atmosphere OTF.

$$OTF_{long\ exposure} = OTF_{tel}(f_\xi)OTF_\varphi(f_\xi) \tag{2.79}$$

The long exposure PSF is easily found as the inverse Fourier Transform of the long exposure OTF.

Figure 2.9 plots the OTF for the different exposure time value as described by 2.67. On figure 2.10 short exposure and long exposure images with their OTF are shown.

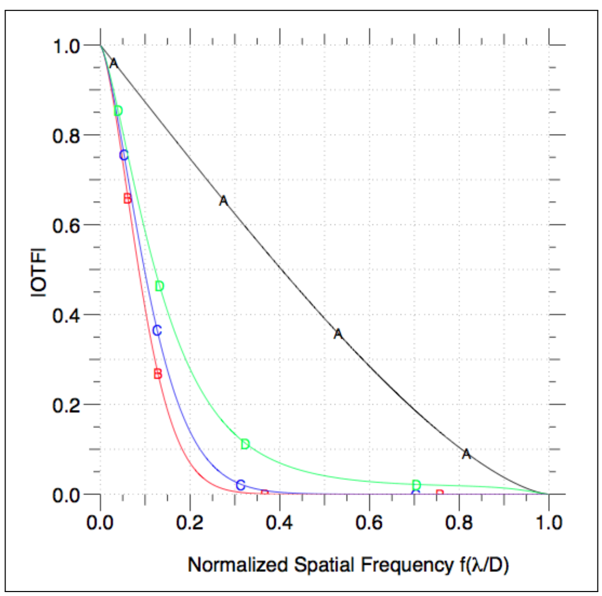

FIGURE 2.9. Diffraction limited OTF (black), atmosphere and telescope composite OTF, for $D/r_0 = 4$, short exposure without scintillation (green), short exposure with scintillation (blue), long exposure (red).

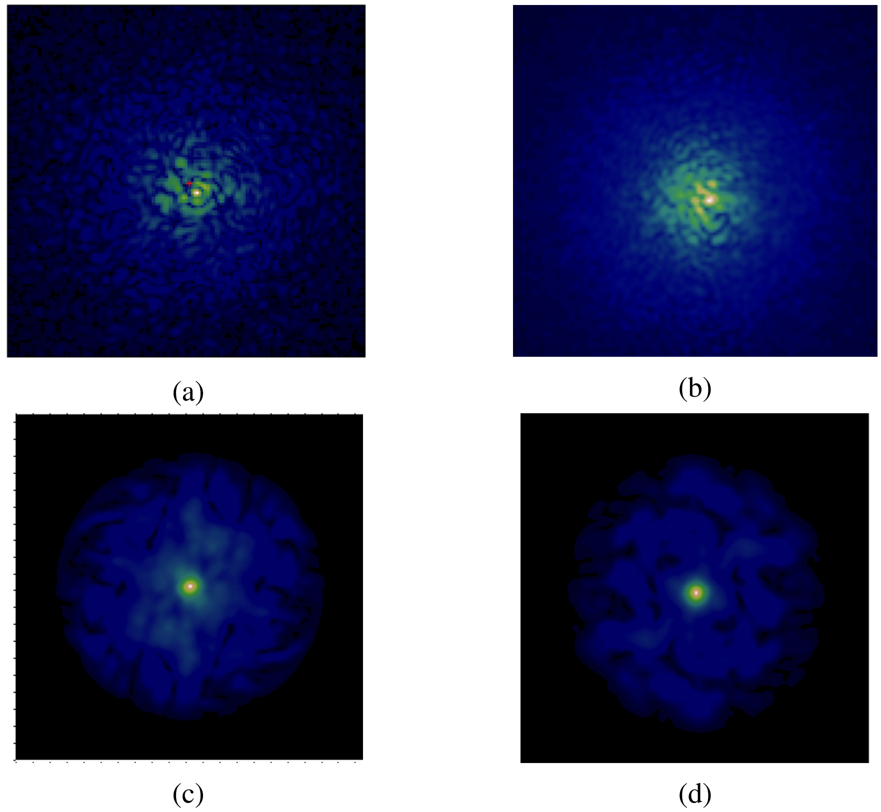

FIGURE 2.10. Short and long exposure images with corresponding OTF. (a) Short exposure image with speckles. (b) Long exposure image. (c) Instantaneous OTF. (d) Long exposure OTF.

2.5. Imaging with Adaptive Optics

This section will briefly review the fundamentals of control theory for the adaptive optics systems. The contents are extracted from Tyson (2000), Roddier (1999), Véran et al. (1997). For a detailed explanation on adaptive optics control please refer to Andersen and Enmark (2011) and Gendron and Lena (1994).

Adaptive optics (AO) is an opto-mechanical system capable of correcting the atmospheric perturbations in real time that affect the incoming wave front over the telescope pupil (Hinnen (1997)). It is designed to minimize the residual phase variance in the imaging path, i.e. to improve the overall telescope point-spread function (PSF). The input and the output of this system are respectively the wave front phase perturbations and the residual phase after correction.

Adaptive optics (AO) systems generally use the principle of phase conjugation. An optical beam is made up of both amplitude A and phase ϕ components and is described mathematically by the electric field $Aexp(-i\phi)$. Adaptive optics reverses the phase to provide compensation for the phase distortion. The corrected wave front can be directly used for imaging or for entering into another scientific instruments.

The AO system in fig. 2.11 is made of three main components, which are the crux of all modern technology AO systems.

- Wave Front Sensor (WFS): which measures the incident wave front deformations.
- Deformable Mirror (DM): which compensates the measured perturbations with the purpose to obtain an almost flat wave front entering into the science instrument.
- Real Time Controller (RTC) which controls the components of the system and converts the WFS measurements into actuator commands for the DM.

Figure 2.11 shows a conventional adaptive optics system configuration. In practice, most systems contain various supporting subsystems: i.e. beamsplitters, an auxiliary tip/tilt/jitter control system, and various other optical elements such as the collecting telescope, the imaging optics or science camera, pupil re-imaging optics, or lasers and launching optics.

2.5.1. AO phase correction

The turbulent phase $\phi_a((r,t)$ is defined as the two dimensional function representing the phase of the incoming turbulent wave-front on the telescope aperture $\mathcal{A}$ at instant t. The turbulent phase entering the AO system is corrected by the action of the deformable mirror(DM). If $\phi_m(r,t)$ is the phase configuration of the deformable mirror at instant t, the residual (corrected phase) $\phi_{\mathcal{E}}(r,t)$ is:

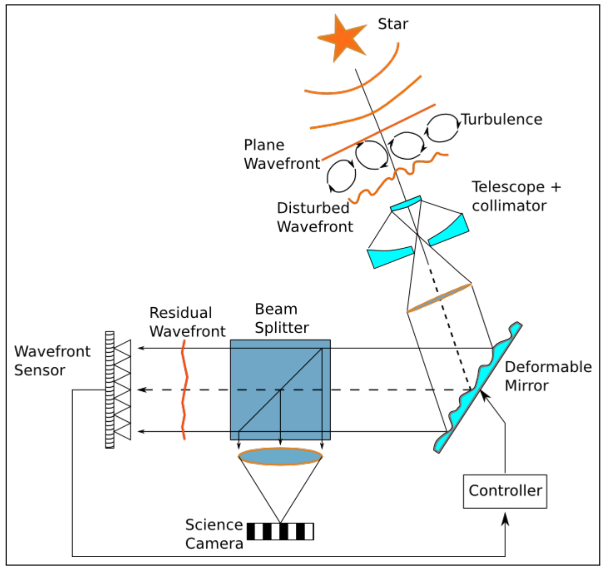

FIGURE 2.11. Conventional adaptive optics system configuration.

$$\phi_{\mathcal{E}}(r,t) = \phi_a(r,t) - \phi_m(r,t) \tag{2.80}$$

If the DM has m degrees of freedom (actuators), the attainable phase functions it can produce define a vector space $\mathcal{M}$ of dimension m which is a subspace of $\mathcal{E}$, where $\mathcal{E}$ is the set of all the possible realizations of $\phi_a(r,t)$. The DM is able to correct spatial frequencies that are lower than the inverse of the inter-actuator distance, thus high spatial frequencies that are present in $\mathcal{E}$ are not corrected by the DM and can also be treated as a subspace $\mathcal{M}^{\perp}$ of $\mathcal{E}$, that is complementary to $\mathcal{M}$. This will be called the high order component or the orthogonal component. The turbulent phase $\phi_a(r,t)$ can be decomposed as the sum of a component on $\mathcal{M}$ (*mirror low order component*) and a component on $\mathcal{M}^{\perp}$ (*high order component*). For instance

$$\phi_a(r,t) = \phi_{a\|}(r,t) + \phi_{a\perp}(r,t) \tag{2.81}$$

As the DM will be only able to compensate the mirror component of the turbulent phase, the residual phase will have the same high order component as the turbulent phase. $\phi_{\mathcal{E}}(r,t)$ may then be decomposed as:

$$\phi_{\mathcal{E}}(r,t) = \phi_{\mathcal{E}\|}(r,t) + \phi_{\mathcal{E}\perp}(r,t) \tag{2.82}$$

where $\phi_{\mathcal{E}\|}(r,t)$ is the mirror component of the residual phase, given by

$$\phi_{\mathcal{E}\|}(r,t) = \phi_{a\|}(r,t) - \phi_m(r,t) \tag{2.83}$$

The optimal instantaneous correction is obtained when $|\phi_{\mathcal{E}}(r,t)|$ is minimal, that is when $\phi_m(r,t) = \phi_{a\|}(r,t)$. The mirror modes $\{M_i(r)\}$ are the set of base functions of $\mathcal{M}$. These basis functions must accomplish orthogonality conditions, such as Zernike modes or mirror influence functions. Phase distributions on $\mathcal{M}$ can be decomposed on to mirror modes, where the coefficients of this decomposition are called *modal coordinates*

$$\phi_m(r,t) = \sum_{i=1}^{m} m_i(t)M_i(r) \tag{2.84}$$

$$\phi_{a\|}(r,t) = \sum_{i=1}^{m} a_i(t)M_i(r) \tag{2.85}$$

$$\phi_{\mathcal{E}\|}(r,t) = \sum_{i=1}^{m} \mathcal{E}_i(t)M_i(r) \tag{2.86}$$

we will refer to the m_i as the modal commands to the DM. A turbulent phase with Kolmogorov statistics can be decomposed in Zernike modes

$$\phi_a(r,t) = \sum_{i=1}^{\infty} z_i(t)Z_i(r) \tag{2.87}$$

The covariance of the Zernike expansion coefficients can be expressed as

$$\langle z_i z_k \rangle = K_{ij}\left(\frac{D}{r_0}\right)^{5/3} \tag{2.88}$$

and equivalently for a different basis, i.e.: the influence functions, 2.88 can be generalized as:

$$\langle m_i m_j \rangle = K'_{ij} \left(\frac{D}{r_0} \right)^{5/3} \tag{2.89}$$

The expression for K_{ij} was developed by Noll (1976) and Wang and Markey (1978), taking the Fourier transform of each base mode

$$Q_j(k) = \mathcal{F}\{M_j(r)\} \tag{2.90}$$

Then K_{ij} is given by:

$$K_{ij}(k) = \int \int Q_i(k)^* k^{-11/3} \delta(k = k') Q_j(k') dk' dk \tag{2.91}$$

2.5.2. Residual phase measurement

Following the scheme presented in figure 2.11, the phase, after been corrected by the DM, passes through a beam splitter, where one part of the wave front goes into the science camera and the other part enters the wave front sensor (WFS) that measures the residual phase. The WFS is a device able to sample the derivatives of the corrected phase $\phi_{\mathcal{E}}(r,t)$, at a finite number of points (sub-apertures) on the pupil. WFS measurements form a n-dimensional vector, where n is the number of sub-apertures in the case of the curvature WFS and twice this number in the case of Shack-Hartmann WFS. We denote $\mathcal{W}(\phi_{\mathcal{E}}(r,t))$ the WFS measurement of $\phi_{\mathcal{E}}(r,t)$, in the absence of any measurement error.

The WFS is intended to operate in its linear domain and can be calibrated on the mirror space $\mathcal{M}$ by sequentially exciting the DM actuators in absence of turbulence and recording the WFS response. The WFS response to the mirror modes is deduced and stored in the interaction matrix $\mathcal{D}$, which is a $n \times m$ matrix (n sub-apertures and m mirror modes). Recalling the WFS linearity, the measurement of the residual phase is

$$\mathcal{W}(\phi_{\mathcal{E}}(r,t)) = \mathcal{W}(\phi_{\mathcal{E}\|}(r,t)) + \mathcal{W}(\phi_{\mathcal{E}\perp}(r,t)) \tag{2.92}$$

and

$$\mathcal{W}(\phi_{\mathcal{E}\|}(r,t)) = \mathcal{D}\mathcal{E}(t) \tag{2.93}$$

The wavefront sensing is driven through the detection of photons coming from a guide star during a short period of time, typically from 1 to 50 ms. Measurement error $n_w(t)$ in a WFS is produced on detection, by photon noise and the imperfections on the photon detector as the dark current and read-out noise. Hence, the measurement of a WFS in the presence of error measurement is expressed as

$$w(t) = \mathcal{D}\mathcal{E}(t) + \mathcal{W}(\phi_{\mathcal{E}\perp}(r,t)) + n_w(t) \tag{2.94}$$

2.5.2.1. Curvature Sensing

From Tyson (2000), if an optical beam with aberrations is focused onto a detector such as a focal plane array, the intensity distribution is the magnitude of the Fourier transform of the field at the pupil. If the beam is slightly out of focus, the intensity pattern will be blurred. The intensity patterns of two beams, both out of focus by the same amount but of different signs, can be subtracted to reveal information about the phase aberrations. In this image plane sensor the second derivative (of the phase curvature) can be determined. A curvature sensor, like that shown in fig 2.12 optically follows Poissons equation. The difference of the two intensity patterns $I_1(r)$ and $I_2(r)$ is the difference of the wavefront curvature at r and the derivative of the wavefront $d\phi/dn$ at r in the radial direction

$$I_1(r) - I_2(r) = C\left[\nabla^2\phi(r) - \frac{d\phi(r)}{dn}\right] \tag{2.95}$$

The slope at the edge of the sub-aperture $d\phi/dn$ is a measurable boundary condition and the constant C depends upon the response of the detector and the actual defocus of the two intensity patterns.

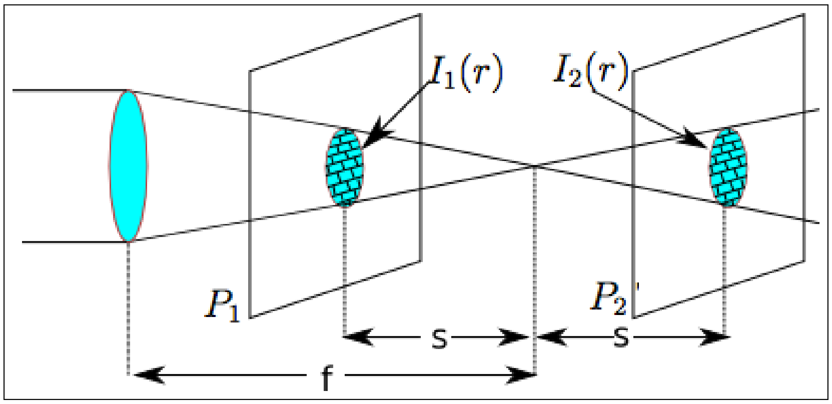

FIGURE 2.12. A curvature wavefront sensor. The difference in intensities in the offset image planes corresponds to the second derivative of the wavefront. f is the telescope focal length and s is the de-focusing distance for the offset image planes.

2.5.3. Residual phase reconstruction

From the WFS measurement an estimate of $\phi_{\mathcal{E}}(r,t)$ has to be made in order to compute the DM commands. All these operations are carried out by the real time controller. The most common technique to perform the residual wavefront estimation is to obtain the generalized inverse matrix of the interaction matrix, known as the control matrix, which is given by

$$\mathcal{D}^{+} = (\mathcal{D}^{T}\mathcal{D}^{-1})\mathcal{D}^{T} \tag{2.96}$$

It is very common to find null eigenvalues in the interaction matrix. These belong to mirror modes that give zero measurement in the WFS and are identified as invisible modes. These modes are eliminated from the mirror basis $\mathcal{M}$, and then, for the calculation of the control matrix a least square approximation can be used and thus the residual phase is also a least square estimation, denoted by $\hat{\mathcal{E}}(t)$.

$$\hat{\mathcal{E}}(t) = \mathcal{D}^{+}w(t) \tag{2.97}$$

In the ideal case of absence of measurement error and absence of high order component, the error estimation will be equal to the real error, $\hat{\mathcal{E}}(t) = \mathcal{E}(t)$, but in the real case the estimation error of the residual phase can be evaluated as

$$|\hat{\mathcal{E}}(t) - \mathcal{E}(t)| = n(t) + r(t) \tag{2.98}$$

where the propagation of the WFS measurements to the mirror modes is:

$$n(t) = \mathcal{D}^{+} n_w(t) \tag{2.99}$$

and

$$r(t) = \mathcal{D}^{+} \mathcal{W}(\phi_{\perp}(r, t)) \tag{2.100}$$

$r(t)$ is called the remaining error and is the non-zero measurement of the high order component of the turbulent phase, this is the aliasing effect because of the incomplete spatial sampling of the WFS.

2.5.4. Deformable mirror control loop

Controlling the deformable mirror is the stage that closes the control loop in the AO system. The residual phase estimation is used to calculate the value of the voltage to be applied to each actuator in the DM, which will change the DM surface and will modify the residual phase that will be measured in the next loop by the WFS. As expected, calculating the DM commands and setting the actuator voltages is not an instantaneous operation, therefore some delay will exist in the control loop. To eliminate the error in the system a controlled gain G is set in the loop. The gain value must be optimized for every specific system, alternatively the gain can be optimized for each specific mirror mode, and this last strategy is called optimized modal control. A complete description of the AO control loop theory and the modal control optimization can be found on Gendron and Lena (1994) and Andersen and Enmark (2011).

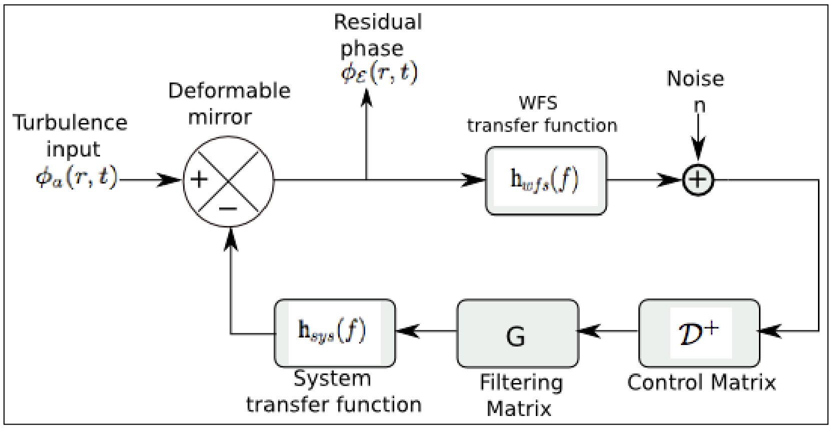

FIGURE 2.13. A curvature wavefront sensor. The difference in intensities in the offset image planes corresponds to the second derivative of the wavefront.

For the AO control loop schema shown in fig. 2.13, $\mathrm{h}_{sys}(f)$, the temporal frequency system transfer function is

$$h_{sys}(f) = \frac{exp(-2i\pi\tau f)}{2i\pi f} \tag{2.101}$$

where τ is the delay of the system.

The WFS temporal frequency transfer function is

$$h_{wfs}(f) = sinc(\pi f T_e)exp(-i\pi T_e) \tag{2.102}$$

where T_e is the sampling period.

The open loop transfer function is

$$h_{ol}(f) = h_{wfs}(f)h_{sys}(f) \tag{2.103}$$

Now defining the close loop transfer function H_{cl}, noise transfer function H_n and correction transfer function h_{corr} for the mode i as

$$
\begin{aligned}
H_{cl}(f) &= \frac{1}{1+h_{ol}(f)g_i} \\
H_n(f) &= \frac{h_{sys}(f)g_i}{1+h_{ol}(f)g_i} \\
H_{corr}(f) &= \frac{h_{sys}(f)g_i}{1+h_{ol}(f)g_i}
\end{aligned} \tag{2.104}
$$

Where g_i is the gain applied to mode i in case of modal control.

The temporal variations of the modal commands mi can be expressed in Fourier domain as

$$\mathcal{F}\{m_i(t)\} = H_{cl}(g_i, f)\mathcal{F}\{a_i(t)\} + H_{cl}(g_i, f)\mathcal{F}\{r_i(t)\} + H_n(g_i, f)\mathcal{F}\{n_i(t)\} \tag{2.105}$$

$f_{cl}(g_i)$) is the cut-off frequency at -3dB for the closed-loop transfer function and represents the temporal bandwidth of the system, which is able to respond to quick changes in the turbulent phase. Decreasing g_i decreases f_{cl} but also decreases the effect of the errors in the estimation of the residual phase, increasing g_i has the inverse effect on the system, and therefore g_i has to be set to an optimal trade-off. If no modal optimization is to be applied, then g_i is the same for all the mirror modes and equal to a general system gain G.

Combining 2.80 and 2.105:

$$\mathcal{F}\{\mathcal{E}_i(t)\} = H_{corr}(g_i, f)\mathcal{F}\{a_i(t)\} - H_{cl}(g_i, f)\mathcal{F}\{r_i(t)\} - H_n(g_i, f)\mathcal{F}\{n_i(t)\} \tag{2.106}$$

2.5.5. AO error sources

Although adaptive optics is effective in correcting the atmospheric perturbations, such provided correction is not perfect. The main error sources come from turbulence model, AO components, calibrations and external factors. Denoting σ^2_{res} as the variance of the residual phase (Costille, 2009), then

$$\sigma^2_{res} = \sigma^2_{scint} + \sigma^2_{aniso} + \sigma^2_{chrom} + \sigma^2_{alias} + \sigma^2_{noise} + \sigma^2_{fit} + \sigma^2_{t} + \sigma^2_{calib} + \sigma^2_{aberr} + \sigma^2_{exo} \quad (2.107)$$

The first three terms in 2.107 refer to atmospheric turbulence model errors:

- Scintillation (σ^2_{scint}): The amplitude variations of the wave front that are not considered in the Kolmogorov hypothesis, which supposes an homogeneous amplitude.
- Anisoplanatism (σ^2_{aniso}): This phenomena is associated to the angular decorrelation of the turbulent phase between two field directions. The quality of the correction is degraded on field positions that are furthest from the correction direction. Notwithstanding, there is a new branch of wide field AO that reduces this problem (Lloyd-Hart & Milton, 2003).
- Chromatism (σ^2_{chrom}): Refraction effect variation due to index of refraction variations as a function of wavelength.

The next four terms correspond to AO system errors:

- Aliasing (σ^2_{alias}): Measurement error due to the finite spatial sampling of the WFS over the residual phase with high spatial frequency components.
- Noise (σ^2_{noise}): Another measurement error coming from photon noise in the detector and detector imperfections as dark current and read-out noise.
- Fit (σ^2_{fit}): The DM is not able to reproduce all the spatial frequencies present in the turbulence and is limited by the number of actuators in the pupil. The high order spatial frequencies cannot be compensated.
- Loop delay (σ^2_{t}) : Is the accumulation of delays in the AO control loop due to measuring, computation and correction. This delay causes that the correction is never made on the same measured wave front.

The next two terms in 2.107 are errors due to system calibration

- Calibration (σ^2_{calib}): Are the errors coming from the interaction matrix measurement misregistration and reference sources.
- Aberrations (σ^2_{aberr}): Correspond to non common path aberrations between the WFS and science camera, and static aberrations in the telescope optics that are not corrected by the AO.

The last term is the exogenous error (σ^2_{exo}) and makes reference to environmental factors which disturb the AO system operation as mechanical vibrations that affect the wave front measuring.

2.5.6. AO image properties

From the previous section it was concluded that AO system correction is non-perfect because of the existence of many error sources, but images obtained in presence of turbulence with AO correction are better in quality than those acquired without correction, nevertheless AO corrected images won't necessarily reach the limit of diffraction quality.

Figure 2.14 shows an image of cumulus M13 that illustrates the concept of AO imaging. In the center, where the wide field picture of the cumulus is shown, a section of the center is zoomed in. On the bottom-right the detail is shown without AO correction, and on the top-right the detail is shown with AO correction which is clearly improved. It can be seen in the long exposure, AO corrected image, a remanent halo surrounding the star's image.

AO allows the correction of low order spatial frequencies for an image obtained from a telescope and the partial reconstruction of high order spatial frequencies, up to the telescope cut-off frequency. The grade of correction made by an AO system can be characterized by measuring the Strehl number.

Figure 2.15 illustrates the improvement that AO correction makes over a short exposure and a long exposure image. Figure 2.15a shows an image with short exposure and AO compensation. In 2.15b for an image with no AO compensation (red) the profile of

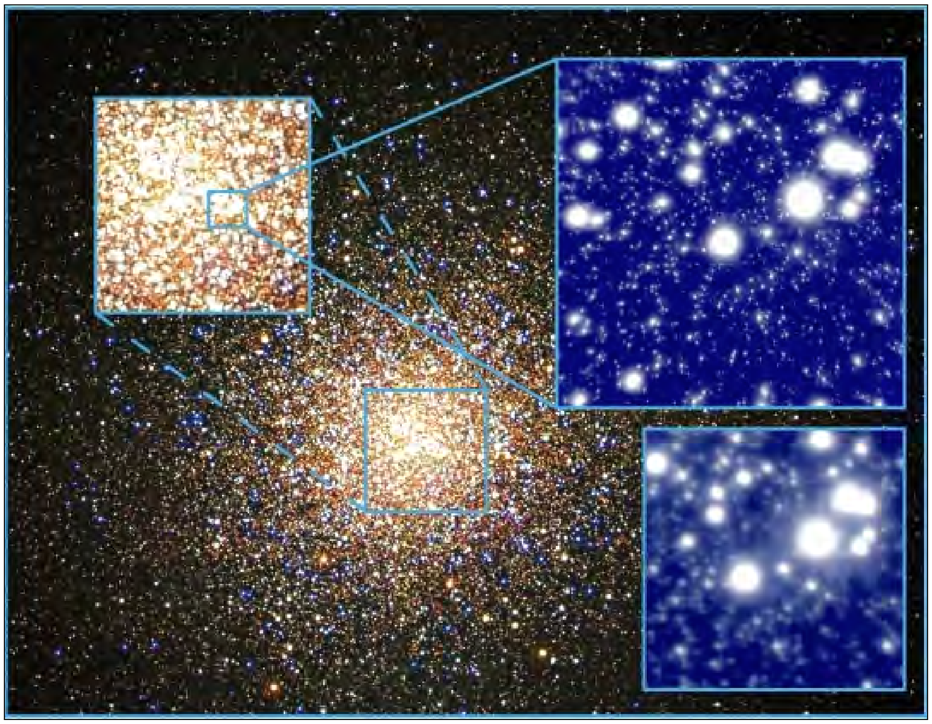

FIGURE 2.14. M13 cumulus image with AO. Credit: Gemini Observatory and Canada-France-Hawaii Telescope/Coelum/Jean-Charles.

the speckles can be seen off-axis; for an image with AO compensation (blue), the profile resembles an asymmetric diffraction limited PSF, the sidelobes are modulated by the remanent speckles.

Figure 2.15c shows an image with long exposure and AO compensation. In 2.15d for the AO compensated image (blue), the core has approximately the same width as the diffraction limit image(black), and the halo is dominating over the side lobes, the halo is the result of the integration of residual speckles after the compensation. From Gladysz et al. (2012), the size of the halo in both, a seeing-limited PSF and a compensated PSF is determined by r_0. Compensation transfers light from the halo (of angular scale $\approx \lambda/r_0$) to the core (of angular scale $\approx \lambda/D$) changing the relative peak intensities of both components but not substantially affecting their widths.

Figure 2.16 shows the effect of AO compensation on the OTF and the intensity distribution. The case of imaging without AO compensation is presented in 2.16(a), note that

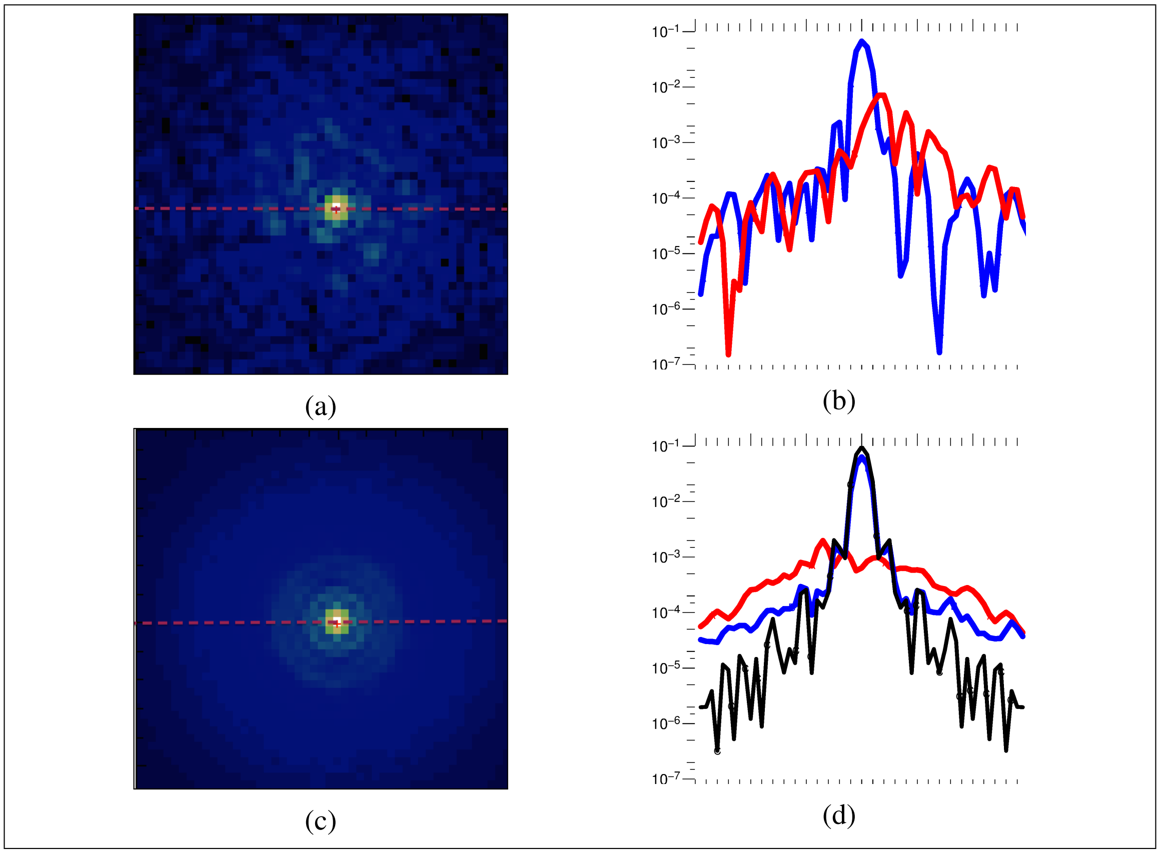

FIGURE 2.15. Short and long exposure image for non-compensated imaging and AO compensated imaging (The dashed red line in (a) and (c) indicates the cross-cut correspondent to the profiles shown in (b) and (d) . (a) (log scale) Short exposure AO corrected image. (b) (log scale) Profile for short-exposure non-compensated image with speckles (red) and short exposure AO corrected image (blue). (c) (log scale) Long exposure AO corrected image. (d) (log scale) Diffraction limited image (black), long exposure non compensated image (red), long exposure AO image (blue).

the spatial frequencies between r_0/λ and D/λ in the OTF are attenuated; this causes the loss of image contrast with significant intensity spread beyond the angular extent of the diffraction-limited image. On 2.16(b), the case for partial AO compensation is presented; the higher spatial frequencies in the OTF are less attenuated, which in turns reduces the spread of intensite in the image. 2.16(c) shows the case for good AO compensation; a discontinuity can be seen in the very low range of spatial frequencies, this discontinuity is due to the aliasing in the system. In the intensity distribution the remnant halo, is due to the integration of residual speckles.

If the long exposure PSF of the system is known and following equation 2.29, it should be possible to deconvolve the AO corrected image with the long exposure PSF and then obtaining a sharper version of the image, without the halo. To make this possible two problems have to be solved: Characterize the long exposure PSF and find an appropriate deconvolution algorithm.

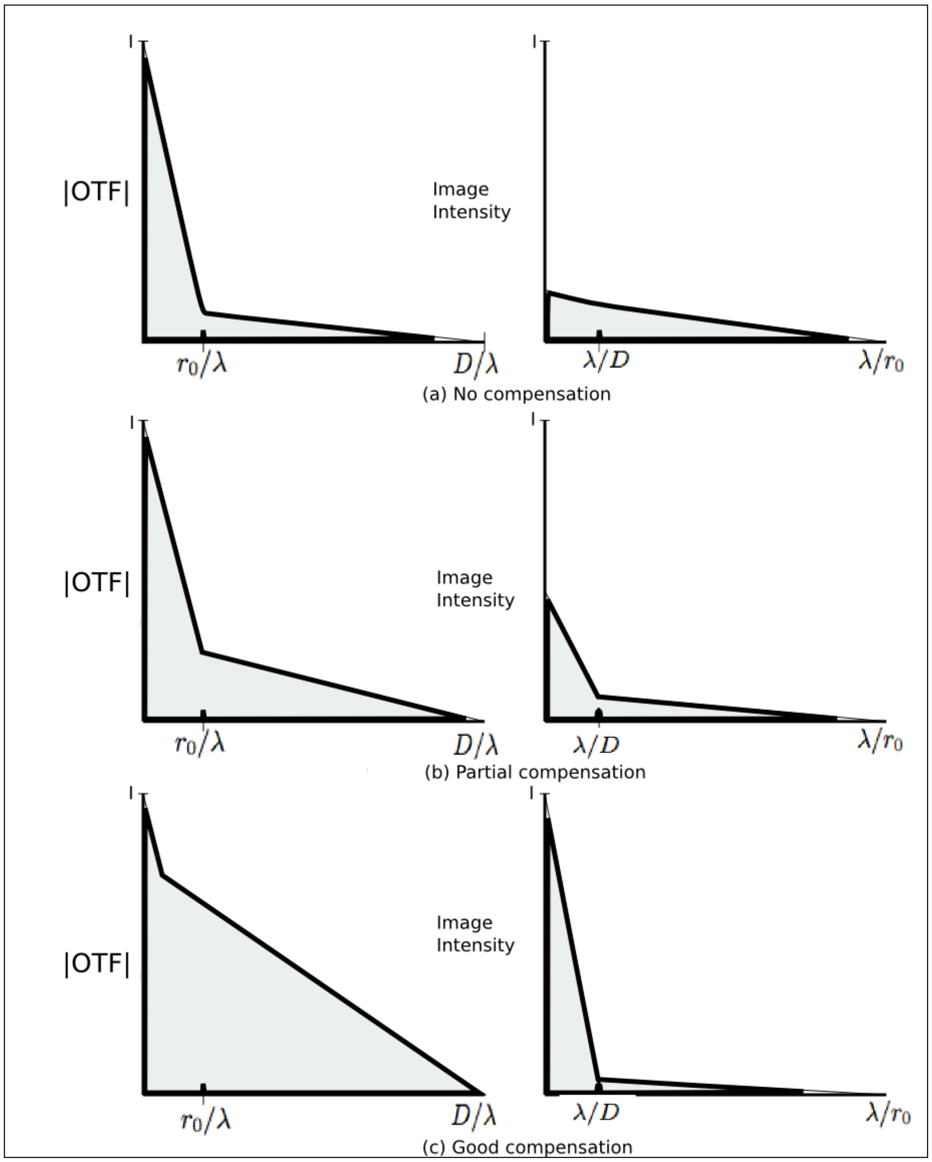

FIGURE 2.16. The effect of increasing AO compensation on the OTF (left) and the PSF (right).

2.6. Deconvolution and PSF estimation

From the previous section, it was seen that the loss of the high-frequency portion of the spectrum caused loss of image contrast, as the intensity of sharp objects spreads beyond the angular extent of the object diffraction limited image. This spreading means tah fine structures in the image will be smeared out and hard to detect. Faint companions are similarly hard to see both because of the large wings of the primary and the identical spreading out of the companions light. Note the OTF is generally a complex number, so for short-exposure imaging, where the PSF is asymmetric and speckled, or for certain fixed optical aberrations, the filtering of any object spectral component includes multiplication by the phase of the OTF at that frequency. Attempts to mathematically invert this filtering and restore spectral amplitudes to at least the diffraction-limited level are referred to as deconvolution processing.

Deconvolution is the undoing of convolution and it tries to find a solution for f in

$$f * g = h + n \tag{2.108}$$

given g and h, where n is noise. Deconvolution will not usually have a unique solution even in the absence of noise. As a process, deconvolution is algorithm-based and is used for signal and image processing. Specifically for imaging, reformulating 2.29 and including noise $n(x, y)$ in the image formation

$$I(x, y) = PSF(x, y) * O(x, y) + n(x, y) \tag{2.109}$$

The original object O is computed from the image and the PSF. Due to the presence of noise and the cut-off spatial frequency of the imaging system, generally there is not a unique and stable solution. Using the Fourier transform convolution property to compute the deconvolution is tempting because of its simplicity, namely

$$\mathcal{F}\{O\}(f_x, f_y) = \frac{\mathcal{F}\{I\}(f_x, f_y)}{OTF(f_x, f_y)} - \frac{N(f_x, f_y)}{OTF(f_x, f_y)} \tag{2.110}$$

with $N(f_x, f_y)$ the Fourier transform of the noise. This last expression poses a big problem for solving the deconvolution, as spatial frequencies close and over the cut-off frequency the values of the OTF are very small making the noise term $\frac{N(f_x,f_y)}{OTF(f_x,f_y)}$ to be dominant, causing noise amplification at high spatial frequencies. Constrains derived from prior information about the object applied to the image reconstruction can mitigate the noise amplification but also limits the result quality. This process is called regularization. Typical deconvolution algorithms are: Wienner (non-iterative), and Richardson-Lucy (iterative(.

When the PSF of the system is considered to be same for each point in the image then the convolution with the object is called a spatially invariant PSF convolution. For a PSF that changes, depending on its position across the image, the convolution is called a spatially variant PSF convolution. There are different types of deconvolution algorithms that should be applied according to the case. Whenever the PSF of the system is not known, blind deconvolution methods have to be applied. In simple words, this is equivalent to trying different given PSFs and verifying which of them make an improvement in the image. If the PSF is known, then a non-blind deconvolution process should be applied. For blind deconvolution the process can be very inefficient, thus the problem of estimating the PSF of a system has been investigated in image processing applied to the deblurring of images acquired out-of- focus or distorted by shaking during acquisition. For a complete discussion on deconvolution techniques applied to astronomy please read Tyler (2001).

2.7. PSF reconstruction from AO telemetry

The contents of this section are directly taken from Véran et al. (1997), which is the seminal work for PSF reconstruction in AO systems.

In astronomy, the PSF is usually estimated from imaging a star, which acts as point source. However, this method is not always a good approximation as the PSF of a telescope depends on many factors that can change along the observation, specially the atmospheric conditions which outdates the PSF in use. Furthermore, imaging a star for PSF measurement purposes consumes precious observation time for science observations. Ideally, the estimated PSF has to be computed from data which is synchronized with the observation. Here the compensated speckles holography method can be used correcting each short exposure image with the measurements from the WFS obtaining an improved long exposure image. This is obviously not applicable when only the long exposure image is available. For the latter case,Véran et al. (1997) try to estimate the PSF from the telemetry data originated by the AO system. This idea was originally applied on PUEO, the Canada-France-Hawaii Telescope adaptive optics system, and has been at the basis of further development for various telescopes and AO systems (Clénet et al., 2008). However, this approach has a series of challenging mathematical and computational challenging problems that have limited its further development. This technique, has been called PSF reconstruction, is the problem that motivated this thesis.

2.7.1. Long exposure OTF and long exposure PSF for AO corrected wavefront

The long exposure PSF is the inverse Fourier transform of the long exposure OTF

$$\big\langle PSF(r)\big\rangle = \mathcal{F}^{-1}\{\big\langle OTF(f_x, f_y)\big\rangle\} \tag{2.111}$$

Recalling 2.75, the instantaneous OTF for an AO corrected wave front is written as

$$OTF(f,t) = \frac{1}{S}\int\int_A A(r)A(r+\Delta r)exp[i\phi_{\mathcal{E}}(r,t)]exp[-i\phi_{\mathcal{E}}(r+\Delta r,t)]dr \tag{2.112}$$

where $\phi_{\mathcal{E}}$ is residual phase as defined by 2.80 and S is the telescope's aperture area. Assuming that the residual phase has Gaussian statistics at any position and that the integration time is long enough to replace the statistical average by the temporal average, then the long exposure OTF is:

$$\langle OTF(f_x, f_y)\rangle = \frac{1}{S}\int\int_A A(r)A(r+\Delta r)exp[-\frac{1}{2}D_{\phi_\mathcal{E}}(r,\Delta r)]dr \tag{2.113}$$

and from 2.48, the structure function of the residual phase:

$$D_{\phi_\mathcal{E}}(r,\Delta r) = \langle|\phi_\mathcal{E}(r,t) - \phi_\mathcal{E}(r+\Delta r,t)|^2\rangle \tag{2.114}$$

Unlike the case of a phase with Kolmogorov statistics, the residual phase is not spatially stationary, thus the structure function depends on the separation Δr and the position r. Calculating $D_{\phi_\mathcal{E}}(r,\Delta r)$ is computationally very demanding as it requires the averaging of 4 dimensional functions. However, it is possible to replace $D_{\phi_\mathcal{E}}(r,\Delta r)$ by $\bar{D}_{\phi_\mathcal{E}}(\Delta r)$

$$\bar{D}_{\phi_\mathcal{E}}(\Delta r) = \frac{\int\int_A A(r)A(r+\Delta r)D_{\phi_\mathcal{E}}(r,\Delta r)dr}{\int\int_A A(r)A(r+\Delta r)dr} \tag{2.115}$$

Then, the long exposure OTF is expressed as:

$$\langle OTF(f_x, f_y)\rangle = exp[-\frac{1}{2}\bar{D}_{\phi_\mathcal{E}}(\Delta r)]\int\int_A A(r)A(r+\Delta r)dr \tag{2.116}$$

Changing $D_{\phi_\mathcal{E}}(r,\Delta r)$ for $\bar{D}_{\phi_\mathcal{E}}(\Delta r)$, assumes that the dispersion along r is small enough so that the exponential of the mean can be replaced by the mean of the exponential. As the exponential is a convex function, the OTF will be under-estimated, but it has been proved that only the lowest values of the OTF, corresponding to the highest spatial frequencies, are affected by the approximation. Bearing this, the quality loss of the reconstructed PSF is not significant . With this change, the computation of $\langle OTF\rangle(f_x, f_y)$ requires to average two-dimensional functions only.

Recalling 2.82, $\bar{D}_{\phi_\mathcal{E}}(\Delta r)$ can be represented by:

$$\bar{D}(\Delta r) = \bar{D}_{\phi\mathcal{E}\parallel}(\Delta r) + \bar{D}_{\phi\mathcal{E}\perp}(\Delta r) + 2\frac{\int\int_A A(r)A(r+\Delta r)\left\langle[\phi_{\mathcal{E}\parallel}(r,t)-\phi_{\mathcal{E}\parallel}(r+\Delta r,t)][\phi_{\mathcal{E}\perp}(r,t)-\phi_{\mathcal{E}\perp}(r+\Delta r,t)]\right\rangle dr}{\int\int_A A(r)A(r+\Delta r)} \tag{2.117}$$

In 2.117, the third term (cross term) is not rigoroulsy zero because $\phi_{\mathcal{E}\parallel}$ and $\phi_{\mathcal{E}\perp}$ may be correlated through the remaining error. It is assumed that this cross term is negligible. Simulations show that this assumption is fully granted for systems such as PUEO (Véran et al., 1997).

Equation 2.116 can be expressed as the product of three contributions:

$$\left\langle OTF(f_x, f_y)\right\rangle = OTF_{\mathcal{E}\parallel}OTF_{\mathcal{E}\perp}OTF_{tel} \tag{2.118}$$

with OTF_{tel} being the telescope OTF, namely

$$OTF_{tel}(f_x, f_y) = \frac{1}{S}\int\int_A A(r)A(r+\Delta r)dr \tag{2.119}$$

In turn, the component $OTF_{\mathcal{E}\perp}$ is the high-frequency spatial phase contribution:

$$OTF_{\mathcal{E}\perp}(f_x, f_y) = exp(-\frac{1}{2}\bar{D}_{\phi\perp}(\Delta r)) \tag{2.120}$$

with $\bar{D}_{\phi\perp}$ given by

$$\bar{D}_{\phi\perp} = \frac{\int\int_A A(r)A(r+\Delta r)|\phi_{\mathcal{E}\perp}(r,t) - \phi_{\mathcal{E}\perp}(r+\Delta r,t)|^2 dr}{\int\int_A A(r)A(r+\Delta r)dr} \tag{2.121}$$

Whose calculation is facilitated using the equivalent formulation in the Fourier domain:

$$\bar{D}_{\phi\perp}(r, \Delta r) = \frac{\mathcal{R}\{\mathcal{F}^{-1}\{2 * \mathcal{R}\{\mathcal{F}\{\phi(r)^2 A(r)\}\mathcal{F}^*\{A(r)\}\} - |\mathcal{F}\{\phi(r)A(r)\}|^2\}\}}{\mathcal{R}\{\mathcal{F}^{-1}\{\mathcal{F}\{A(r)\}\mathcal{F}^*\{A(r)\}\}\}} \tag{2.122}$$

Function $OTF_{\mathcal{E}\parallel}$ represents the contribution of the mirror component of the residual phase to the long exposure OTF:

$$OTF_{\mathcal{E}\|}(f_x, f_y) = exp[-\frac{1}{2}\bar{D}_{\phi\mathcal{E}\|}(\Delta r)] \tag{2.123}$$

where $\bar{D}_{\phi_{\mathcal{E}\|}}$ is expressed as

$$\bar{D}_{\phi\mathcal{E}\|}(\Delta r) = \sum_{i,j}^{N} \langle \mathcal{E}_i \mathcal{E}_j \rangle U_{ij}(\Delta r) \tag{2.124}$$

where the U_{ij} are functions of the mirror modes:

$$U_{ij}(\Delta r) = \frac{\int\int_A A(r)A(r+\Delta r)[M_i(r) - M_i(r+\Delta r)][M_j(r) - M_j(r+\Delta r)]dr}{\int\int_A A(r)A(r+\Delta r)dr} \tag{2.125}$$

If the mirror modes are Zernike polynomials or Karhunen-Loeve (KL) functions, U_{ij} can be obtained analytically. For other modes these functions have to be computed numerically. In addition, using the Fourier transform and the properties of the correlation function, the $U_{ij}(\Delta r)$ functions can be computed as:

$$U_{ij}(\Delta r) = \frac{\mathcal{F}^{-1}\left(2\mathcal{R}(\mathcal{F}(M_i M_j A)\mathcal{F}^*(A) - \mathcal{F}(M_i A)\mathcal{F}(M_j A))\right)}{\mathcal{F}^{-1}\left(|\mathcal{F}(A)|^2\right)} \tag{2.126}$$

Finally notice that after the DM, the corrected wave front, passes through a beam splitter that sends part of the wave front to the imager, and the remainder to the WFS. Non-common path aberrations that are not seen by the WFS could exist and affect the final image, therefore they must be taken into account in the PSF. The non-common path aberrations are of static nature and may be calibrated as a static PSF, denoted $PSF_s(r)$, and this static PSF is obtained by imaging a point source in absence of turbulence, with the DM flat, having zero measurements at the WFS.

The OFT of the telescope is replaced by the OTF from the static PSF: $OTF_s(f_x, f_y) = \mathcal{F}\{PSF_s(x, y)\}$.

The long exposure OTF is finally expressed as:

$$\langle OTF(f_x, f_y) \rangle = OTF_{\mathcal{E}\|}(f_x, f_y) OTF_{\mathcal{E}\perp}(f_x, f_y) OTF_s(f_x, f_y) \tag{2.127}$$

2.7.2. Estimation of $OTF_{\epsilon\|}$

The long exposure OTF component due to mirror modes is computed from $\mathcal{C}_{\mathcal{E}\mathcal{E}}$, the covariance matrix of the modal coordinates of $\phi_{\mathcal{E}\|}$.The computation of $\mathcal{C}_{\mathcal{E}\mathcal{E}}$ is based on $\hat{\mathcal{E}}(t)$, that is the estimation of $\mathcal{E}$ made by the RTC as described in 2.97. Hence, recalling 2.98:

$$\hat{\mathcal{E}}(t) = \mathcal{E}(t) + n(t) + r(t) \tag{2.128}$$

where $n(t)$ is the WFS measurement error propagated onto the mirror modes and $r(t)$ is the remaining error coming from the high-frequency spatial phases affecting the measurement of $\phi_{\mathcal{E}\|}$. The measurement error n has no temporal correlation with either $\mathcal{E}(t)$, or $r(t)$. 2.128 can be expressed in terms of covariance matrices as:

$$\mathcal{C}_{\mathcal{E}\mathcal{E}} = \mathcal{C}_{\hat{\mathcal{E}}\hat{\mathcal{E}}} - \mathcal{C}_{nn} - \mathcal{C}_{rr} - 2\mathcal{C}_{\mathcal{E}r} \tag{2.129}$$

$\mathcal{C}_{\hat{\mathcal{E}}\hat{\mathcal{E}}}$ can be computed from $\mathcal{C}_{ww}$, the covariance matrix of the WFS measurements.

From 2.97:

$$\mathcal{C}_{\hat{\mathcal{E}}\hat{\mathcal{E}}} = \mathcal{D}^{+} \mathcal{C}_{ww} (\mathcal{D}^{+})^T \tag{2.130}$$

In a similar way, $\mathcal{C}_{nn}$ can be computed from $\mathcal{C}_{n_w n_w}$, the covariance matrix of the measurement error:

$$\mathcal{C}_{nn} = \mathcal{D}^{+} \mathcal{C}_{n_w n_w} (\mathcal{D}^{+})^T \tag{2.131}$$

Calculation for $\mathcal{C}_{n_w n_w}$ is specific to the WFS. For $-\mathcal{C}_{rr} - 2\mathcal{C}_{\mathcal{E}r}$, an element (i, j) of the matrix can be expressed as:

$$-(\mathcal{C}_{rr})_{ij} - 2(\mathcal{C}_{\mathcal{E}r})_{ij} = (\mathcal{C}_{rr})_{ij} - 2\int H^*_{corr}(g_i, f) S_{r_i r_j}(f)df - 2\int H^*_{corr}(g_i, f) S_{a_i r_j}(f)df \tag{2.132}$$

Where $S_{r_i r_j}$ and $S_{a_i r_j}$ are temporal cross-spectrums. In general, except for very faint stars, the integral terms will be negligible with regards to $(\mathcal{C}_{rr})_{ij}$. 2.129 can be expressed as:

$$\mathcal{C}_{\mathcal{E}\mathcal{E}} \approx \mathcal{C}_{\hat{\mathcal{E}}\hat{\mathcal{E}}} - \mathcal{C}_{nn} + \mathcal{C}_{rr} \tag{2.133}$$

2.7.3. Estimation for $OTF_{\mathcal{E}\perp}$ and $\mathbf{C}_{rr}$

The contributions of the high order phase components $\phi_\perp$ to the long exposure OTF are calculated from $\bar{D}_{\phi\perp}$, the structure function of $\phi_\perp$ using 2.122. On the other hand, C_{rr}, the covariance matrix of the orthogonal residual phase depends on the statistics of $\phi_\perp$, but because the limited spatial sampling of the WFS, no information about $\phi_\perp$ can be obtained from the WFS measurements, however high order phases are not affected by the AO system thus Kolmogorov statistics can be assumed and it can be concluded that $D_{\phi\perp}$ and $\mathcal{C}_{rr}$ depend only on the value of D/r_0. Supposing that D/r_0 is known, then to calculate these parameters is possible through analytical methods but limited to mirror space generated by Zernike polynomials or KL functions, with no central obscuration. For the general case, random phase screens with Kolmogorov statistics can be simulated and by extracting the high order component of each of them, a large number of realizations of $\phi_\perp$ can be generated. $D_{\phi\perp}$ can be estimated by replacing in equation 2.121 the statistical average by an average over all the realizations. For $\mathcal{C}_{rr}$, a simulation of the WFS can be done in order to compute $\mathcal{W}(\phi_\perp(r,t))$, and using equation 2.100, a large number of realizations of $r(t)$ can be obtained and accumulated to give an estimate of $\mathcal{C}_{rr}$.

$D_{\phi\perp}$ and $\mathcal{C}_{rr}$ need to be calculated just once, at $D/r_0 = 1$ for instance, as they can be scaled to any D/r_0.

$$D_{\phi\perp}(r, \Delta r) = (D_{\phi\perp}(r, \Delta r))_{D/r_0=1}(\frac{D}{r_0})^{\frac{5}{3}} \tag{2.134}$$

$$\mathcal{C}_{rr} = (\mathcal{C}_{rr})_{D/r_0=1}(\frac{D}{r_0})^{\frac{5}{3}} \tag{2.135}$$

2.7.4. Estimation of D/r_0

For each mirror mode, D/r_0 can be estimated using 2.89

$$(D/r_0)_i = (\frac{\sigma^2_{a_i}}{K'_{ii}})^{\frac{3}{5}} \tag{2.136}$$

where $\sigma^2_{a_i}$ is the statistical variance of the mode coefficient in the turbulent phase and the expression for K'_{ii} is given by 2.91. Thus, having one estimation of D/r_0 per each actuator, combining them provides a more accurate estimation. Tip an tilt modes should be discarded as they are strongly dependant of the outer scale of the turbulence. It has been proven that the most robust method is to take the median for D/r_0 from the set of estimations: $(D/r_0)_i$.

The relationship between the modal coordinates $a_i(t)$ of $\phi_{a\|}$ and the modal commands to the DM, $m_i(t)$ is given by 2.105. Recalling that the measurement error $n(t)$ has no temporal correlation with $\mathcal{E}(t)$ and $r(t)$ and also considering that the remaining error comes from the high order spatial frequencies of the turbulence, then the covariance $\langle a_i r_i \rangle$ is much smaller than the variance $\sigma^2_{a_i}$, then from correlation properties:

$$\sigma^2_{m_i} = \int |H_{cl}(g_i, f)|^2 S_{a_i a_i}(f) df + \int |H_{cl}(g_i, f)|^2 S_{r_i r_i}(f) df + \sigma^2_{n_i} \int |H_n(g_i, f)|^2 df \tag{2.137}$$

Where $S_{a_i a_i}(f)$ is the power spectrum (Fourier transform) of the autocorrelation of $a_i(t)$ and $S_{r_i r_i}(f)$ is the power spectrum of the autocorrelation of $r_i(t)$.

This last equation states that the variance of the mirror commands $\sigma^2_{m_i}$ is:

a) the variance of the mirror modes in the turbulence $\sigma^2_{a_i}$, filtered by the closed-loop transfer function; b) the variance of the remaining error $\sigma^2_{r_i}$, also filtered by the closed-loop transfer function, and c) the variance of the measurement error $\sigma^2_{n_i}$, filtered by the noise transfer function.

If the system bandwidth is high enough so that $f_{cl}(g_i) > f_{\mathcal{M}}$, then the filtering action of the closed-loop transfer function is negligible and therefore, a_i can be formulated as:

$$\sigma^2_{a_i} = \sigma^2_{m_i} - \sigma^2_{r_i} - \sigma^2_{n_i} \int |H_n(g_i, f)|^2 df \tag{2.138}$$

$\sigma^2_{m_i}$ is calculated from the command applied to the DM, $H_n(g_i, f)$ is analytically known from equation 2.105 and $\sigma^2_{n_i}$ is obtained from equation 2.131. The problem is to obtain $\sigma^2_{r_i}$, which is a function of D/r_0. This requires to have an iterative method for estimating both $\sigma^2_{r_i}$ and D/r_0. The following heuristic (Véran et al., 1997) has been found to provide good convergence into a solution:

- set $D/r_0 = 0$
- Repeat until convergence:
  - Compute $\sigma^2_{r_i}$ using 2.135
  - Compute $\sigma^2_{a_i}$ using 2.138
  - Compute D/r_0 using 2.136
  - Take the new estimate or D/r_0 from the median of $(D/r_0)_i$ for all the non-excluded modes.

2.7.5. Curvature WFS noise

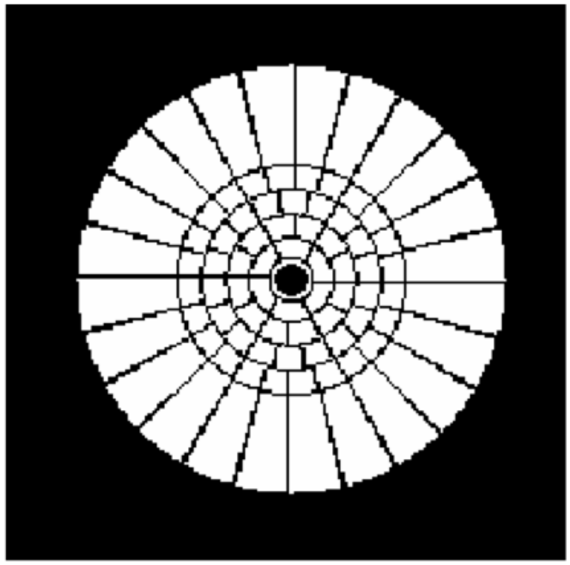

FIGURE 2.17. Curvature WFS.

The noise, specifically in curvature WFS is covered here as it is critical for the study case in this thesis. The curvature WFS is made by an intrafocal plane and an extra focal plane that are separated by a distance l from the focal plane. Taking the illumination contrast on both planes, the measurement in absence of any measurement error is:

$$W(t) = \frac{N_1(t) - N_2(t)}{N_1(t) + N_2(t)} = \frac{N_D(t)}{N_S(t)} \tag{2.139}$$

where $N_1(t)$ is the number of photons in a sub aperture in the intrafocal plane and $N_2(t)$ is the number of photons in the same sub aperture but detected on the extra focal plane. $W(t)$ is related to the wave front average local curvature of the measured wave front at the sub- aperture. $W(t)$ is a random variable with mean value 0. $N_D(t)$ mean value is 0 and $N_S(t)$ mean value is $N(t) = \left\langle N_1(t) + N_2(t) \right\rangle$, which is the average number of photons in the aperture. As the WFS measures the corrected phase, it is expected to have small fluctuations on N_S, then if $\sigma_{N_S} \ll N$, σ_W^2 can be approximated by:

$$\sigma_W^2 \approx \frac{\sigma_{N_D}^2}{N^2} \tag{2.140}$$

In the presence of measurement errors, the WFS measurement for the given sub-aperture becomes:

$$w(t) = \frac{n_1(t) - n_2(t)}{n_1(t) + n_2(t)} = \frac{N_d(t)}{N_s(t)} \tag{2.141}$$

The error measurement in a curvature WFS is originated mainly by photon noise, which has Poisson statistics. Only when N is very small the dark current and read-out noise could become significant. The measured intensities for intra-focal plane, $n_1(t)$, and extra-focal plane,$n_2(t)$, can be modeled as independent Poisson processes with mean N_1 and N_2 respectively, then with $s(t) = n_1(t) + n_2(t)$, it follows that:

$$N = \langle s(t) \rangle \tag{2.142}$$

$$\sigma^2_{N_S} = \sigma^2_{N_s} - N \tag{2.143}$$

$$\sigma^2_{N_D} = \sigma^2_{N_d} - N \tag{2.144}$$

Combining 2.144 with 2.140 the variance of the noiseless measurement is expressed as

$$\sigma^2_W \approx \frac{\sigma^2_{N_d}}{N^2} - \frac{1}{N} \tag{2.145}$$

And then the variance of the measurement noise is

$$\sigma^2_{n_w} = \sigma^2_w - \sigma^2_W \tag{2.146}$$

WFS outputs per sub-aperture are $N_s(t)$ and $N_d(t)$, so using the above relationships, $\sigma^2_{n_w n_w}$ can be calculated for each sub-aperture and form $\mathcal{C}_{n_w n_w}$ as a diagonal matrix.

Typically, $\sigma^2_{N_s} \gg \sigma^2_{N_S}$ due to the photon noise. However, if the mean flux on the sub-aperture is so high that $\sigma_{N_s} \ll N$, then σ^2_w can be expressed as

$$\sigma^2_w \approx \frac{\sigma^2_d}{N^2} \tag{2.147}$$

which combined with 2.145 and 2.146 defines the variance of the measurement error as:

$$\sigma_{n_w} = \frac{1}{N} \tag{2.148}$$

which is the typical expression for the photon noise on any WFS. However, 2.146 offers a better accuracy for low flux levels.

3. A SURVEY ON PSF RECONSTRUCTION

3.1. Introduction

PSF Reconstruction (PSF-R) has become a desirable tool for diffraction limited astronomical AO science, used for photometry or astrometry of crowded star fields as well as for deconvolution of extended objects. Regarding that the astronomy community is foreseeing the next generation of extremely large telescopes (ELTs) and that AO systems are strictly necessary for their operations, PSF-R will play a key role in astronomical science.

PSF-R is based on the post-processing of AO telemetry data and models of WFS measurement noise, WFS aliasing and DM fitting. Véran et al. (1997), proposed this PSF-R technique for AO systems with a bright natural guide star, and he successfully tested it on PUEO at CFHT (Canada-France-Hawaii Telescope).

During the last 16 years, researchers have worked to incorporate improvements and additional features to Véran's original concept, and have covered problems as the noise estimation for Shack-Hartmann WFS, the PSF field dependence, the anisoplanatism effect, algorithm optimization and reconstruction for AO Laser Guide Stars systems.

Observatories sush as Gemini, Keck, TMT and Paranal's VLT are implementing PSF-R techniques for wide field AO systems such as MCAO (Multi Conjugated AO) and GLAO (Ground Layer AO). During 2011, successful implementations have been reported at Keck Observatory (Jolissaint et al., 2011). In 2013, Exposito et al. introduced a new theoretical method for PSF-R based on a maximum likelihood approach. Nowadays, PSF-R is a major topic in conferences such as *AO4ELT* and *SPIE Astronomical Telescopes and Instrumentation*.

The main parameters involved in the PSF reconstruction algorithm are the guide star magnitude, the coherence length of the atmosphere r_0, the static aberrations of the telescope and the temporal bandwidth of the system, which is mainly defined by the loop gain. The estimated PSF is only valid within the isoplanatic angle from the reference source for the case of a single guide star.

3.2. The timeline of PSF Reconstruction

3.2.1. 1997: First PSF-R experience on PUEO at CFHT

In 1997, Veran published the article *Estimation of the adaptive optics long exposure point spread function using control loop data* (Véran et al., 1997). This the first and most successful implementation of the AO PSF reconstruction algorithm, and it has been the basis for development of new PSF-R in AO up to present times. In this case, the estimation of long exposure PSF from AO telemetry data is based on the analysis of the atmospheric turbulence properties using Kolmogorov statistics and characterization of the AO components. Section 2.7 discussed the complete theory and mathematical development on the reconstruction algorithm. Equation 2.127 states that the long exposure OTF can be expressed as the product of three different contributions: the static contribution (due to the non-common path aberrations), the residuals from the AO loop and the contribution from the high order components of the turbulent phase excluded from the AO correction.

The PSF reconstruction was successfully tested and implemented during the first commissioning runs of PUEO. PUEO is a curvature based AO system operated at the Canada-France-Hawaii Telescope(CFHT). PUEO contains a bimorph DM with 19 actuators and a WFS with 19 sup-apertures.

The results obtained during these runs were based on the observation of a point source (star) so that its image could be considered a good approximation to the real PSF and could be directly compared to the estimated PSF. Images were obtained at $1.65\mu m$ and $2.12\mu m$. The method accuracy depends on the guide star magnitude, i.e. for stars of magnitude 13 or brighter, the long exposure PSF is well estimated (see figure 3.1) and is potentially useful for image restoration. The estimated PSF characteristics are: FWHM within 0.01 arc-seconds, Strehl ratio (SR) within $\pm 4\%$ accuracy, accurate morphology, precision on OTF ranging from 10^{-2} for low spatial frequencies to 10^{-1} at high spatial frequencies. The estimation errors are originated at the high end of spatial frequencies.

For stars fainter than magnitude 13, the accuracy of the PSF estimation is degraded and deviates significantly from the theoretical PSF. This is because the measurement error is increased due to the decreasing number of photons, and then the loop gain has to be lowered reducing the bandwidth; thus $f_{cl} > f_{\mathcal{M}}$ is no longer valid. Consequently, D/r_0 is underestimated giving an estimated PSF with higher SR than the real value.

The estimated PSF is only valid within the isoplanatic angle from the reference source, and for greater angular distances the system performance is degraded by the anisoplanatic errors which were not included in this study but should mean a modification to equation 2.127.

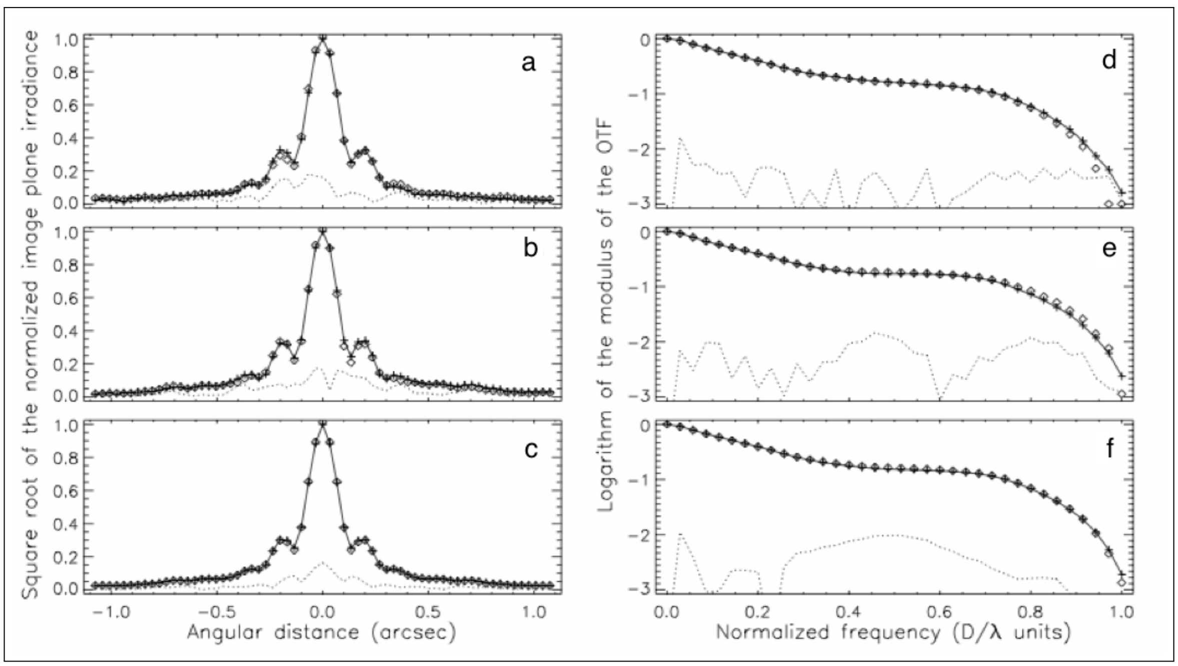

FIGURE 3.1. PSF reconstruction results on PUEO for a guide star with magnitude 10.4. Left plots: square-root of the normalized image plane irradiance. Right: modulus of the OTF in logarithm scale. Plots are for X-cut(a and d), Y-cut (c and e) and circular average(c and f). The real PSF is plotted in solid line and '+' markers. Diamonds represent the estimated PSF. The dotted line is the absolute difference of the two curves in the same escale.

3.2.2. 1999: PSF-R applied on ADONIS at ESO 3.6m telescope

The article *Estimating the point spread function of the adaptive optics system ADONIS using the wavefront sensor measurements* was authored by Harder and Chelli (2000) and is the first attempt to implement PSF-R on a Shack-Hartmann system.

ADONIS was the AO system for *La Silla 3.6-m* telescope, and is currently decommissioned. ADONIS was based on a Shack-Hartmann sensor with 7 x 7 sub-apertures. It had two mirrors for wave front correction: a tip/tilt mirror and a piezo-stack deformable mirror with 52 actuators. ADONIS used modal control and due to invisible and redundant modes only fifty modes were corrected.

The PSF estimation for ADONIS was based on Veran's algorithm, but it was necessary to define a method for estimating the measurement noise of a Shack-Hartmann WFS. The noise for a Shack-Hartmann device is generally a superposition of photon noise and read-out noise. In practice, the autocorrelation method is used, which consists in deriving the noise from the bias on the central point of the autocorrelation function by fitting an arbitrary function (e.g. a parabola) near its origin.

From experimental data, the measurement noise estimation was obtained by the analysis of the autocorrelation of measured wavefront slopes. As reported in the article, this method has an accuracy of 7 to 8%. Analysis of the measurement noise in open loop was straightforward, but for closed loop operation, this was harder to estimate as the consecutive slope measurements are less correlated due to the wavefront correction, making difficult to extrapolate the autocorrelation function to its origin. Measurement noise estimations in good atmospheric seeing conditions were consistent for both open and closed loop; however, in bad atmospheric seeing conditions the measurement noise estimated in open loop is higher than in closed loop.

The PSF reconstruction algorithm was evaluated under three different conditions:

- Bright reference sources(7.4 to 7.7 magnitude) and good seeing (0.9 to 1 arcsec): The maximum reconstruction error on the OTF was about 10 to 20% at low frequencies. The observed PSF is not symmetric, and the asymmetry changes in position on a short time scale. The estimated PSF can not reproduce the asymmetry, and the maximum error is located in the first null of the diffraction pattern.

- Faint reference sources (10 to 12 magnitude) and very bad seeing (1.5 to 2 arcsec): The reconstructed OTF is underestimated by at least 20 to 30% at low frequencies. The non-common path aberrations were calibrated, but using either the ideal or the measured instrumental OTF did not change the quality of the PSF reconstruction.
- Faint sources(10 to 12 magnitude) and very good seeing(0.6 to 0.7 arcsec): The residual aberration visible on the first diffraction ring was stable; thus it was possible to calibrate the static non-common path aberrations. The error on the reconstructed OTF was less than 10% at low and medium frequencies. The asymmetry of the PSF is quite well reproduced within a mean error between 5 and 10%. It was observed for cases with larger error in the reconstruction that the average measured flux per sub-aperture on the WFS was about 4.5 photoelectrons, and there were instants where the measured flux is lower than 2 photoelectrons. In these cases, the center of gravity in the WFS was poorly estimated.

It was concluded that PSF estimation under bad seeing is not satisfactory, with a permanent under-estimation of the OTF by 20 to 30% at low and medium spatial frequencies. On good seeing conditions, the OTF is estimated with 10% accuracy and it was found that this was due to the non-modeled aberration visible in the first diffraction ring. The aberration was non-stationary and was not due to the non-common path aberrations.

The presence of a slowly evolving and non fully developed turbulence was observed. This turbulence was probably caused by temperature gradients above the primary mirror and could be the cause of the residual aberration.

The residual aberration, limited the photometric precision, when is variable causes an important error on the flux ratio of a binary system. The error is of the order of 10 to 40% at the location of the first diffraction ring and 5 to15% for larger distances. When it is stable, the error is much smaller, of the order of 3 to 10%.

There are not other publications about ADONIS that could account about the source of the local turbulence. However, it can be seen how the PSF-R implementation helps to make a rigorous characterization of the telescope and the AO system providing unexpected findings of anomalies in the system.

3.2.3. 2001: Preliminary studies for the application of the PSF-R to a MCAO system

Véran (2001) starts outlining the implications and limitations of the PSF-R algorithm applied to the MCAO system envisioned for Gemini South Observatory.

The aforementioned MCAO system comprises 5 Laser Guide Stars (LGS) and 3 Deformable Mirrors (DM). As in any AO system, the correction provided by a MCAO system is not perfect.

A MCAO system can not achieve an optimal correction everywhere in the field of view: since there is a finite (small) number of guide stars, the tomography can not be complete. In addition, in MCAO the residual phase cannot be fully reconstructed in 3 dimensions, but rather only at 3 discrete altitudes (the DMs).

Véran stated a limitation to the PSF estimation scheme: the field dependence of the MCAO PSF could not be fully retrieved by the estimation scheme based on the MCAO loop data. However, the field dependent error in the PSF estimation is very small; especially considering that the field dependence of the MCAO PSF is quite weak by definition.

A second limitation of using loop data to reconstruct the PSF: the residual speckle noise cannot be reconstructed and has to be computed as a function of D/r_0 using the Kolmogorov model.

To estimate the structure function of the mirror component of the residual phase, ($D_{\phi_{\varepsilon\parallel}}$), the same approach presented in section 2.7.1 can be used. Recalling equation 2.124:

$$D_{\phi_{\mathcal{E}\|}}(\Delta r) = \sum_{i,j}^{N} \left\langle \mathcal{E}_i \mathcal{E}_j \right\rangle U_{ij}(\Delta r) \tag{3.1}$$

The problem is then to determine the covariance matrix $\left\langle \mathcal{E}_i \mathcal{E}_j \right\rangle$ from the WFS measurement. It is necessary to take into account that tip, tilt and tilt anisoplanatism modes are not given by the LGS but rather by the natural guide stars (NGS). Flicker and Rigaut (2001) introduced a new approach to estimating the covariance of the tilt anisoplanatism modes in the residual phase of an MCAO system was presented.

While the implementation of PSF reconstruction based on AO loop data on any other curvature based AO system would be straightforward, the generalization of this scheme to a Shack-Hartmann based system remains problematic, even in the case of a classical AO system, as was experienced with ADONIS. The main issue has to do with the estimation of the noise in the SH WFS. With a MCAO system, the LGS WFS will have a fairly constant and relatively high signal-to-noise ratio, which should facilitate the noise estimation.

LGS WFS are based on quad-cells, and their measurement is related to the actual wavefront by a gain factor (centroid gain). An accurate knowledge of the gain is critical for PSF reconstruction.

It must be emphasized that uncalibrated static aberrations may affect the quality of the estimated PSF; thus everything that is not seen by the WFS must be calibrated and entered into the PSF reconstruction method.

3.2.4. 2002: PSF-R algorithn for LGS MCAO systems.

Flicker, Rigaut, and Ellerbroek (2003) presented a method for estimating the long exposure PSF degradation due to tilt anisoplanatism in a LGS based MCAO system from control loop data.

In LGS MCAO systems, the global tip and tilt can not be inferred from the LGS measurement, and the tomographic wavefront reconstruction in MCAO will be impaired and unable to determine the altitudes of a subset of low-order modes. As a consequence of the tilt filtering, the MCAO system looses all tomographic information about the altitudes of quadratic modes. Lacking any information on the altitude of the mode, the system concludes that it was all located at the ground and consequently will assign all correction to the pupil-conjugated DM. As a result, the mode will be perfectly corrected on-axis, but off-axis only the quadratic parts will cancel and leave a field-dependent tilt component uncorrected. Failure to correct this differential tilt will result in differential image motion, or tilt anisoplanatism, which will manifest in an MCAO image as a convolution of the long exposure PSF with a field-varying Gaussian. Hence, the atmospheric tilt error is described by a Gaussian PSF whose width and orientation are field-dependent.

The estimation algorithm uses the closed loop WFS measurement covariance matrix and the WFS noise covariance matrix to obtain the tilt covariance matrix. With the tilt covariance matrix, the pupil-averaged phase structure function is calculated which is used to estimate the atmospheric long exposure OTF.

The algorithm was implemented at simulation level and was reported as a robust reconstruction algorithm. It had a high accuracy over the entire field of view, with 5% of error at the H band and a limiting asterism magnitude M_R = 19. Together with an algorithm for estimating the PSF variation due to partial correction of the high-order LGS system, a complete specification of the LGS MCAO PSF can be achieved, such as is indispensable for subsequent accurate photometry and deconvolution.

3.2.5. 2003: PSF-R for ALFA AO system

Weiss (2003), addresses the problem of implementing the PSF reconstruction method on ALFA, covering the on-axis and off-axis cases.

ALFA is an AO system, operated by the Max-Planck-Institut für Astronomie at the Calar Alto Observatory in Spain. ALFA is Shack-Hartmann based system. It has a tip/tilt mirror and a deformable mirror with 97 actuators.

Veran's algorithm was implemented for the estimation of the on-axis PSF. For the estimation of the off-axis PSF, measurements from the atmosphere turbulence profiler SCIDAR were used to characterize the atmosphere statistics.

In ALFA, it is not possible to obtain the slope measurements directly because of hardware and processing capability restrictions; therefore, it is only possible to make an indirect estimation of the noise by time-series analysis of the WFS signals. Weiss proposed a new method for noise estimation, which provided better results for faint guide stars and low loop frequencies. The method is done using the auto-covariance of the WFS measurement, with noise estimation errors in the order of 1%.

For the PSF reconstruction, a good agreement between observed and estimated PSF, was found. OTF errors were below 10% for the on-axis case and below 25% for the off-axis case. However, the most prominent deviations come from uncalibrated non-common path aberrations and low signal-to-noise ratio at the wings of the measured PSF. For faint stars, the reconstruction was not possible unless the new noise estimation method was used.

Accuracy of photometry was improved by use of the estimated PSF. For the bright star case, the magnitude estimation error was reduced to under 5%, but for faint stars the results were not conclusive.

3.2.6. 2004: PSF reconstruction at Lick Observatory

Fitzgerald (2004) briefly reported the status of the PSF reconstruction implementation at Lick Observatory.

The Lick's AO system is a LGS Shack-Hartmann system with 40 sub-apertures in a square layout, and a DM with 61 actuators in triangular layout. The AO system has maximum sampling frequency of 1 Khz, but typically operates at 500 Hz. The control loop uses a weighted-least squares control matrix. For imaging, it is equipped with a CCD for detection at 2.2 μm.

The PSF reconstruction follows Véran's approach and tries to develop the Shack-Hartmann WFS noise covariance using the difference between the covariance of the noise measurements and the covariance of the noiseless measurements (obtained from an empirical model for noise variance vs. mean in each pixel).

Finally, the resulting PSF estimation has a considerable error. The error sources were calibration problems for the components of the system.

3.2.7. 2004: Software for automatic PSF-R applied to Altair

Jolissaint, Véran, and J.Marino (2004) worked on automatic PSF reconstruction, which resulted in the creation of an IDL-based software called OPERA(Performance of Adaptive Optics). Using OPERA, PSF-R was implemented for a Shack-Hartmann (4-quadrant type) based AO system in Altair, the Gemini-North AO system.

In addition, improved methods in the determination of r_0 from the DM drive commands were presented, which includes an estimation of the outer scale L0; and the contribution of the high spatial frequency component of the turbulent phase, which is not corrected by the AO system and is scaled by r_0.

It is generally accepted that PSF-R has been succesfully solved for curvature AO systems. To adapt this method to another type of WFS, a specific analytical noise propagation model must be established. Specifically, for Shack-Hartmann WFS it was proved that is possible to derive an accurate estimation of the noise on each sub-aperture, based on the covariances of the WFS CCD pixel values in the corresponding sub-aperture.

This Jolissaint et al. work demonstrates that the residual AO corrected tip-tilt variances can be directly extracted from the statistics of the noisy 4-quadrant outputs, without using any assumptions on the noise level. In fact, this method can be applied either to open or closed loop,for any noise level.

Unfortunately, no on-sky data was acquired in this case, and tests were done with an artificial star through a phase screen turbulator. Although testing conditions were not good for characterizing the accuracy of the PSF estimation, it was possible to validate the PSF reconstruction algorithm using OPERA, and the progress done for noise estimation of Shak-Hartmann WFS was remarkable for the development of the technique.

3.2.8. 2006: New algorithms for AO PSF-R

The PSF reconstruction algorithm developed by Véran makes use of the U_{ij} functions that are derived from the mirror modes. The total number of the U_{ij} functions is proportional to the square number of these mirror modes, whichrequires handling large amounts of data in systems with 150 to 200 actuators, limiting the efficiency of the PSF reconstruction process. Gendron et al. (2006) presented two new algorithms for suppressing the use of the U_{ij} functions, in order to avoid the storage of large amounts of data and to shorten the computation time of the PSF reconstruction. Both algorithms take advantage of the eigen decomposition of the residual parallel phase covariance matrix, $\mathcal{C}_{\mathcal{E}\mathcal{E}}$.

In the first algorithm, the use of a basis in which the residual parallel phase covariance matrix is diagonal reduces the number of U_{ij} functions to the number of mirror modes. Recalling 2.124, the long-exposure OTF and long-exposure PSF can be estimated from the structure function of the mirror component of the residual phase, that is:

$$D_{\phi_{\mathcal{E}\|}}(\Delta r) = \sum_{i,j}^{N} \left\langle \mathcal{E}_i \mathcal{E}_j \right\rangle U_{ij}(\Delta r) \tag{3.2}$$

In equation 3.2, the i and j indices play a symmetric role so that there are $N(N+1)/2$ useful $U_{ij}(\Delta r)$ functions. Depending on the array size and data type, the large number of $U_{ij}(\Delta r)$ implies several gigabytes of data to compute, store, and read. For the next generation of AO systems, even if equation 3.2 can be efficiently implemented, the PSF reconstruction process may be impossible to handle since these are expected to have much larger number of modes, i.e. in the order of several tens of thousands for extremely large telescopes.

In this article, Gendron et al. introduce the V_{ii} algorithm. This new algorithm proposes to diagonalize the residual parallel phase covariance matrix, $\left\langle \mathcal{E}_i \mathcal{E}_j \right\rangle$, using eigen decomposition. Having $\{\lambda_i\}_{i=1\ldots N}$ as the set of eigenvalues of $\left\langle \mathcal{E}_i \mathcal{E}_j \right\rangle$, and B the matrix of eigenvectors, then

$$D_{\phi_{\mathcal{E}\parallel}}(\Delta r) = \sum_{i=1}^{N} \lambda_i V_{ii}(\Delta r) \tag{3.3}$$

In the new basis the $V_{ij}(\Delta r)$ functions are the equivalent to the $U_{ij}(\Delta r)$ functions.

$$V_{ij}(\Delta r) = \frac{\int\int_A A(r)A(r+\Delta r)[M'_i(r) - M'_i(r+\Delta r)][M'_j(r) - M'_j(r+\Delta r)]dr}{\int\int_A A(r)A(r+\Delta r)dr} \tag{3.4}$$

Matrix M' obtained from the eigenvector modes, $\{M'_i\}_{i=1...N}$ is given by $M' = B^t$, M being the matrix made of the mirror modes $\{M_i(x)\}_{i=1...N}$. The V_{ii} functions have to be computed on the fly for each estimation of the mean residual parallel phase structure function.

In the second algorithm, the eigen decomposition is used to compute phase screens, $\phi(x,t)$, that follow the same statistics as $\langle \mathcal{E}_i \mathcal{E}_j \rangle$. From the phase screen, the instantaneous PSF is calculated as $PSF_{\parallel}(x,t) = |\mathcal{F}(exp(i\phi(x,t)))|^2$. On average, the set of instantaneous PSFs will converge to the long-exposure PSF of the mirror space. It is necessary to note that this algorithm does not include the uncorrected part of the phase $\phi_{\perp}(x,t)$.

Simulation results showed that U_{ij} and V_{ii} produce the same OTFs. In practice, the U_{ij} algorithm requires reading each of the $N(N+1)/2\, U_{ij}$ functions (where N is the number of modes), which have been computed and stored previously. In comparison, the V_{ii} algorithm requires to diagonalize the covariance matrix, to compute the new modes $\{M'_i(x)\}_{i=1...N}$, and each V_{ii} function.

The approach of V_{ii} functions will be evaluated on the PSF reconstruction implementation for NICI.

3.2.9. 2006: PSF reconstruction for NAOS-CONICA

Clénet et al. (2006) implemented the PSF reconstruction in NAOS, the SH AO system of NACO at Paranal'sVLT. NaCO provides adaptive optics assisted imaging, imaging polarimetry, coronography, sparse aperture masking and spectroscopy. NAOS is the AO system of NACO and CONICA are the infrared camera and spectrometer attached to NAOS [from www.eso.org].

A dedicated algorithm for NAOS was developed based on Veran's original idea. However, this attempt was focused on implementing the PSF reconstruction applying the V_{ii} *algorithm* and *the instantaneous PSF algorithm*, described in the previous paragraph.

Simulations with a model of NAOS and the PSF reconstruction algorithm, showed that the long exposure OTF was over-estimated, especially for faint stars. The cause of the problem was found on the noise model for the Shak-Hartmann WFS.

The relationship between s_m and s_0 is defined as:

$$s_m = Gs_0 + n \tag{3.5}$$

where G is a coefficient and n an additive noise, uncorrelated with s_0.

For the Shack-Hartmann WFS in NAOS, the centroid of each subaperture spot is computed from the pixels that have an intensity greater than a given threshold. From the centroid position, the wavefront slope is calculated.

It was found that the coefficient G has a direct dependence on the value of the threshold. Running simulations that include the relationship between G and threshold resulted in the expected OTF. As a conclusion, the threshold level is a key issue when reconstructing PSFs from real SH data. An improper threshold level may bias the data, leading to a wrong estimation of noise and the phase residuals.

The delivery of wavefront-related data to estimate the PSF has been an important specification for NAOS to maximize the scientific returns of the instrument. From the CONICA images, the observer gets the two residual modal covariance and mirror modal covariance matrices and the corresponding two means; turbulence parameters, such as r_0, L_0, and AO loop parameters such as the Zernike mean noise $\bar{n_z^2}$.

As previously discussed, the assumptions made to compute the noise part of the OTF are important. Having only $\bar{n_z^2}$ for this purpose, might result in large uncertainties for the PSF estimation. To improve this situation it was proposed to modify the Real Time Computer software, so it provides the vector of variance noises $n_{z_i}^2$ for all considered Zernikes, or provide the vector of variance noises n_i^2 for all considered mirror modes.

For the computation of the orthogonal or uncorrected OTF, a possible alternative is to use the *instantaneous PSF algorithm* with an orthogonal phase screen, $\phi_\perp$ and evaluate the instantaneous PSF as $|\mathcal{F}(exp(i\phi_{\mathcal{E}\perp}))|^2$, averages them to get $PSF_\perp$ and, after a Fourier transform, the perpendicular OTF multiplied by the telescope OTF; Alternatively, the U_{ij} could be used.

Although the reported work is only at simulation level, the contribution to more accurate AO simulations is important for effective implementation of PSF reconstruction. In particular, it helped to improve the noise model of Shack-Hartmann WFS.

3.2.10. 2006: Point spread function reconstruction for Woofer-Tweeter adaptive optics bench

Keskin, Conan, and Bradley (2006) attempt for the implementation of PSF reconstruction over a woofer-tweeter AO bench for the first time.

In this architecture, the woofer is a low-order-high-stroke DM, and is used to compensate for the low-frequency-high-amplitude effects introduced by the atmospheric turbulence. The tweeter is a high-order-low-stroke DM that is used to compensate for the high-frequency-low-amplitude effects introduced by the atmospheric turbulence.

For Extremely Large Telescopes (ELT), due to the unavailability of a DM manufacturing technology, it will not be possible to provide an AO correction with a use of a single high-order-highstroke DM (containing large number of actuators) as is done in current AO systems on 4-10 meter class telescopes. A solution to this problem for the ELTs is the use of this dual configuration DMs, that provide high degrees of correction for large wavefront amplitude distortions.

The importance of the AO bench is to demonstrate the closed-loop wavefront control feasibility for a W/T AO concept to be used on the science instruments of the Thirty Meter Telescope (TMT).

The PSF reconstruction followes Veran's method adapted to Shack-Hartmann systems. The PSF reconstruction was validated using numerical simulations and experimental data.

The results showed a good match between measured and estimated PSF. No additional analysis was provided in order to understand the quality of the reconstruction process.

3.2.11. 2007: PSF-R at Dunn Solar Telescope

Marino (2007) implemented a PSF reconstruction version in the Dunn Solar Telescope, being the first implementation in solar astronomy.

The Dunn Solar Telescope in Sunspot (New Mexico, USA) has a Shack-Hartmann based AO system with a 76 apertures wavefront sensor (WFS) and a continuous face plate deformable mirror with 97 actuators .

Many basic processes in the sun take place in small scales (< 1"). Its atmosphere is highly dynamic, and most solar phenomena are a direct result of the active magnetic field continuously emerging from the solar interior on scales from granulation to active regions. The sun's magnetic field produces coronal mass ejections, flares, and solar winds.

Solar physics require high-resolution observations that produce accurate measurements. AO correction and post-processing, with an estimation of the AO-corrected PSF, are vital to produce accurate scientific measurements. In night-time observations, the PSF can be measured directly from the image of a star. However, a direct measurement of the PSF from solar observations is impossible due to the lack of point sources in the field-of-view.

The PSF reconstruction was implemented following Veran's method adapted for Shack-Hartmann WFS. In this case, the noise covariance matrix estimation of the WFS was done using statistics of the measurements. Being the sun a very bright source, the noise in the system is not relevant for the PSF estimation.

The PSF reconstruction implementation was tested using Sirius as a point-object source. It should be noticed that Sirius is not as bright as the sun, so even though the system was able to lock over Sirius, the Strehl ratio was too low. In addition, the seeing conditions were too poor, causing strong differences between the PSF estimation and the PSF measurement.

Later, the PSF reconstruction was tested on a AO driven solar observation. It was verified that quantitative measurements and scientific data were significantly improved by deconvolution with the estimated AO PSF (see figure 3.2).

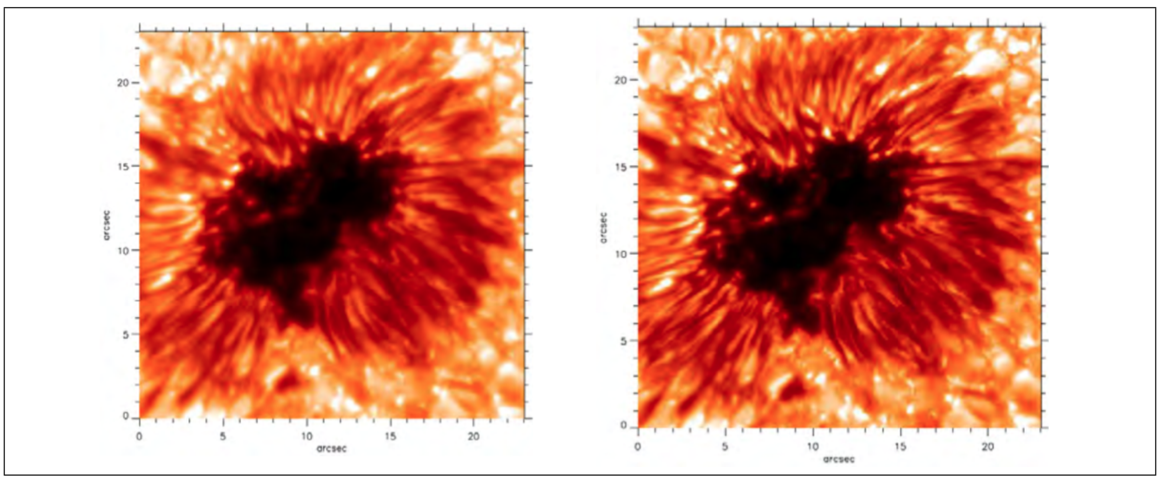

FIGURE 3.2. Sun spot image made with AO correction and improved with estimated PSF deconvolution. Left: AO-corrected sun spot image with $r_0 \approx 18$ cm. Right: Deconvolved AO-corrected sun spot image. Credit: Marino

3.2.12. 2008: Tests of the PSF reconstruction algorithm for NaCo/VLT

In Clénet et al. (2008), the work started in 2006 for the PSF reconstruction on NAOS-CONICA is resumed (see section 3.2.9).

After indications made during the 2006 campaing, the software of the Real Time Computer was modified to provide the vector of variance noise $n_{z_i}^2$ for all considered Zernikes, so the resulting scientific images are provided with the covariance matrices that allow to compute the WFS measurement covariance matrix and the measurement noise covariance matrix. In addition, the estimation for r_0 from the DM commands is also provided. The orthogonal phase covariance matrix is estimated via simulations as already described in section 3.2.9,

Two tests were executed: i) checking the orientation of the reconstructed PSF with respect to the CONICA images using the NAOS calibration source; and ii) on-sky observations aimed to evaluate the quality of the PSF estimation.

For the first test, it was found that the reconstructed PSFs are in good agreement with the CONICA images in terms of orientation. The expected and observed images match well, and there is no rotation or symmetry that could give the same matching.

The results for the on-sky testing, were not promising. In the first on-sky test, with a bright source (V=9) and good atmospheric conditions, the PSF estimation showed significative differences in comparison to the observed PSF. The Strehl ratio of the former is $\approx 39\%$ whereas the one of the latter is $\approx 31\%$. The discrepancies between the reconstructed and observed PSFs could be due to the presence of a faint companion close to the target, the lack of the aliasing contribution or/and the use of a fibre image instead of a bright star to calibrate the non common path aberrations; the latter being more accurate compared to the former.

For the second on-sky test, a fainter star (V=12.7) was used, and non-common path aberrations were calibrated using a star. The estimated PSF had a Strehl ratio $\approx 19\%$, whereas the observed PSF Strehl ratio was $\approx 32\%$. The reconstruction was worse than for the first test. This discrepancy could be explained by an error in the estimation of the aliasing contribution or/and a bad estimation of the noise contribution using the Zernike mean noise value. Note also that the chosen star might have been too faint to provide a good reconstruction with such algorithm.

Further development of the PSF reconstruction was done using SESAME, an optical bench developed at LESIA/Observatoire de Paris. The first tests showed inaccuracy in the PSF estimation; however, the loss of accuracy is low when estimating the noise from the

Zernike noise variance vector. The most probable origin of the discrepancies is the short loop bandwidth used for this test.

3.2.13. 2008: Exploring the impact of PSF reconstruction error on the reduction of astronomical AO based data

Research conducted by Jolissaint, Carfantan, and Anterrieu (2008) tried to answer the question of what is the required accuracy on the quality of the PSF reconstruction, with a focus on Wide-Field Adaptive Optics (WFAO) systems, and tries to set the guidelines needed in order to check the validity/usefulness of a given PSF reconstruction approach. The goal of this study is to show the impact of PSF estimation errors on data reduction; thus it does not cover PSF reconstruction techniques. The method builts a set of AO corrected PSFs, for a variety of AO parameters, and simulate data reduction using PSF with an increased difference with respect to the initial PSF parameters.

WFAO systems as Ground Layer AO(GLAO), Laser Tomography AO (LTAO), Multi-Conjugate AO (MCAO), and Multi-Object AO (MOAO) are coming on-line or will be on-line very soon, and it is expected that the demand for AO-based observation will increase very significantly. The difficulty with AO data is the complexity of AO PSF structure. Moreover, it varies across the field-of-view, and the quality of the correction depends on the seeing, which can change quickly. As a consequence, simple PSF models in the astronomy for seeing limited data reduction (Gaussians, Moffat) will not be sophisticated enough to represent the full variety of the PSF structure. Over the last years a few AO research groups have started to develop PSF reconstruction techniques, most of them based on AO loop data, extending to WFAO using a method pioneered by Véran et al. (1997) - see for reference (Keskin et al., 2006) and (Clénet et al., 2008).

Amongst the different data reduction schemes, the most sensitive to the PSF structure are the deconvolution approaches, either seen as an inverse filtering process, or a source extraction process. Other methods were not considered in this study.

The parameters with the strongest impact on the PSF structure can be separated in static and dynamic. Critical static parameters are non-common path residual aberrations and telescope static errors; these sources of PSF uncertainties are not discussed here. Critical dynamic parameters are the Fried parameter r_0, the vertical distribution profile C_N^2 and the residual tip-tilt in LGS AO systems.

For most of the classical image deconvolution techniques, the main impact of a PSF reconstruction error can be studied using the concept of residual filter, which is the ratio of the exact OTF over the reconstructed OTF.

As a preliminary result, it was found that impact of PSF reconstruction errors over deconvolution were noticeable but surprisingly low. This situation apparently relaxes the need of highly sophisticated PSF-R algorithms.

The data reduction simulations found that for Wiener-like deconvolution algorithms, tip-tilt uncertainty is the most critical parameter. For CLEAN-like algorithms, seeing angle estimation error is the dominant factor.

More extended analysis of the impact of the PSF errors must be done before drawing a final conclusion. It is recommended to model the nominal PSF with an end-to-end Monte-Carlo method.

3.2.14. 2010: PSF-R in GLAO system ARGOS

AO systems aiming to provide large field of view combined with large sky coverage use multiple laser beacons on sky. In practice, AO assisted astronomical observations produce images in which the PSF varies with the field position. Therefore, knowing the off-axis PSF becomes as important as the on-axis PSF.

PSF-R techniques seem to be far from being a standard tool in the reduction of AO-based astronomical data. In the context of the ARGOS project Peter and Gässler (2010), investigated the PSF reconstruction problem for AO systems using multiple laser guide stars to provide the observer with a trustworthy PSF map directly in combination with the raw science data.

The ARGOS system is a Ground Layer AO (GLAO) system proposed for the Large Binocular Telescope (LBT). It uses three Rayleigh laser beacons per eye equally placed in a 2' radius circle at a height of 12 km. The high order part of the wavefront is measured on these beacons by one 15x15 Shack-Hartmann WFS per beacon. The Tip-Tilt(TT) values are obtained from one natural TT-star using a pyramid WFS. The system will run at 1 Khz frame rate.

There are two algorithms proposed for the off-axis PSF estimation. The first introduces the Anisoplanatic Transfer Function (ATF). According to Britton (2006) the OTF can be formulated for any direction in the sky as the product of the guide star OTF and the ATF formed from $D_{apl}(r)$, where $D_{apl}(r)$ is the structure function of the residual phase arising from anisoplanatism, or the anisoplanatic structure function. The anisoplanatic transfer function is given by $ATF(r) = exp[-\frac{1}{2}D_{apl}(r)]$.

The alternative approach derives the off-axis PSF by first projecting the WFS signal into the desired off-axis direction via correlations between the wavefron on-axis and off-axis for a subsequent use of the standar on-axis algorithm. This last approach seems to be more favorable to laser based systems as it is straightforward to include the cone effect.

In comparison to the classical PSF reconstruction scheme, the reconstruction for AO systems using multiple sources face more difficulties: First, the low order and high order spatial information have different sources. Second, in the case of laser systems , high layer turbulence is poorly sampled.

To overcome these difficulties, the inclusion of the the following features in the reconstruction scheme are proposed:

- Project the wavefronts from the different sources rather than the OTF.
- Derive the lower altitude atmospheric profile from different WFS using SLODAR.
- Use DIMM-MASS data to estimate the total atmospheric profile.
- Use potential truth sensor information to refine the contribution of the upper atmosphere.

A first simulation of the proposed scheme was done. The on-axis PSF was reconstructed using a 1' off-axis TT-star and another star for high order correction at (-1)' off-axis. With an original system resolution of 0".2 the PSF reconstruction enabled to resolve a 0".1 binary.

3.2.15. 2011: The PSF reconstruction effort for NICI, the high-contrast coronographic imager on Gemini observatory

Since the first successful implementation of PSF-R in a curvature system (Véran et al., 1997), many other initiatives tried to implement PSF retrieval in AO supported instrumentation. No observatory has reached a comparable level of AO telemetry data handling as is standard for the direct scientific data. Since AO is key for ELTs, this should change in a not too far future.

In 2009, Damien Gratadour developed the code base of APETy (A PSF Estimation Tool for Yorick, http://github.com/dgratadour/apety).

In this work, (Hartung et al., 2011) evaluates the APETy performance when implemented for the PSF-R in NICI, an AO system installed at Gemini South. NICI consists of a curvature WFS with 85 sub-apertures and a bimorph DM with 85 actuators.

Most of the work that could be done so far focused on optimizing and comparing simulated PSFs (for a NICI alike curvature system) with the APETy output. The end-to-end simulations were done using YAO, a full- fledged Monte Carlo Simulator for single and multi-conjugated Adaptive Optics written by F. Rigaut (http://frigaut.github.com/yao/).

An accurate estimation of the parallel part of the wavefront (roughly spoken the part that can be controlled by the AO system) based on the WFS telemetry is key to the basic performance of APETy.

The parallel phase structure functions are better estimated when the phase split (parallel and orthogonal components) is based on the WFS geometry. Instead of projecting the simulated phase directly onto the DM modes, the phase is sampled by the WFS first and then projected on the DM modes (and/or influence functions).

For a numerical implementation and comparison using Monte Carlo simulators, this is an important aspect to consider. For a correct comparison, the parallel phase needs to be constructed passing by the WFS (WFS based split). Clearly, this point is also relevant to compute a representative orthogonal phase (to be scaled by a measured r_0) that APETy or other retrieval codes would use to assemble an appropriate long exposure PSF.

Long exposure PSFs were retrieved using APETy and compared with a YAO simulated PSF. The PSF retrieved from the split based on the WFS compares better with the expected PSF than the PSF retrieved from split based on the DM. For both cases, the inner part of the PSF appears to be consistently overestimated while the outer part (a few λ/D) is underestimated.

This work is the motivation and the base for this thesis as well as the study case to be presented in the next chapter.

3.2.16. 2011:First successful AO PSF reconstruction at W.M. Keck Observatory

Jolissaint et al. (2011) reported the last results of the PSF-R project for the Keck-II and Gemini- North AO systems using natural guide stars.

The most critical aspects of PSF-R are the determination of the systems static aberrations and the optical turbulence parameters (seeing diameter r_0, outer scale L_0) as seen from the telescope. The PSF structure is very sensitive to these parameters, and the difficulty to accurately determine these parameters prevented the successful reconstruction of the PSF on these systems.

For the seeing estimation, the approach proposed by Véran et al. (1997) was used: extracting the average Fried parameter r_0 and the optical turbulence outer scale L_0 from the DM commands statistics. The closed loop DM-based seeing monitor technique works well: 10% accuracy is easily obtained for estimating both the seeing value r_0 and the outer scale L_0. Therefore, there is no need to implement independent seeing monitors at telescopes equipped with AO systems: the DM telemetry can be used for this.

The static aberrations determination was made using of a phase diversity (PD) approach adapted to the use of AO corrected sky source images. In the PD approach, it is assumed that the difference between the diffraction limited PSF and a defocused PSF is only generated by the defocus and that the imaged object remains the same.

Phase diversity has been demonstrated to work on sky sources, but is crucial to have a reliable estimate of the seeing associated with the PSF, and keep only the PSF with similar seeing angle.

The corrected phase homogeneity across the pupil was evaluated. The residual phase is essentially stationary everywhere (83% of the pupil surface), except on a few actuators on the edge. Therefore, the stationary assumption is valid, and it is possible to proceed with the separation of the global OTF into the telescope OTF and the AO-OTF. It is concluded that the higher the actuators density, the better the stationary assumption. Hence, reconstructing the PSF for AO systems with a high actuators density (ExAO systems, AO on extremely large telescopes) can also make use of the OTF separation paradigm.

The PSF reconstruction results for the Keck-II system, in NGS mode, have a Strehl error in the order of 5% and the FWHM error is negligible. The detailed PSF structure shows some differences, and this is certainly due to the uncertainties in the determination of the static aberrations.

3.2.17. 2012:PSF Reconstruction Project at W.M. Keck Observatory : First Results with Faint Natural Guide Stars

Jolissaint et al. (2012) report the progress in the PSF-R project for single guide star AO systems running at the W. M. Keck & Gemini-North observatories, since January 2010.

Demonstrating the PSF-R method on a bright NGS is a first and necessary step. Later, going to fainter NGS with the consequent decrease of the loop frequency will test the high bandwidth hypothesis, that tells that if the control loop bandwidth is high enough so $f_{cl}(g_i) > f_{\mathcal{M}}$, then the filtering action of the closed-loop transfer function is negligible (See section 2.7.4).

Keck-II AO system is zonal, so the modes are the DM influence functions. There are 349 actuators, making 61075 U_{ij} functions. This would require a huge amount of time to compute (about 1 month of CPU), and about 64 Gb of memory for 512-by-512 matrices.

The residual phase is stationary in the pupil. In fact, it is like the telescope pupil was simply capturing a part of a turbulent phase corrected before the telescope. Therefore, it is possible to extend the residual phase anywhere in the plane before the pupil, totally ignoring the pupil edges. Alternatively, it is possible to redefine a virtual pupil (larger than the actual pupil) with edges such that it maximizes the number of symmetric couples of influence functions. The DM modes in use define 349 influence functions, on the extended pupil support. With this method, the number of independent U_{ij} functions to store is reduced to 2655, or half this (1328) because $U_{i,j}(r) = U_{i,j}(r)$.

It is worth noting that thanks to this freedom of the pupil edges definition and the resulting symmetries, the square relationship between the number of actuators and the number of $U_{i,j}$ becomes probably closer to a linear relationship, so there are good reasons to believe that this method makes the usage of $U_{i,j}$ functions still practical even for AO systems of extremely large telescopes.

The first results for PSF-R at Keck-II were obtained for a bright NGS (mV=10.1) for two narrow filters, Br-γ (λ = 2169 nm, $\Delta\lambda$ = 33 nm) and Fe-II (λ =1646 nm, $\Delta\lambda$ = 25 nm). Strehl and FWHM between the reconstructed and the sky PSF were in excellent agreement (less than 6 % difference in Strehl, and almost no difference in FWHM).

When the NGS magnitude increases (fainter source), the WFS noise impact becomes gradually noticeable, and in order to reduce the noise, the loop frequency is decreased, at the cost of increasing the servo-lag error. Therefore, the loop frequency is tuned to minimize the total contribution of both noise and servo-lag errors.

The WFS noise variance estimation was done by looking at the tail of the measured signal power spectral distribution (PSD) from NGS with different magnitude. It was not possible to use more rigorous methods than the one used on the noise estimation due to time restrictions.

For the PSF reconstruction of fainter NGSs, the behavior of the reconstructed Strehl with respect to the sky Strehl, as a function of the NGS magnitude was analyzed. It was found that the relative contribution of the noise becomes more important for increasing magnitude, so getting an accurate noise model is critical for fainter NGSs. In addition, the reconstructed Strehl drops with the magnitude following the same trend than the sky Strehl. Thus, the whole PSF-R procedure seems to work well.

These preliminary results do not show any anomalous behavior of the reconstructed Strehl for the weaker stars, as it expected as a consequence of the high BW assumption being not valid anymore. It could be that the other terms are simply dominating any low BW effect here. More data near the faint end are required before drawing any conclusion.

3.2.18. 2012: Tip/Tilt PSF reconstruction for LGS MCAO

The multi conjugate adaptive optics (MCAO) system under design for the Thirty Meter Telescope (TMT) is required to provide 2% differential photometry over a 30" field of view (FoV) for a 10 min integration at a wavelength of 1 micron, and 50 microarcsec root-mean-square (RMS) time dependent differential astrometry over the same FoV for a 100 sec integration in H band.

In LGS MCAO, multiple low-order NGS-WFSs are required to sense and control a few low-order atmospheric null-modes unsensed by the multiple high-order LGS WFSs. These null-modes consist of global TT and tilt anisoplanatism (TA) modes producing absolute and differential magnification on the science focal plane.

Gilles et al. (2012) describes how the approach developed by Flicker in 2002 (see section 3.2.4) that consists of post-processing the measurement covariance matrix of multiple low-order NGS WFSs, is used to solve the problem of reconstructing the TT covariance matrix of these modes in the science direction of interest and, therefore, the TT contribution to the long exposure PSF, from the multi-NGS WFS measurement covariance matrix.

The reconstructed AO system OTF is expressed as

$$OTF^{sys} = K_{TT}^{sys} OTF_{TTR}^{sys} \tag{3.6}$$

where OTF_{TTR}^{sys} is the tip/tilt removed (TTR) OTF estimated from on-axis LGS WFS measurement covariance matrix, and K_{TT}^{sys} the tip/tilt (TT) blurring filter function, obtained by post-processing low-order multi-NGS WFS measurement covariance matrix and expressed in terms of the TT structure function

$$K_{TT}^{sys}(u) = e^{-D_{TT}^{sys}(\lambda u)/2}, \;\; D_{TT}^{sys}(\lambda u) = 16(\lambda/D)^2 u^T C_{TT}^{sys} u \tag{3.7}$$

C_{TT}^{sys} is the reconstructed modal TT system phase covariance matrix (2x2, in units of radians squared). Following the scheme developed by Flicker, the unbalanced reconstruction of C_{TT}^{sys} involves three steps: (i) noise removal from the global low-order multi-NGS measurement covariance matrix, (ii) tomographic null-modes reconstruction (typically N_{mNGS}=5 modes are reconstructed, consisting of TT and 3 quadratic modes defined for two layers), and (iii) reconstructed null-modes projection onto TT along the science direction of interest. These 3 operations can be expressed as follows:

$$C_{TT}^{u,sys} = H_{TT} R_{NGS}^{sys} (C_{gNGS}^{sys} - C_{gNGS\ nse}^{sys})(R_{NGS}^{sys})^T (H_{TT})^T \tag{3.8}$$

where R_{NGS}^{sys} denotes the $N_{mNGS} \times N_{gNGS}$ modal tomographic NGS phase reconstruction matrix (N_{gNGS}=12 for a system employing 2 TT Shack-Hartmann WFSs and 1 TT/focus/astigmatism (TTFA)), H_{TT} is a 2 $\times N_{mNGS}$ matrix that projects the reconstructed null-modes onto TT along the science direction of interest, C_{gNGS}^{sys} is the closed loop NGS WFS measurement matrix, and $C_{gNGS\ nse}^{sys}$ denotes the estimated measurement noise covariance matrix, computed from centroid weights and subaperture time averaged pixels intensities.

The implementation of the TT PSFR is at simulation level only. Preliminary results shows that i) the TT error is negative, meaning that the estimated SR is too high and ii) the

TT error is concentrated in the PSF core (in an area of size equal to roughly twice the PSF FWHM).

3.2.19. 2012: PSF reconstruction for MUSE in wide field mode

The Multi Unit Spectroscopic Explorer (MUSE) is a panoramic integral-field spectrograph operating in the visible wavelength range that if fed by GALACSI, a four LGS wide field GLAO system which will be installed at the VLT in 2013. Villecroze et al. (2012) developed the PSF estimation algorithm at any location of the FoV and for every wavelength of the MUSE spectrograph using telemetry data coming from both AO LGSs and NGSs The estimation algorithm computes the GLAO PSF for all the positions and all the wavelengths of observation from the computation of the residual phase structure function D_ϕ and an internal MUSE PSF. This estimated GLAO PSF is fitted to a Moffat function (see Villecroze et al. (2012)), allowing to describe the estimated PSF with four parameters.

For MUSE Wide Field Mode, the GLAO performance is really dominated by fitting and anisoplanatic aspects, thus very few online information coming from the AO system itself is required (r_0, L_0 and C_n^2) in addition to the typical characteristics of the AO system (number of corrected modes), telescope (pupil shape) and instrument (internal aberrations).

The computation time of PSF reconstruction has been identified as one of the main issues, i.e. the FoV and the wavelength sampling of MUSE will lead to a large number of PSFs to compute. Even though there is no need for a real time reconstruction process, it is important to keep in mind that the huge amount of data to be processed will require a computation time as small as possible. Optimization of the PSF reconstruction process includes the use of V_{ii} functions instead of U_{ij} functions and optimization of the numerical computation of the covariance matrix (N=989). By doing so, the PSF reconstruction computation time can be reduced from over 27 hours to less than 2 hours. It is expected that after coding the algorithm in C, the execution time can be taken under 5 minutes.

Tests for the algorithm were done using end-to-end simulation tools developed at ONERA. A first sensitivity analysis has been conducted showing that accuracy of 1 to 2 % is required for the estimation of both seeing and C_n^2 profile (ground vs high altitude).

Future work in the algorithm includes:

- Finalization of the improvement of algorithm speed.
- Finalization of the error budget and the sensitivity analysis.
- Finalization of performance assessment.
- Test in labs.
- Final and detailed algorithms allowing an implementation in the MUSE data reduction pipeline.

3.2.20. 2013:A new method for AO PSF-R

The typical PSF estimation method, defined by Véran, is based on a least-squares (LS) approach that requires estimates for the noise variance and covariance of the aliasing on the mirror modes needed to unbias the covariance matrix of the modes.

Exposito et al. (2013) present a new method to estimate the AO PSF based on a maximum likelihood approach. This method can be used to estimate the covariance of the residual phase, including the propagation of the noise on the DM and the Fried parameter r_0 during the observation.

A probabilistic approach is used to estimate $C_\mathcal{E}$, the covariance matrix of the modes of the residual phase, in a basis containing an infinite number of modes to explicitly take into account the effects of aliasing on the measurement, noise and the loop temporal bandwidth. This method allows to estimate the most likely covariance matrix of the modes measurements taking into account the effect of aliasing, temporal bandwidth and noise. To do this, it is necessary to have an accurate estimate of the correlation terms between the parallel and the perpendicular components of the residual phase. These terms have a significant effect on the measurements and must be taken into account when estimating the parallel component.

Using 200 Karhunen-loéve (KL) modes, the residual phase ϕ_ϵ is projected (with a least-squares projection) onto the modes such that:

$$\phi_\epsilon = \epsilon KL \tag{3.9}$$

The vector ϵ is the expansion vector of the residual phase ϕ_ϵ in the 200 KL-basis. The covariance matrix is then defined as

$$C_\epsilon =< \epsilon\epsilon^t > \tag{3.10}$$

C_ϵ is decomposed in 4 components:

- $C_{\epsilon\perp}$: This term represents the correlations between high order modes uncorrected by the mirror. KL modes being statistically independent, the covariance matrix is diagonal. Assuming a Kolmogorov phase, the covariance of these modes depends only on the parameter r_0.
- $C_{\epsilon\|}$: Because of the correction of the AO system, correlations between the DM modes appear: the covariance matrix of the modes is not diagonal. They stand for the residual component in the mirror space including the temporal residuals, the aliasing and the propagation of measurement noise. In addition, they depend on the correction performance.
- $C_{\epsilon\|\perp}$: This cross term is the coupling between the modes of high spatial frequencies and modes in the mirror space (corrected). Erroneous commands are sent to the DM, due to the aliasing on the sensor and the finite temporal bandwidth. To get the covariance $C_\epsilon \|$ from the covariance of measurements, it is necessary to have an estimate of the terms $C_{\epsilon\|\perp}$.
- $C_{\epsilon\perp\|}$: The transposed matrix of $C_{\epsilon\|\perp}$.

$C_{\epsilon\|\perp}$ can be analytically estimated from the temporal aspects of the loop as

$$C_{\epsilon\perp} =< \epsilon_\| \epsilon_\perp^t >= -\sum_{m=1}^{n} g(1-g)^{m-1} D^+ D'_\infty < \epsilon_\perp^{i-m} \epsilon_\perp^{it} > + \sum_{m=1}^{n} (1-g)^{m-1} < \Delta\Phi_\|^{i-m} \epsilon_\perp^{it} > \tag{3.11}$$

where n is the number of iterations, g is the loop gain, D^{+} is the command matrix on the mirror modes, D'_{∞} is the KL interaction matrix in the DM orthogonal space and $\Delta\phi_{\|} = \phi_{\|}^{i-m+1} - \phi_{\|}^{i-m}$.

The cross term $C_{\epsilon\|\perp}$ only depends on the temporal covariance matrices for the modes in ϕ_{atm}.The Kolmogorov spectrum and the Taylor hypothesis reduce the parameter space for the cross term to two key parameters: r_0 and the wind speed v. This method to estimate the cross-term have been tested on a Canary-like system (Gendron et al., 2011). The estimation error (the difference between the exact covariance recovered from the simulation and the estimated covariance decreases when n increases.

With this estimation, the ML method was tested in a simplified case. The variance of the modes was successfully estimated with an accuracy better than 1%.

3.2.21. 2013: Point spread function reconstruction on the MCAO Canopus bench

In this work, Gilles et al. (2013) use the Gemini South Canopus AO bench to validate the LGS MCAO PSF reconstruction algorithm proposed in 2012(see section 3.2.17) for the TMTs AO system.

Canopus AO bench comprises five SH WFSs with 16x16 subapertures, two DMs conjugate to ground (DM0), and 9km (DM9). The 5 LGSs asterism has a X shape of 1 arcmin x 1 arcmin. It also includes a dedicated fast tip/tilt mirror and 3 natural guide star low-order WFSs.

To test the PSF reconstruction algorithm the following experiment was executed: Von Kármán frozen flow turbulence was injected in closed loop to DM0 with a zero integrator gain to simulate open loop dynamics. Static non-common path aberration (NCPA) commands were applied to both DM0 and DM9. A bright calibration source was used as guide star, and a time history of WFS slopes and K- band short exposure turbulence images (16x16 pixel) were captured. A time history of short exposure static images (24 x 24 pixel) were also recorded without turbulence injected. All data is further degraded by

8 milliarcsec 2-axis RMS tip/tilt jitter induced by the large vibration levels present on the bench.

The focus of this work was on tip/tilt-removed PSF-R. The tip/tilt component was removed at every frame from WFS slopes and short exposure images. Ninetynine percent level PSF-R accuracy was achieved in K-band, corresponding to a 66-fold accuracy improvement between point spread functions estimated without and with wavefront sensor telemetry.

Future work considers obtaining data sets with multiple calibration sources at finite and infinite range, and turbulence injected onto two deformable mirrors to test the effects of anisoplanatism and tomography.

4. STUDY CASE: PSF RECONSTRUCTION IN NICI, THE NEAR INFRARED CORONOGRAPHIC IMAGER AT GEMINI SOUTH OBSERVATORY

4.1. Introduction

The goal of this thesis is to implement the PSF-R algorithm in NICI, a facility instrument installed at Gemini South Observatory. This is part of a project that was conceived as a collaboration between Gemini South Observatory (GSO) and Pontificia Universidad Católica (PUC). The development is done using APETy (see section 3.2.15), a Yorick code written for YAO(Yorick Adaptive Optics) where the basic algorithm from Véran is implemented.

The applied methodology is first simulate the NICI AO loop and estimate the long exposure PSF using Véran's algorithm. Second, the estimation error sources for the reconstructed PSF are assessed by comparison with the simulated long exposure PSF. Later, using real data from NICI AO telemetry, the estimated PSF is computed and its quality is evaluated using science images.

4.2. NICI: The Near Infrared Coronographic Imager

NICI is conceived in the context of a dedicated circumstellar imaging campaign and is in operations at GSO since 2009. The instrument is a dual-channel imager and includes a dedicated Lyot coronagraph (Artigau et al. (2008)).

NICI is optimized for the detection of large Jovian-type planets around nearby stars. It can enhance its sensitivity by spectrally differenciating two images, inside and outside the strong near-infrared methane absorption features, found in substellar objects cooler than 1400K. Imaging is done on each channel by a 1024x1024 pixels ALADDIN InSb array working between 1 to 5 μm. The image scale is 18 mas/pix, and the field of view is 18 x 18 arcseconds.

NICI AO is an 85-element curvature AO system, the WFS detector is equipped with 85 avalanche photo-diodes (APD), the operational frame rate is 1300 Hz and the frame delay is 769 μs (1 frame).

4.3. Previous work on PSF reconstruction for NICI

On July 2011, a collaboration project between GSO and PUC started to implement the PSF reconstruction for NICI. The preliminary work was reported in Hartung et al. (2011) (see section 3.2.15).

The work includes Monte Carlo simulations on YAO and PSF reconstruction with APETy. NICI is modeled as an AO loop operating at a frequency of 1300 Hz and a loop gain set to 0.3. Detectors are represented by a two dimensional array of 256 x 256 elements. The YAO simulations included 10000 iterations and were done for $r_0 \approx 19.75$ cm and $r_0 \approx 13.16$ cm.

The schema shown in Figure 4.1 summarizes the process for implementing the PSF estimation algorithm.

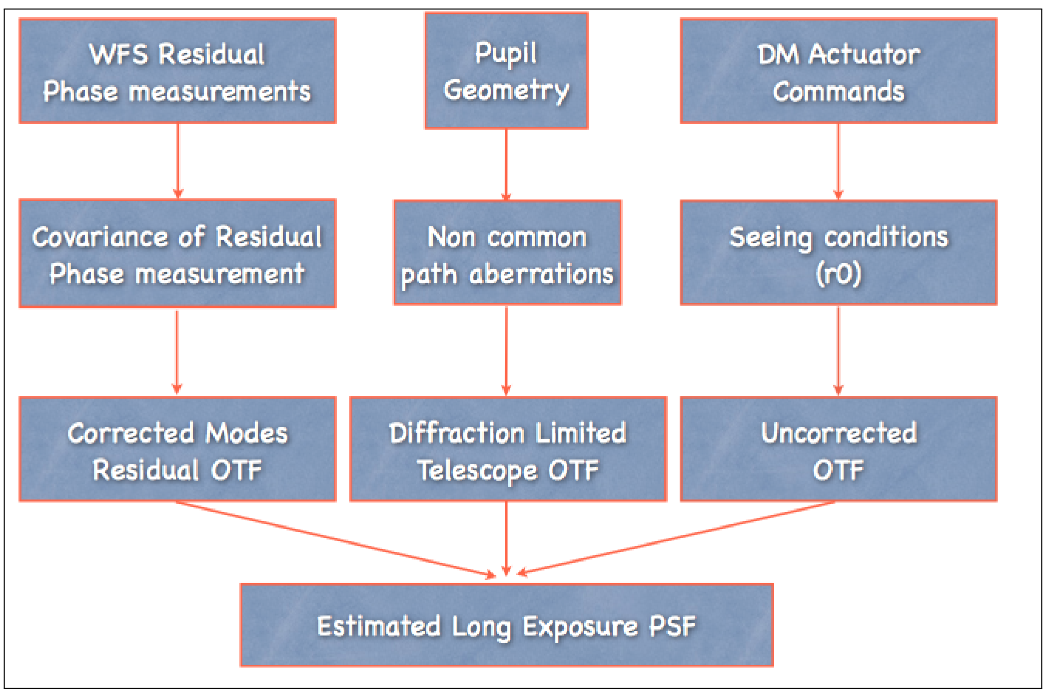

FIGURE 4.1. PSF-R process diagram.

The main effort in this implementation was focused on the estimation of the uncorrected OTF or high order phase component. The estimation of r_0 from DM commands was not included.

Two methods were used to evaluate the high order phase $\phi_\perp$ from YAO simulations: The first method considered $\phi_\perp$ as the difference of the residual phase $\phi_\mathcal{E}$ and the projection of the residual phase over the mirror modes $\phi_{\mathcal{E}\|}$ (phase split on the DM)

$$\phi_\perp = \phi_\mathcal{E} - \phi_{\mathcal{E}\|} \tag{4.1}$$

The second method evaluated $\phi_\perp$ as the difference of the residual phase $\phi_\mathcal{E}$ and the mirror shape calculated from the WFS measurement of the residual phase $\mathcal{W}_{\phi_\mathcal{E}}$, the command matrix $\mathcal{D}^+$ and the mirror modes $\mathcal{M}$ (phase split on the WFS)

$$\phi_\perp = \phi_\mathcal{E} - \mathcal{D}^+ \mathcal{W}_{\phi_\mathcal{E}} \mathcal{M} \tag{4.2}$$

The reconstructed PSF, compared to the simulated long exposure PSF, was overestimated inside the first diffraction ring for both methods. However, the method using phase split on the WFS had the lowest error (see figure 4.2). In addition, it was found that the WFS noise contribution was not significative for the case of a bright guide star.

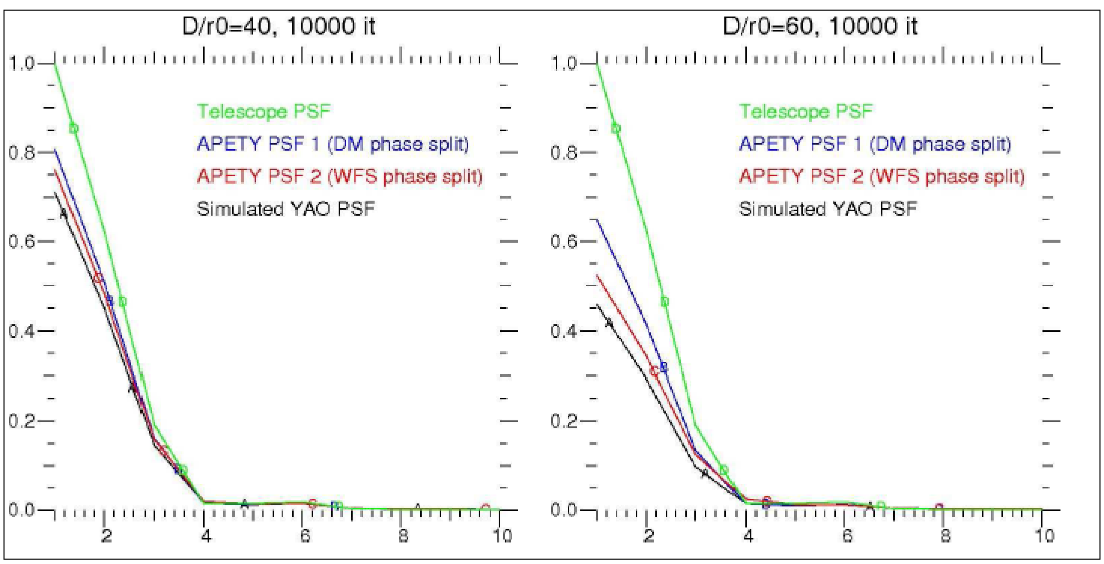

FIGURE 4.2. PSF-R results as obtained with APETy on (Hartung et al., 2011). The graphs show the circular average for the simulated long exposure PSF and the estimations obtained using DM phase split and WFS phase split. Left: case for D/r_0=40. Right: casefor D/r_0=60.

4.4. Working plan for PSF Reconstruction applied to NICI

After this preliminary result, the subsequent effort was focused on the following goals:

- Finding the cause of PSF overestimation.
- Searching for a better method of evaluating the high order residual phase contribution and aliasing effects.
- Scaling of the PSF-R simulation to 1024 x 1024 pixels.
- Use of real data from telescope and AO system: Pupil, interaction matrix and command matrix.
- Estimation of D/r0 using real data from NICI DM commands
- Perform PSF-R using real data from NICI
- Evaluation of the quality of the estimated PSF using science images

The methodology for this work is to perform PSF reconstructions using APETy using data from AO simulations.

(i) The estimated PSF will be compared to the long exposure PSF, obtained from simulations, to assess the estimation errors and identify the sources of such errors.

(ii) From the estimation errors assessment, the PSF reconstruction algorithm implemented in APETy will be fine tuned

(iii) A model will be build to predict the performance of the algorithm.

(iv) Finally, after the minimization of the estimation errors, the high order phase contributions obtained from simulations will be saved and used in the PSF reconstruction for data from on-sky observations made with NICI AO.

4.4.1. Finding the Cause for PSF over-estimation

The PSF structure is mainly sensitive to non common path aberrations and atmospheric parameters (see 3.2.16). As expressed by 2.127, the long exposure OTF is made by the product of three contributions: the telescope optics OTF, the OTF from the mirror component of the residual phase and the OTF from the orthogonal component of the residual phase.

In the initial work (see 4.3) ideal optics were assumed and r_0 was given; therefore the error in the PSF estimation is coming from the evaluation of the OTFs for the mirror component and the orthogonal component of the residual phase.

According to section 2.7, to obtain the OTF of the mirror component of the residual phase is necessary to calculate $\mathcal{C}_{\mathcal{E}\mathcal{E}}$, the covariance matrix of the measured error , which from equation 2.133 is:

$$\mathcal{C}_{\mathcal{E}\mathcal{E}} \approx \mathcal{C}_{\hat{\mathcal{E}}\hat{\mathcal{E}}} - \mathcal{C}_{nn} + \mathcal{C}_{rr}$$

where $\mathcal{C}_{\hat{\mathcal{E}}\hat{\mathcal{E}}}$ is the covariance matrix of the WFS measurements, $\mathcal{C}_{nn}$ is the covariance of the measurement error and $\mathcal{C}_{rr}$ is the covariance matrix of the remaining error coming from the aliasing affecting the WFS.

The calculation of $\mathcal{C}_{\hat{\mathcal{E}}\hat{\mathcal{E}}}$ and $\mathcal{C}_{nn}$ is straightforward from the WFS measurements and can be discarded as the source of the estimation error.

$\mathcal{C}_{rr}$ is calculated from simulations of the high order phase. The OTF for the orthogonal phase component is also calculated from the simulation of the high order phase. As described in section 4.3, APETy presents two methods to evaluate the high order phase component: phase split on the DM and phase split on the WFS.

From the previous analysis and the results from Hartung et al. (2011), it can be inferred that the methods used by APETy for evaluating the high order phase component is the main cause of the error in the PSF estimation. This hypothesis creates the need for a better method to evaluate the high order phase.

4.4.2. A new strategy for evaluating the high order residual phase contribution

It has been suggested (Véran et al., 1997) that the evaluation of the high order residual phase can be done by creating phase screens with Kolmogorov statistics, removing their low order components. Hence, by simulating the AO loop with high order components only, will allow to have a statistical estimation of the aliasing in the WFS and to find the structure function of the uncorrected phase.

In YAO, simulated phase screens are created by the built-in function *create_phase_screens*; this function generates a phase screen computed by modulating a random phase with the von Kármán frequency response and later applying an inverse Fourier transform to obtain the phase screen. This function can be modified to apply a spatial high-pass filter over the von Kármán spectrum, generating a high-order phase screen. Figure 4.3 shows the resultant spectrum after filtering the Von Kármán spatial spectrum with high-pass filters of order 1, 2 and 4.

Evaluation of the high order phase component was tested using filtered phase screens with different spatial cut-off frequencies and outer scale $L_0=\infty$. It was found dependence in the error of the PSF estimation and the spatial cut-off frequency of the phase screen. For higher spatial cut-off frequencies, the PSF tends to be underestimated; for lower spatial cut-off frequencies the PSF is over estimated. It was possible to observe a transition from PSF over-estimation to PSF under-estimation, leading to conclude that an optimal cut-off frequency exists, and that must correspond to the WFS cut-off frequency.

4.4.3. NICI WFS spatial cut-off frequency

To estimate the spatial cut-off frequency of NICI curvature WFS, two approaches were followed: Analysis of the WFS spatial frequency response and analysis of the WFS's geometry.

In the first approach, the WFS spatial frequency response is obtained from the Fourier transform of the WFS spatial sampling function. The WFS spatial sampling function is represented by the image of the center points of the sub-apertures, that can be obtained

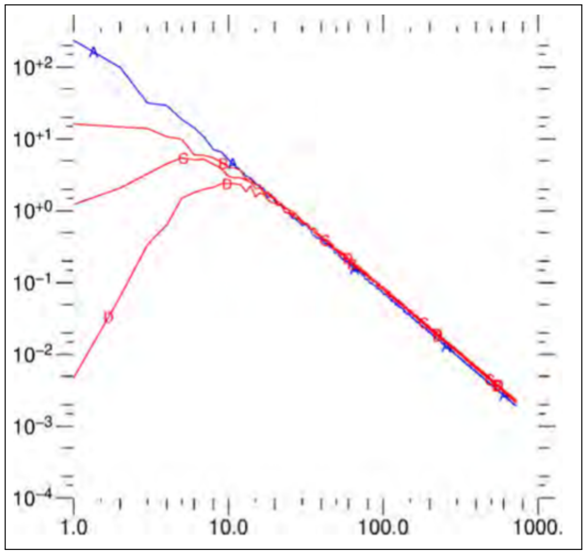

FIGURE 4.3. Filtered von Kármán spatial spectrum. Original spectrum is in blue. Red spectrums from top to bottom correspond to high pass filters of order 1, 2 and 4.

from the WFS geometry shown by figure 2.17. The WFS geometry is irregular; thus more than one sampling frequency is expected. From the obtained WFS response, shown in figure 4.4, three main sampling frequencies can be observed, and from simple inspection they can be roughly estimated to be around $\kappa \approx 1.5$, $\kappa \approx 3.0$ and $\kappa \approx 4.0$. The roll-off slope in the WFS frequency response begins for $\kappa > 5.0$. Therefore, the WFS cut-off frequency can be estimated to be $f_{co} \approx 5.0[1/m]$.

In the second approach, the cut-off frequency f_{co}, can be estimated from the average size of the sub-apertures S_{sa}. Assuming that the sub-apertures have circular geometry, an equivalent sub-aperture average radius, r_{sa} can be calculated as $r_{sa} = \sqrt{S_{sa}/\pi}$. The spatial sampling frequency is defined as $f_s = D/(2r_{sa})$, with D the telescope pupil diameter in pixels. In Nyquist criteria, the maximum sampled frequency is half of the sampling frequency, thus in this case $f_{co} = D/(4r_{sa})$.

From the WFS geometry image, the average sub-aperture size is $S_{sa} = 1469[pixels^2]$, and the average equivalent radius is $r_{sa} = 21.6[pixels]$. The cut-off frequency is $f_{co} = 4.67[1/m]$, which is fairly close to the estimation from the WFS frequency response.

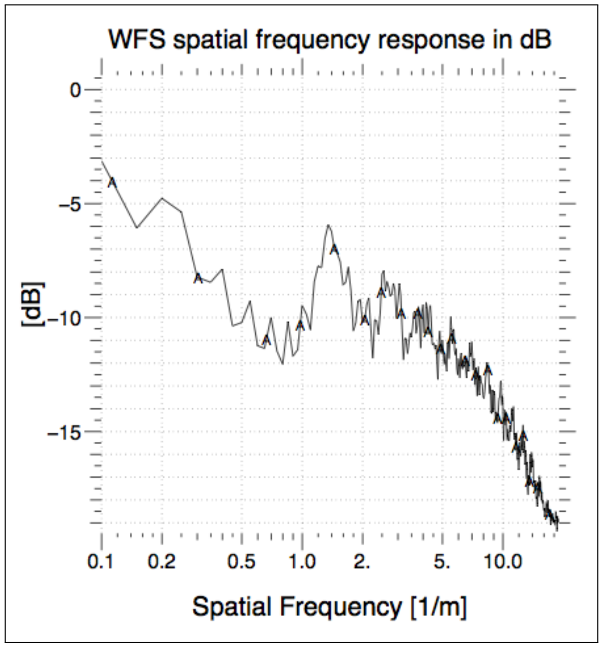

FIGURE 4.4. WFS spatial frequency response.

Making the same exercise, but assuming square sub-apertures, the average side is calculated as $a = \sqrt{S_{sa}}$. The sampling frequency is defined as $f_s = D/a$, and the cut-off frequency is $f_{co} = D/2a$. From this supposition, the cut-off frequency is estimated as $f_{co} = 5.27[1/m]$.

Taking in account the results from both approaches it seems that assuming the cut-off frequency as $f_{co} = 5.0[1/m]$ will be a reasonable starting point for evaluating aliasing and the uncorrected phase contribution to the long exposure PSF.

4.4.4. Optimal high-pass filter

The optimal high-pass filter minimizes the error in the estimation of the high order component of the PSF. The parameters defining the filter are the spatial cut-off frequency and the filter order. The spatial cut-off frequency was estimated in the previous section; therefore, this section is focused on the estimation of the optimal filter order.

Analysing the WFS spatial frequency responses in figure 4.4, the roll-off slope is approximately 20 dB per decade; thus it is reasonable to assume that the WFS is a first order low-pass filter. In consequence, it is reasonable to suppose that the optimal high-pass filter is a first order filter.

To validate the aforementioned assumption, the error in the PSF reconstruction was evaluated for cases using ideal, first order and second order filters. The results are compared to the base case presented in section 4.3.

The test with the ideal high-pass filter showed a better fit, in the circular average, of the simulated long exposure PSF and the estimated PSF. However, none of the remanent speckles was reproduced in the estimated PSF image. This effect is explained because, in the PSF high order component, there are two phenomena evaluated: the uncorrected phase and the WFS aliasing. The remanent speckles, as explained in section 2.5.6, are due to the uncorrected phase in the system; thus the ideal high-pass filter isolates the WFS aliasing but eliminates the uncorrected phase effect. The test with a second order high-pass filter did not show any improvement with respect to the test with the ideal filter.

Finally, the test with a first order high-pass filter obtained reproduction of the remanent speckles and better match for the circular average of the estimated PSF. The mean square error in the image estimation was improved in a factor of 7 with respect to the base case.

Figure 4.5 shows the comparison of the circular average for the long exposure PSF and the estimated PSF. It can be seen that center pixels over-estimation was minimized and that the pixels away of the center tend to be over-estimated. Figure 4.6 shows the image of the long exposure PSF and the estimated PSF. The details on the remanent speckles can be appreciated.

4.4.5. APETy code modifications to support different size images and AO loop simulation performance

The APETy's original code only supported images of 256x256 pixels, which was fine for AO loop simulation with YAO and test of the PSF reconstruction algorithm. The imaging system of NICI is 1024x1024 pixels; therefore, it was necessary to tweak the APETy code for including support of different size images. The PSF reconstruction results with

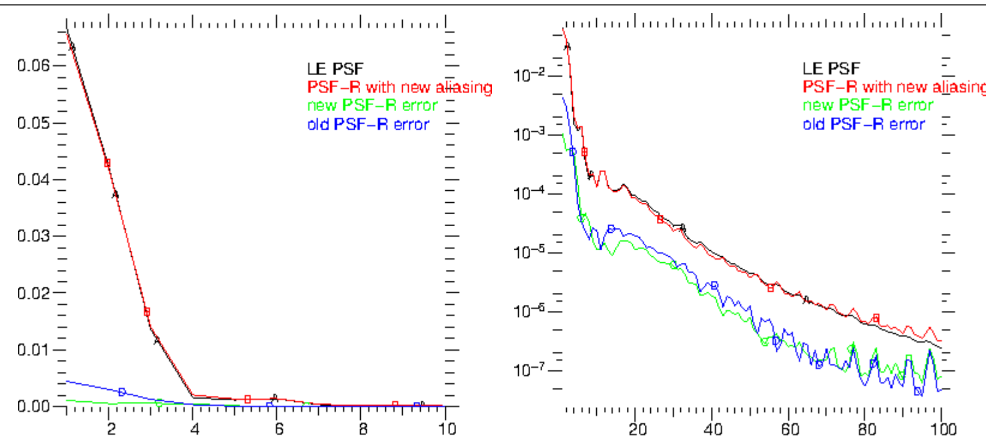

(a) (b)

FIGURE 4.5. PSF-R with filtered phase screens and D/r0 = 40. Long exposure PSF (black), Estimated PSF(red), old error(blue) from previous APETy results on 2011 and error with filtered phase screen(green). (a) PSF-R results for center pixels circular average (linear scale). (b) PSF-R results for full circular average (log scale)

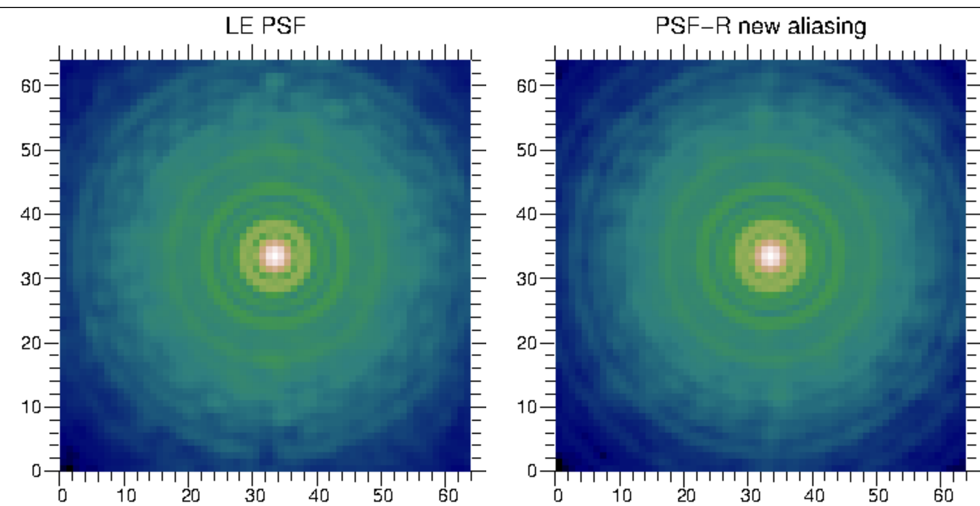

(a) (b)

FIGURE 4.6. Images for long exposure PSF and estimated PSF from simulation using filtered phase screens and D/r0 = 40. (a) Long Exposure PSF image. (b) Estimated PSF image.

an imaging system defined to 1024x1024 pixels are similar to the results presented in the previous section for the 256x256 pixels case.

The AO simulations were run in a computer with a quad-core, 2.2 GHz processor and 10 Gigabytes of RAM. The AO loop simulations using 256x256 arrays run in average at 8.7 iterations per second. For AO loop using 1024x1024 arrays, the simulation run at 0.27 iterations per second. The increment in the simulation time was defined by the processor speed. In order to improve the speed in AO system with bigger image size it will be necessary to explore solutions using parallel computing or programming using graphics processing unit (GPU). However, this issue is out of the scope of this thesis.

4.4.5.1. U_{ij} functions for NICI PSF reconstruction

The PSF reconstruction algorithm requires the calculation of $\frac{N(N-1)}{2}$ U_{ij} functions, where N is the number of modes of the AO system. NICI AO has 85 modes; thus a total of 3570 U_{ij} functions have to be calculated and applied for the estimation of $D_{\phi_{\varepsilon\|}}$ (the structure function of the mirror phase component) and $D_{\phi\ alias}$ (structure function of the aliasing component).

The U_{ij} functions are calculated in APETy using equation 2.126. The resulting U_{ij} functions are arrays of 842 x 842 pixels, and take approximately 8 seconds to calculate each of them. The PSF reconstruction process can take over 7 hours using on-the-fly calculation of the U_{ij} functions. Previous calculation and storage of all the U_{ij} functions is an effective workaround that allows to run the PSF reconstruction in approximately 6 minutes. The total storage size required for the 3570 U_{ij} functions is 10 Gigabytes. Figure 4.7 shows the image of the function $\mathrm{U}_{58,19}$.

4.4.5.2. Gemini Telescope pupil mask

Figure 4.8 shows the pupil mask of the Gemini telescope; this is a 1024x1024 pixels image. The pupil mask was integrated in the code of YAO, to complete the simulation model of NICI AO. YAO simulations using the Gemini telescope pupil were consistent in Strehl with the previous cases using a pupil generated by YAO. A slight change in the simulation results was observed due to the change in the telescope PSF.

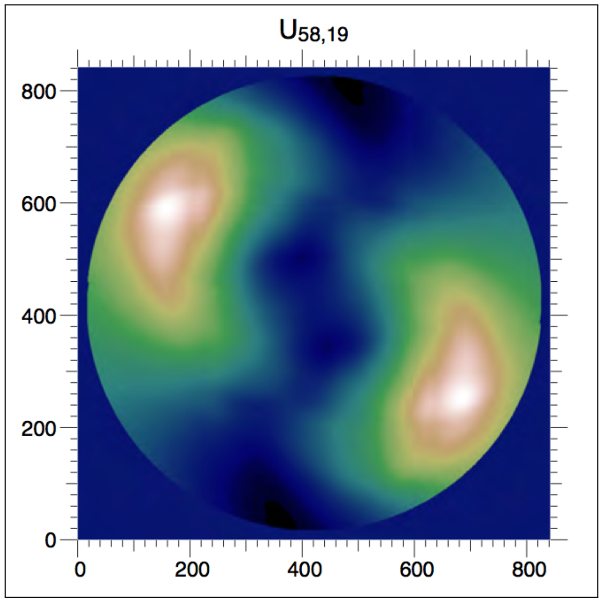

FIGURE 4.7. Image of function $U_{58,19}$.

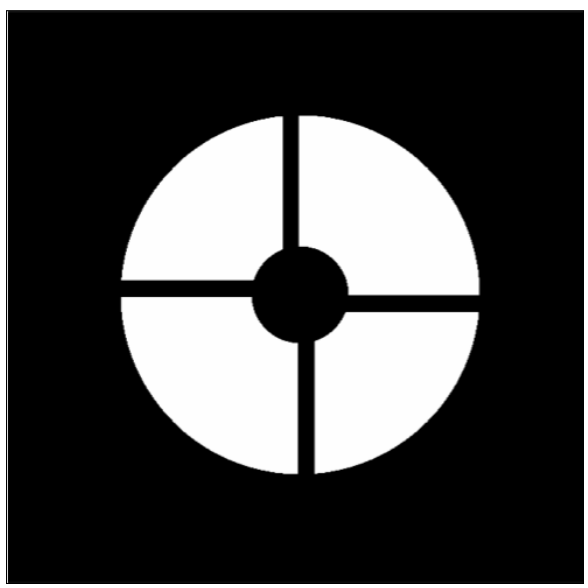

FIGURE 4.8. Gemini telescope pupil mask.

4.4.5.3. NICI AO measured interaction matrix and command matrix

In a similar way as for the Gemini telescope pupil mask, the NICI AO measured interaction matrix and the command matrix were integrated in the code of YAO. The aforementioned matrices are shown in figure 4.9. It was expected that using the NICI AO matrices the simulations in YAO would provide a better description of NICI AO behavior, but this was not case and the simulated AO loop was not able to compensate the atmospheric turbulence.

Comparing the simulated matrices generated by YAO and the NICI AO measured matrices, it is found that their elements have a magnitude difference in the order of 10^4. It was attempted to scale the measured matrices to the magnitude order of YAO matrices, but no improvements in the AO loop simulation were seen. To explain this situation it is necessary to recall that YAO uses the influence functions to calculate the mirror shape from the mirror commands; therefore, the system response in the simulated AO loop is strongly dependent in the relationship between the influence functions and the command matrix. As the NICI AO influence functions were not available, the use of the measured matrices was discarded for simulations on YAO/APETy. Nevertheless, these measured matrices need to be included in the PSF reconstruction for NICI when using observation data.

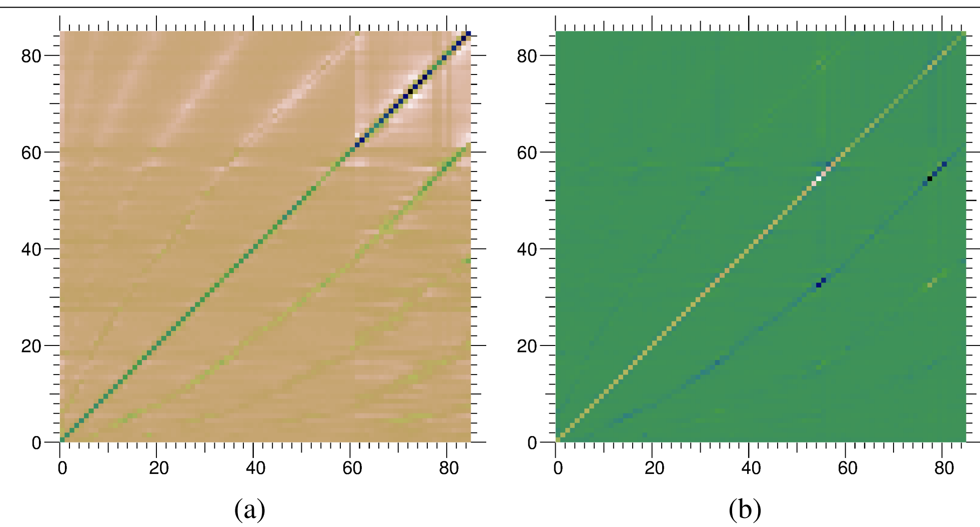

FIGURE 4.9. NICI AO measured interaction and command matrices. (a) NICI AO interaction matrix. (b) NICI AO command matrix.

4.5. Simulation of NICI PSF-R using Gemini pupil mask and a pupil grid of 1024x1024 pixels

This simulation is the last test in APETy before attempting PSF reconstruction for NICI using data from on-sky observations. The PSF reconstruction was done using filtered phase screens and the features incorporated in the previous section. The results show error level similar to the results found in the 256x256 pixels case presented in section 4.4.4. Figure 4.10 shows the simulated long exposure PSF and the estimated PSF for D/r$_0$=40. A characterization of the variables involved in the PSF reconstruction process follows.

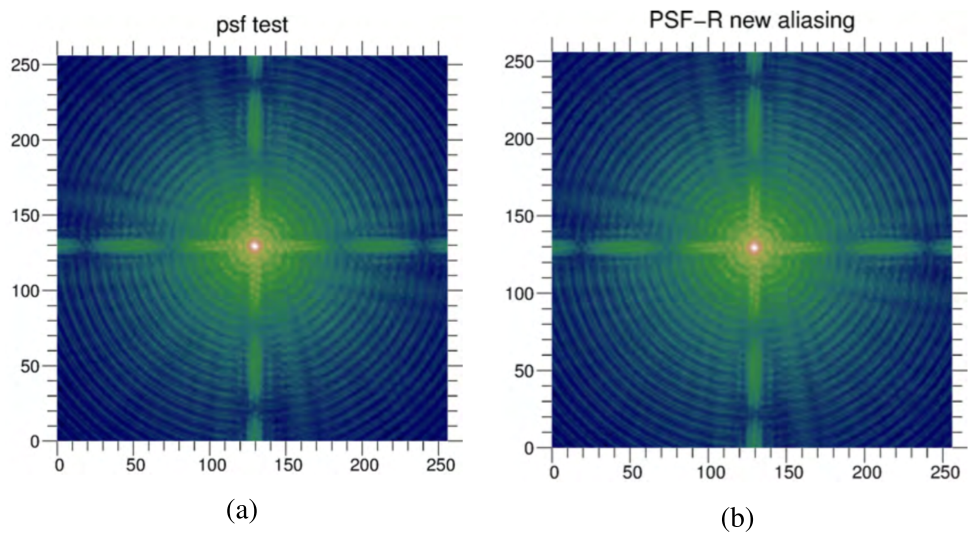

FIGURE 4.10. Simulated long exposure PSF and estimated PSF using Gemini Telescope pupil mask, 1024x1024 pixels, D/r$_0$ = 40. (a) Simulated long exposure PSF. (b) Estimated PSF.

4.5.1. The high order contributions $\mathcal{C}_{rr}$ and $D_{\phi\perp}$

The high order contributions, $\mathcal{C}_{rr}$ and $D_{\phi\perp}$, were calculated as indicated in section 2.7.3. A YAO simulation was run, using spatial filtered phase screens with spatial cut-off frequency of $\kappa = 5[1/m]$ and D/r$_0$=1. The high order phase, $\phi_\perp$, realizations were measured obtaining $\mathcal{W}(\phi_\perp)$, the high order WFS measurements. From these measurements, the covariance matrix of the uncorrected phase $\mathcal{C}_{rr}$ was obtained as

$$\mathcal{C}_{rr_{\frac{D}{r_0}=1}} = \mathcal{D}^{+}\sigma^2_{\mathcal{W}\perp}(\mathcal{D}^{+})^T \tag{4.3}$$

Figure 4.11 shows $\mathcal{C}_{rr}$ and $D_{\phi\perp}$ scaled to D/r$_0$=40.

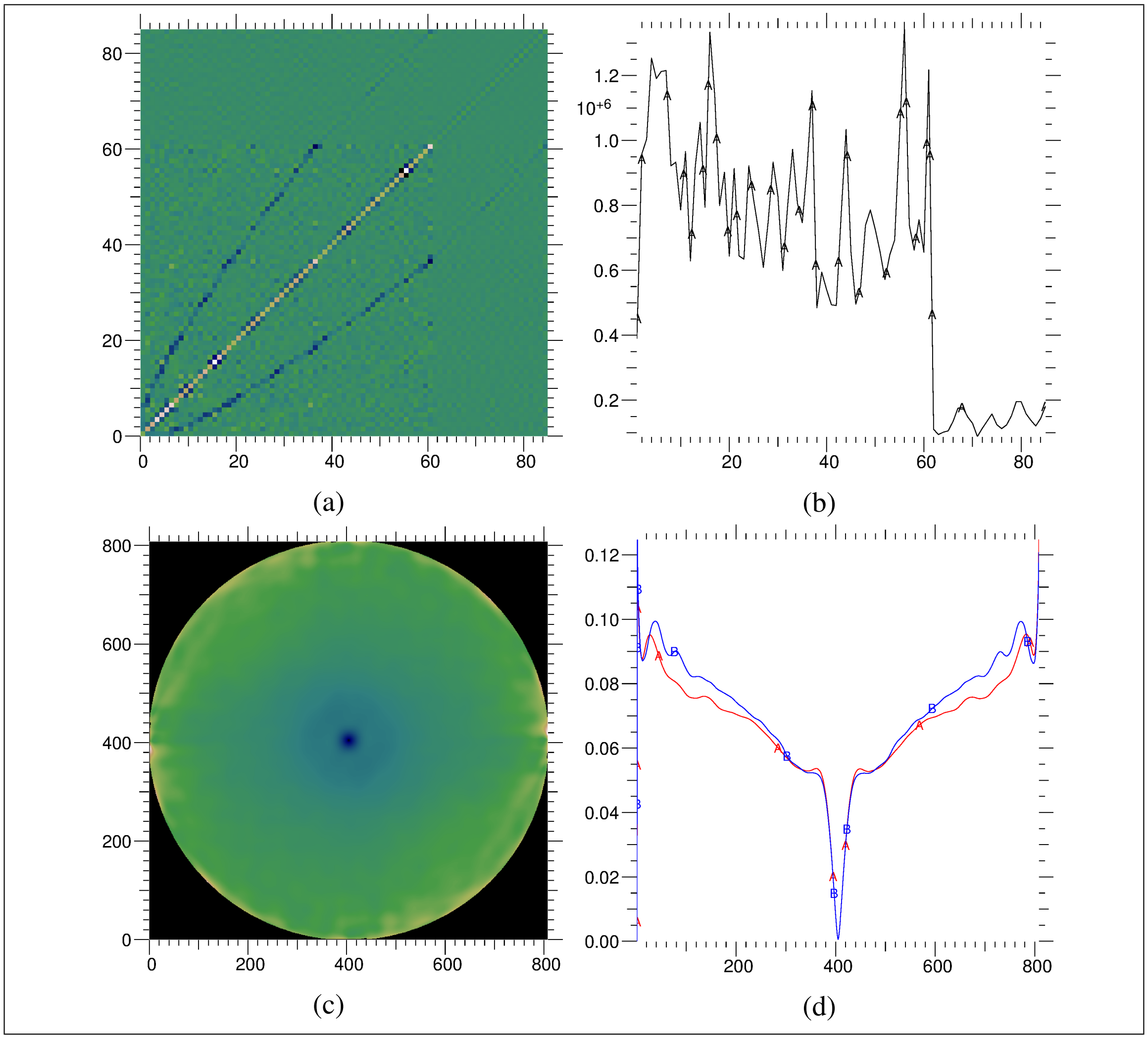

FIGURE 4.11. High order components $\mathcal{C}_{rr}$ and $D_{\phi\perp}$ calculated with D/r$_0$ = 40. (a) $\mathcal{C}_{rr}$, the covariance matrix of the orthogonal residual phase. (b) $\phi_\perp$ variance per subaperture. (c) $D_{\phi\perp}$, the structure function of the orthogonal phase. (d) $D_{\phi\perp}$, x-x(red) and y-y(blue) transversal cuts.

4.5.2. Estimation of $\mathcal{C}_{\hat{\mathcal{E}}\hat{\mathcal{E}}}$ and $\mathcal{C}_{\mathcal{E}\mathcal{E}}$

$\mathcal{C}_{\hat{\mathcal{E}}\hat{\mathcal{E}}}$ is defined by equation 2.130 and is calculated using the covariance matrix of the WFS measurements, $\mathcal{C}_{\mathcal{E}\mathcal{E}}$, is defined by equation 2.133 and is calculated from $\mathcal{C}_{\hat{\mathcal{E}}\hat{\mathcal{E}}}$, $\mathcal{C}_{rr}$ and $\mathcal{C}_n$. Figure 4.12 shows $\mathcal{C}_{\hat{\mathcal{E}}\hat{\mathcal{E}}}$ and $\mathcal{C}_{\mathcal{E}\mathcal{E}}$.

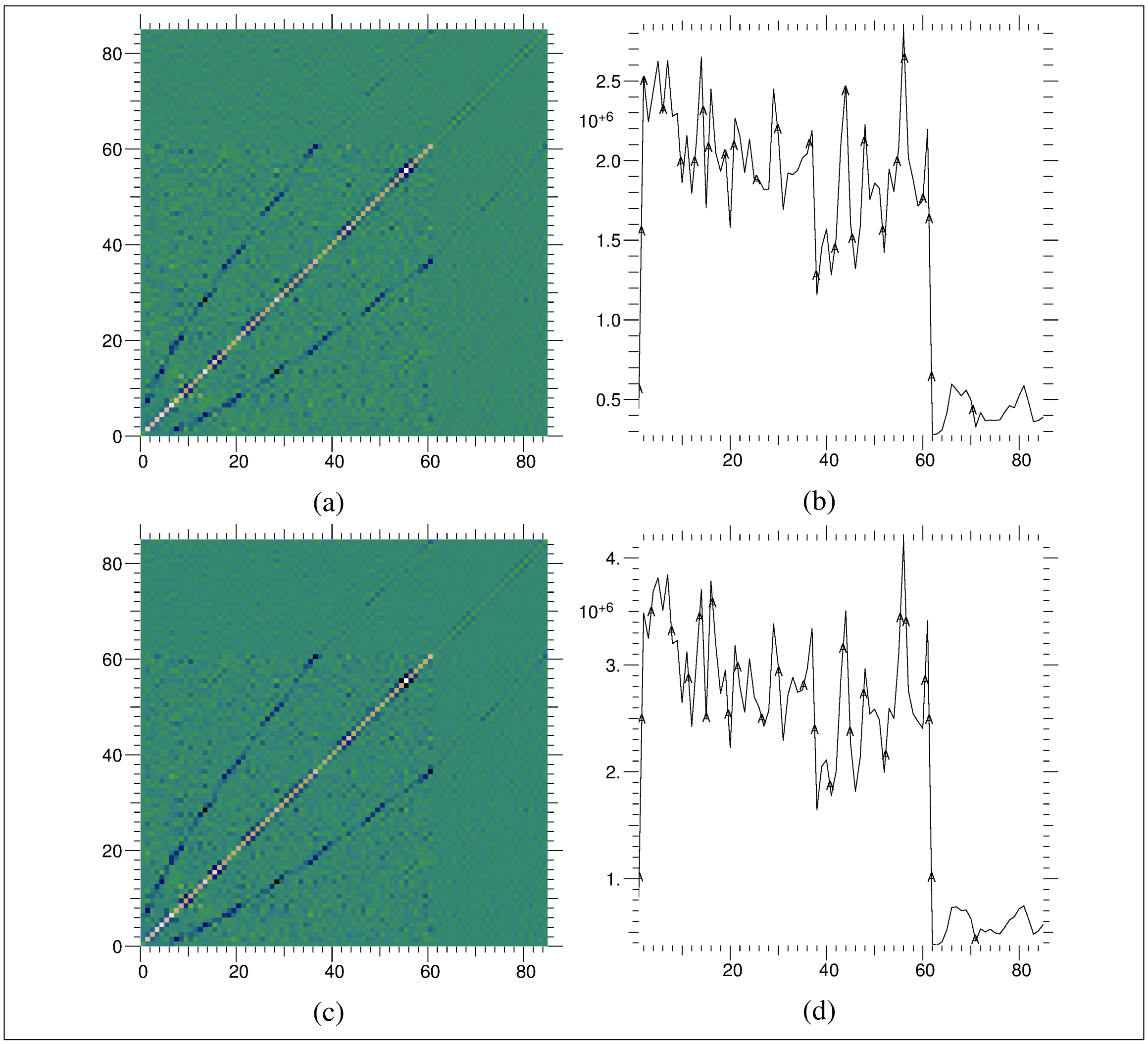

FIGURE 4.12. $\mathcal{C}_{\hat{\mathcal{E}}\hat{\mathcal{E}}}$ and $\mathcal{C}_{\mathcal{E}\mathcal{E}}$ covariance matrices.(a) $\mathcal{C}_{\hat{\mathcal{E}}\hat{\mathcal{E}}}$ covariance matrix (b) Estimation of the error variance per subaperture. (c) $\mathcal{C}_{\mathcal{E}\mathcal{E}}$ covariance matrix. (d) Measurement error variance per subaperture.

4.5.3. The corrected phase structure function

The corrected phase structure function is defined by equation 2.124. This component is made by the sum of the corrected phase error $\mathcal{E}_{\|}$ and the aliasing error $\mathcal{E}_{alias}$, where:

$$\begin{aligned} D_{\phi\|} &= \sum_{i,j} (\mathcal{C}_{\mathcal{E}\mathcal{E}}(i,j) + \mathcal{C}_{\mathcal{E}\mathcal{E}}(i,j)^T) * U_{ij} \\ D_{\phi\ alias} &= \sum_{i,j} (\mathcal{C}_{rr}(i,j) + \mathcal{C}_{rr}(i,j)^T) * U_{ij} \end{aligned} \tag{4.4}$$

Figure 4.13 shows the resulting structure functions.

4.5.4. The turbulent atmosphere OTF and the telescope OTF

The turbulent OTF can be expressed as:

$$OTF_{turb} = exp(-0.5D_{\phi\|})exp(-0.5D_{\phi\ alias})exp(-0.5D_{\phi\perp}\frac{2\pi}{\lambda}) \tag{4.5}$$

Figure 4.14 shows the obtained turbulent atmosphere OTF. Figure 4.15 shows the telescope OTF and PSF for 1.65 [μm].

4.5.5. The long exposure OTF and the estimated long exposure OTF

The estimated long exposure OTF is calculated as the multiplication of the turbulent atmosphere OTF and the telescope OTF. Figure 4.16 shows the long exposure OTF obtained from simulation and the estimated long exposure OTF from the PSF reconstruction process.

4.6. NICI AO PSF reconstruction implementation

After the APETy code modifications, the PSF-R implementation for NICI AO was ready for use with on-sky data. Two datasets of on-sky observations with NICI were available to test the implementation. These datasets correspond to observations done for AO loop gain characterization that were obtained during scheduled engineering night test (ENT) activities.

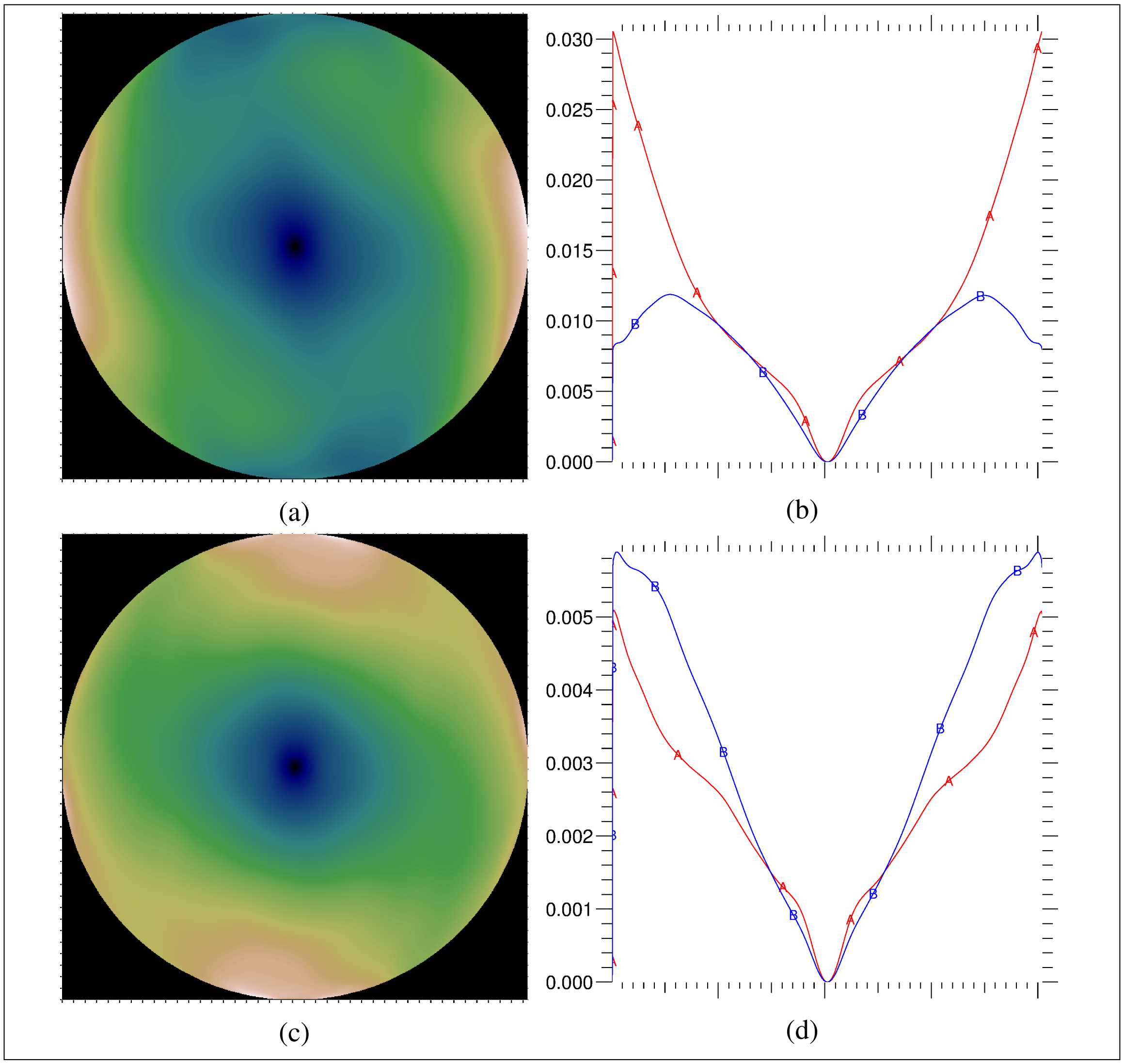

(a) (b) (c) (d)

FIGURE 4.13. Structure function for corrected phase error phase and aliasing phase error.(a) $D_{\phi\|}$, corrected phase error structure function. (b) $D_{\phi\|}$, x-x(red) and y-y(blue) transversal cuts. (c) $D_{\phi\ alias}$, aliasing phase error structure function (d) $D_{\phi\ alias}$, x-x(red) and y-y(blue) transversal cuts.

4.6.1. Simulations for high order contributions $\mathcal{C}_{rr}$ and $D_{\phi\perp}$

From a YAO simulation, with D/r$_0$=1, the high order WFS measurements $\mathcal{W}(\phi_\perp)$ are obtained (see section 4.5.1). $D_{\phi\perp}$ is the structure function of $\mathcal{W}(\phi_\perp)$. $\mathcal{C}_{rr}$ is calculated from equation 4.3 using the NICI AO measured command matrix. $\mathcal{C}_{rr}$ and $D_{\phi\perp}$ can be scaled to any D/r$_0$ condition using equations 2.134 and 2.135. It was expected that an open

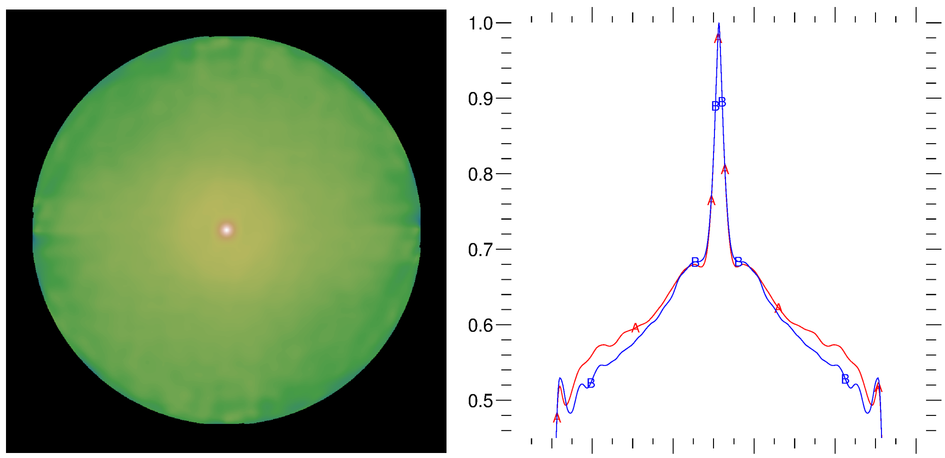

(a) .   (b)

FIGURE 4.14. The turbulent atmosphere OTF. (a) Turbulent atmosphere OTF (b) Turbulent atmosphere OTF, x-x (red) and y-y (blue) transversal cuts.

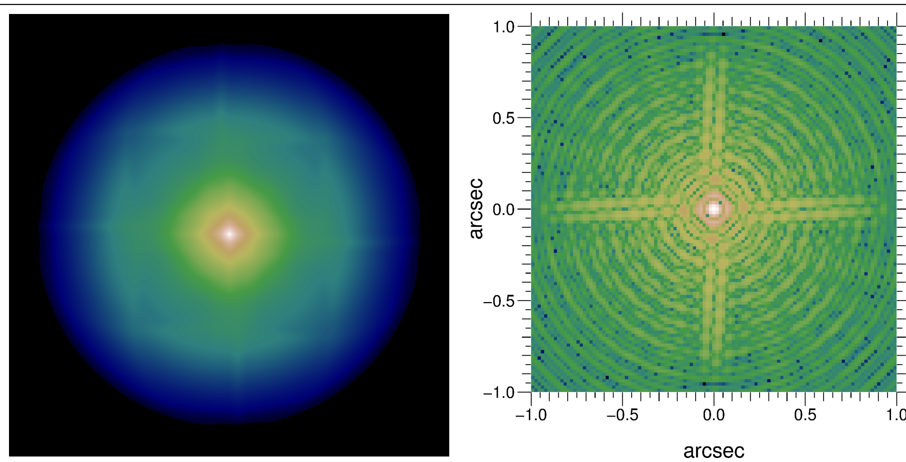

(a)   (b)

FIGURE 4.15. Telescope OTF and PSF. (a) Telescope OTF @ 1.65 [μm]. (b) Telescope PSF @ 1.65 [μm].

loop simulation with high order realizations of the turbulent phase (high-pass filtered phase screens) would provide an appropriate evaluation of $\mathcal{C}_{rr}$ and $D_{\phi\perp}$. However this assumption was not correct. As it was found in section 4.4.4, the high order phase is obtained from a first order high pass filter and due to the filter roll-off, there is a low frequency residual that is affected by the loop gain; making $\mathcal{C}_{rr}$ and $D_{\phi\perp}$ dependent on the loop gain. Therefore,

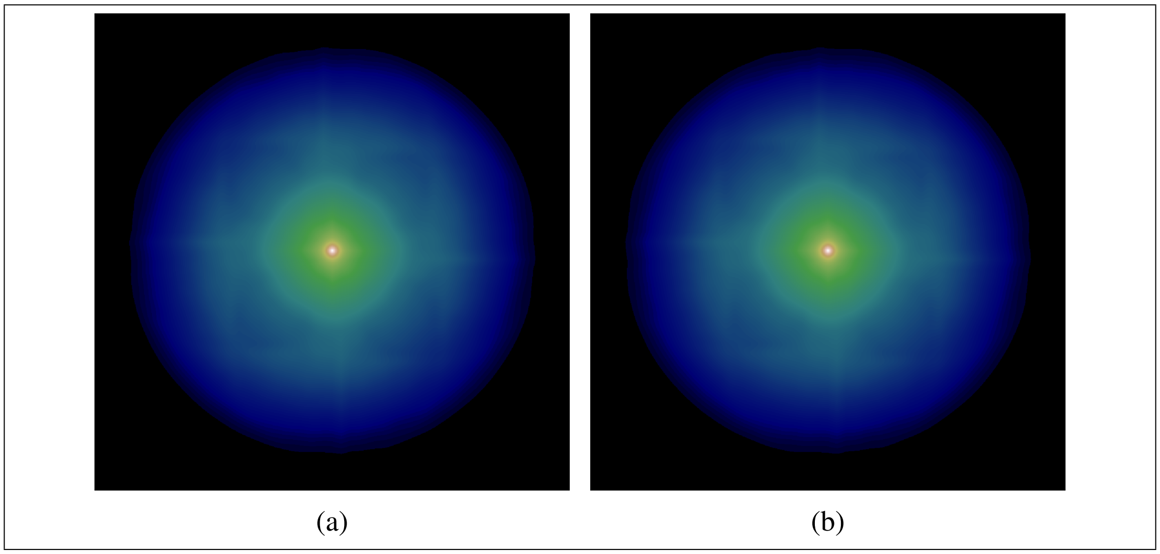

FIGURE 4.16. Simulated long exposure OTF and estimated OTF. (a) Long exposure OTF from simulation. (b) Estimated Long exposure OTF.

for every different loop gain a high order simulation has to be done. Figures 4.17 and 4.18 present $\mathcal{C}_{rr}$ and $D_{\phi\perp}$ as function of the loop gain.

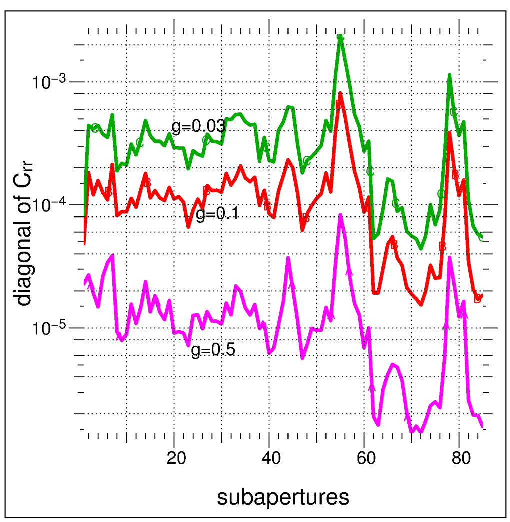

FIGURE 4.17. $\phi_\perp$ variance as function of loop gain (g=0.03 (green), g=0.1 (red) and g=0.5 (magenta).

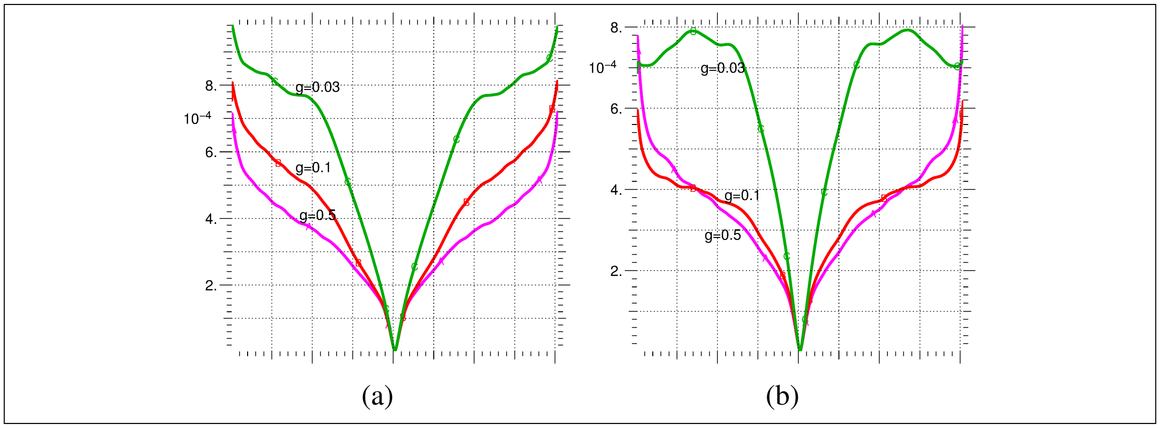

FIGURE 4.18. $D_{\phi\perp}$ as function of the loop gain. (a) x-x cut for $D_{\phi\perp}$ as function of the loop gain g=0.03 (green), g=0.1 (red) and g=0.5 (magenta). (b) y-y cut for $D_{\phi\perp}$ as function of the loop gain g=0.03 (green), g=0.1 (red) and g=0.5 (magenta).

4.6.2. Datasets for PSF reconstruction

The datasets, provided by Gemini Observatory correspond to observations done during the nights of September 15th in 2008 and February 8th in 2009. The datasets have on-sky observations for AO guide stars with the following magnitudes in the R band (680 μm):

- Case 1: R = 8.9
- Case 2: R = 11.0
- Case 3: R = 12.07
- Case 4: R = 13.2

These datasets allow to make two study cases: PSF reconstruction on bright stars (R=8.9 and R=11.0) and PSF reconstruction on faint stars (R=12.07 and R=13.2). It will be also possible to evaluate the effect of the loop gain in the PSF reconstruction accuracy and the effectiveness of the V$_{ii}$ method.

Table 4.1 summarizes the datasets provided for PSF reconstruction on NICI AO, these datasets include on-sky science images and AO circular buffer data.

TABLE 4.1. Summary of NICI observations datasets.

Case	Date	UTC time	Target	Ra/Dec	R Magnitude	Loop Gain
1-a	8-Feb-2009	05:18:15	HD 91845	158.980 /-21.449	8.9	0.1
1-b	8-Feb-2009	05:20:50	HD 91845	158.980 /-21.449	8.9	0.2
1-c	8-Feb-2009	05:22:47	HD 91845	158.980 /-21.449	8.9	0.3
1-d	8-Feb-2009	05:23:53	HD 91845	158.980 /-21.449	8.9	0.34
1-e	8-Feb-2009	05:24:58	HD 91845	158.980 /-21.449	8.9	0.4
1-f	8-Feb-2009	05:26:14	HD 91845	158.980 /-21.449	8.9	0.5
2-a	15-Sept-2008	00:48:48	0703-0708348	285.037/-19.695	11.0	0.5
2-b	15-Sept-2008	00:53:30	0703-0708348	285.037/-19.695	11.0	0.4
2-c	15-Sept-2008	00:58:17	0703-0708348	285.037/-19.695	11.0	0.3
2-d	15-Sept-2008	01:04:08	0703-0708348	285.037/-19.695	11.0	0.2
2-e	15-Sept-2008	01:08:49	0703-0708348	285.037/-19.695	11.0	0.1
3-a	15-Sept-2008	01:24:38	S3033132255	285.395/-20.334	12.07	0.03
3-b	15-Sept-2008	01:35:34	S3033132255	285.395/-20.334	12.07	0.08
3-c	15-Sept-2008	01:46:41	S3033132255	285.395/-20.334	12.07	0.16
3-d	15-Sept-2008	01:51:24	S3033132255	285.395/-20.334	12.07	0.2
4-a	15-Sept-2008	03:32:17	GSC0640000164	345.066/-20.199	13.22	0.01
4-b	15-Sept-2008	03:40:53	GSC0640000164	345.066/-20.199	13.22	0.03
4-c	15-Sept-2008	03:50:39	GSC0640000164	345.066/-20.199	13.22	0.08

4.6.3. Estimation of r_0 from DM commands

The algorithm for the estimation of r_0 using the DM commands, described in section 2.7.4, was implemented in Yorick. The AO circular buffers from the datasets indicated in table 4.1 were processed. NICI WFS measurements are for λ = 0.65 μm, thus the r_0 estimation has to be scaled to obtain the standard r_0 at 0.5 μm using

$$r_{0(0.5\mu m)} = r_{0(0.65\mu m)} \left(\frac{0.50}{0.65}\right)^{1.2} \tag{4.6}$$

Table 4.2 provides a summary with the values estimated for r_0 in centimeters and the seeing angle in arc-seconds.

4.6.4. Analysis of r_0 estimation results

Gemini Observatory has a Differential Image Motion Monitor (DIMM) installed at Cerro Pachon, which is able to estimate r_0 with accuracy of $\sim$10% (Tokovinin and Kornilov (2007). For Case 1, in the night of February 8th 2009 at the time of the observations (around 5:30 UTC), the DIMM measurements recorded r_0 between 16 to 18 centimeters. The DIMM is a separate instrument mounted a few tens of meters away from the Gemini

TABLE 4.2. r_0 estimation from AO circular buffer DM commands.

Case	Date	UTC time	Target	D/r_0 @ 0.65 μm	r_0 @ 0.65 μm	r_0 @ 0.5 μm	seeing [arcsec]
1-a	8-Feb-2009	05:18:15	HD 91845	46.2	17.1	12.5	1.008
1-b	8-Feb-2009	05:20:50	HD 91845	49.1	16.1	11.7	1.071
1-c	8-Feb-2009	05:22:47	HD 91845	51.4	15.4	11.2	1.121
1-d	8-Feb-2009	05:23:53	HD 91845	46.9	16.8	12.3	0.993
1-e	8-Feb-2009	05:24:58	HD 91845	56.8	13.9	10.2	1.239
1-f	8-Feb-2009	05:26:14	HD 91845	52.4	15.1	11.0	1.143
2-a	15-Sept-2008	00:48:48	0703-0708348	59.6	13.2	9.7	1.301
2-b	15-Sept-2008	00:53:30	0703-0708348	55.9	14.1	10.3	1.219
2-c	15-Sept-2008	00:58:17	0703-0708348	67.2	11.7	8.6	1.467
2-d	15-Sept-2008	01:04:08	0703-0708348	54.9	14.4	10.5	1.198
2-e	15-Sept-2008	01:08:49	0703-0708348	51.0	15.5	11.3	1.114
3-a	15-Sept-2008	01:24:38	S3033132255	38.5	20.5	14.9	0.841
3-b	15-Sept-2008	01:35:34	S3033132255	39.7	19.9	14.5	0.867
3-c	15-Sept-2008	01:46:41	S3033132255	40.6	19.5	14.2	0.886
3-d	15-Sept-2008	01:51:24	S3033132255	44.7	17.7	12.9	0.976
4-a	15-Sept-2008	03:32:17	GSC0640000164	39.2	20.2	14.7	0.855
4-b	15-Sept-2008	03:40:53	GSC0640000164	26.5	29.8	21.7	0.579
4-c	15-Sept-2008	03:50:39	GSC0640000164	39.3	20.1	14.7	0.858

dome, and it is usually looking in a different direction than Gemini. Therefore, the DIMM measurements can be used only as a reference to compare the estimated r_0 values from the AO DM commands, but not to evaluate the accuracy of the estimation from the DM commands. In addition, the DIMM seeing measured values tend to be 20-30% higher than the values delivered by the Gemini Image Quality software and it doesn't account for the dome turbulence either.

Figure 4.19 shows a graph of the r_0 estimation for Case 1, which corresponds to the night of February 8th 2009. Dashed regions show the range for DIMM seeing measurement values (red) and an estimated Gemini Image Quality measurement (magenta), assuming they are 20% lower than DIMM measurements. The estimations of r_0 obtained from the DM commands are represented by the blue line and diamond markers. It can be seen that the estimated values for r_0 are ($\sim$ 30%) lower than the DIMM measurements,this difference could be explained by i) It is possible that the DIMM did not exactly see the same portion of atmosphere than the telescope and ii) the DIMM does not account for the dome seeing that can reduce the seeing in the observation between 20% and 30% (Connors, 2008). iii)

The turbulence outer scale is different to the outer scale used in the simulation of the high order contributions.

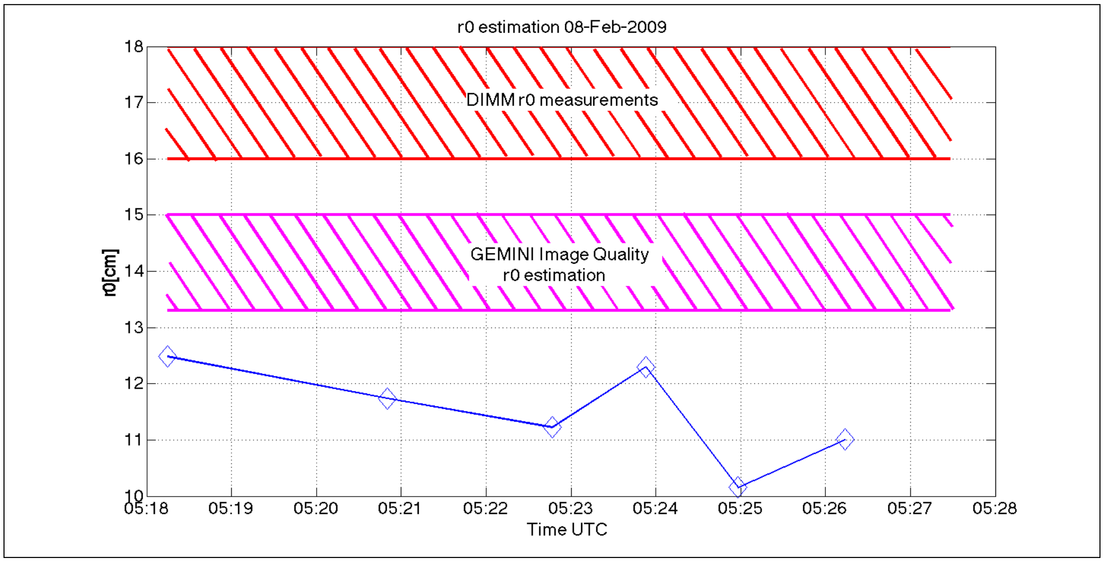

FIGURE 4.19. Case 1: r_0 estimation (blue line) comparison with DIMM measurements on 08-Feb-2009.

For the rest of the datasets corresponding to cases 2, 3 and 4; that were acquired during the night of September 15th 2008, the DIMM was out of service, thus there are not measurements available to compare with the estimations. Figure 4.20 shows a graph with the estimations of r_0 for the aforementioned cases.

Figure 4.21 shows the r_0 estimation as function of the AO loop gain and the AO star magnitude. It can be seen that the estimation of r_0 tends to be higher for lower loop gains and for higher star magnitude (fainter star). This behaviour is explained by equation 2.138, that tell us that r_0 will be higher if $\mathcal{C}_{rr}$ or σ_n^2 are higher or if the covariance of the mirror commands is lower.

In section 4.6.1, it is shown that $\mathcal{C}_{rr}$ tends to be higher for lower AO loop gains, setting the dependence of the r_0 estimation in the loop gain. The dependence on the star magnitude comes from the fact that for fainter stars the photon noise will be higher in the WFS measurements. Figure 4.22 illustrates this situation, where the WFS measurement noise variance corresponds to cases 1, 2 and 3 for a loop gain of 0.2. This relationship may seem

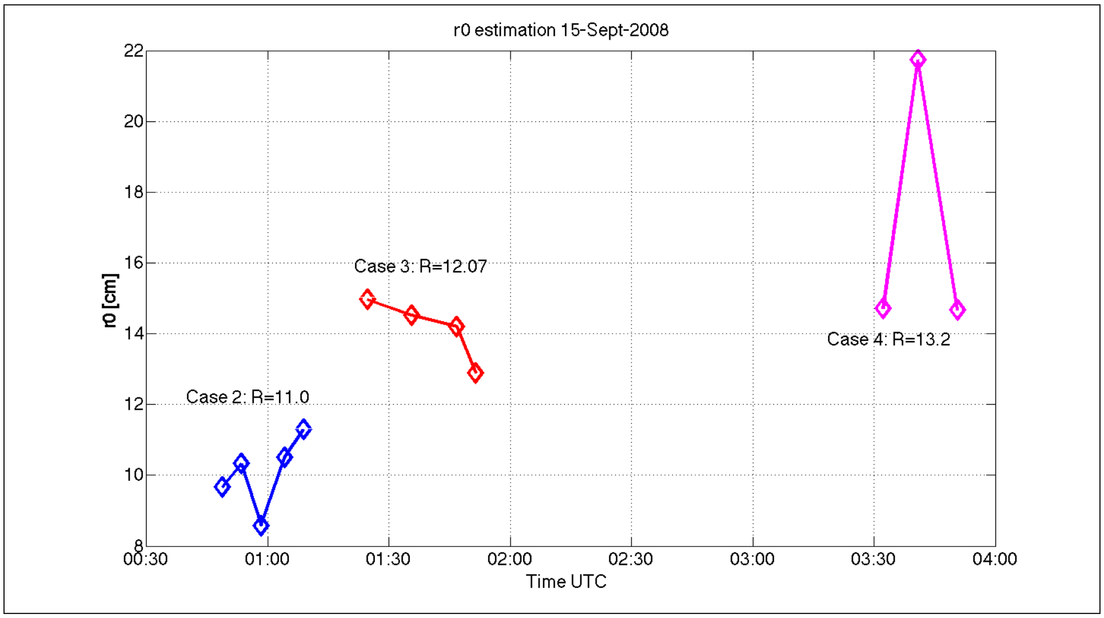

FIGURE 4.20. r_0 estimation for cases 2(blue), 3(red) and 4(magenta) on 14-Sep-2008.

contradictory for case 1 that has a higher r_0 estimation than case 2, but it is necessary to recall that case 1 was observed during the summer (February 2009) and case 2 was observed during the spring (September 2008), thus case 1 could be expected to have better seeing due to the better weather conditions in the summer.

The higher photon noise in faint stars forces to reduce the system bandwidth, this reduction is done by lowering the AO loop gain. As consequence of the lower loop gain, $\sigma^2_{m_i}$ is lowered and $\sigma^2_{r_i}$ is augmented (see figure 4.17). $\sigma^2_{a_i}$ in equation 2.138 is lowered and the D/r_0 estimation in equation 2.136 is lowered too. If $\sigma^2_{a_i}$ gets too close to 0, the estimation of r_0 will produce higher values (over-estimation) or the estimation algorithm will not converge. For PSF-R, an over-estimated value of r_0 will deliver an estimated PSF with a significative higher strehl with respect to the real long exposure PSF.

Finally, it will be possible to evaluate the accuracy of the r_0 estimation method by comparison of the strehl values for the PSF estimation and the real long exposure PSF.

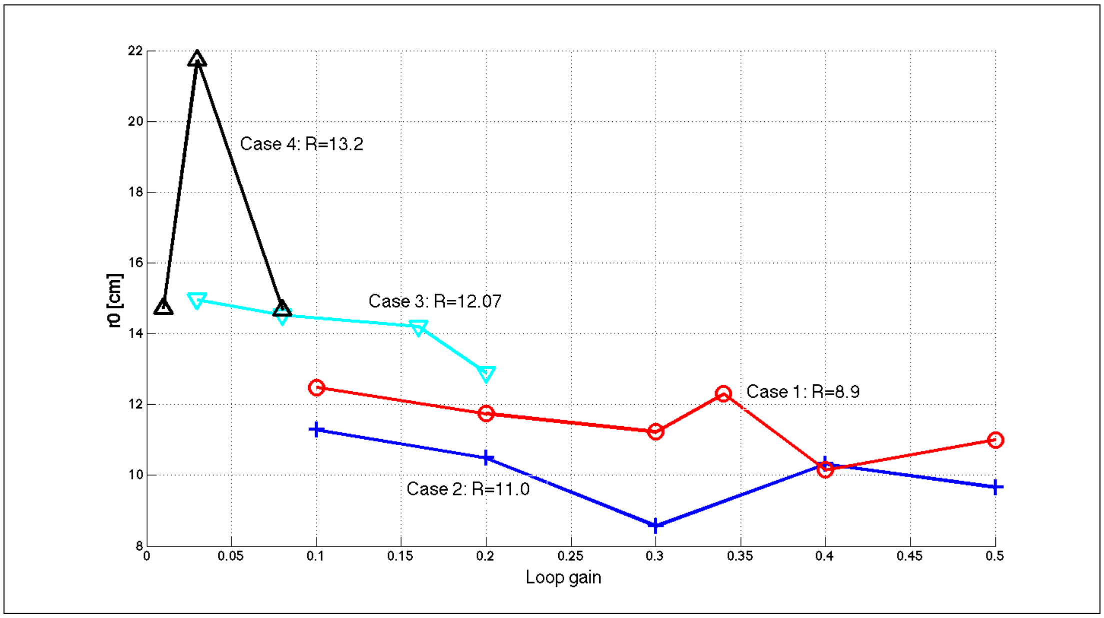

FIGURE 4.21. r_0 estimation as function of the loop gain and the AO star magnitude

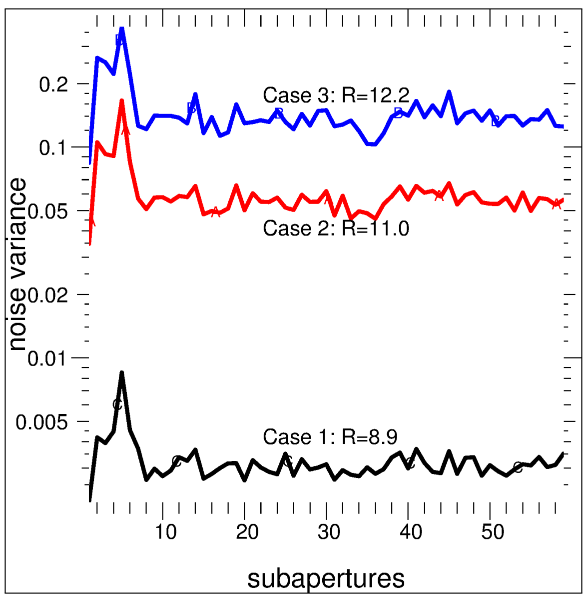

FIGURE 4.22. WFS measurement noise variance as function of AO star magnitude(log scale). R=8.9 (black), R=11.0(red), R=12.2 (blue).

4.6.5. PSF reconstruction results

The datasets listed in table 4.1 were processed using APETy and the values of r_0 estimated from the DM commands that are summarized in table 4.2. The PSF estimation was done using both U_{ij} and V_{ii} methods. To evaluate the quality of the estimation, the real PSF and the estimated PSF are compared in terms of the Strehl ratio, the FWHM and the diameter of the 50% encircled energy (EE50). Table 4.3 presents the results of the PSF estimation for the datasets processed.

TABLE 4.3. PSF reconstruction results for NICI datasets.

			Strehl Ratio %			FWHM [arcsec]			EE50 [arcsec]		
Case	R Magnitude	Loop Gain	Real	U_{ij}	V_{ii}	Real	U_{ij}	V_{ii}	Real	U_{ij}	V_{ii}
1-a	8.9	0.1	0.310	0.240	0.240	0.067	0.080	0.080	0.187	0.187	0.187
1-b	8.9	0.2	0.325	0.258	0.258	0.063	0.075	0.075	0.221	0.187	0.187
1-c	8.9	0.3	0.321	0.248	0.248	0.062	0.074	0.074	0.187	0.221	0.221
1-d	8.9	0.34	0.318	0.294	0.294	0.058	0.070	0.070	0.204	0.170	0.170
1-e	8.9	0.4	0.302	0.197	0.197	0.058	0.081	0.081	0.221	0.255	0.255
1-f	8.9	0.5	0.307	0.228	0.228	0.069	0.0786	0.079	0.204	0.204	0.204
2-a	11.0	0.5	0.076	0.141	0.141	0.241	0.102	0.102	0.306	0.272	0.272
2-b	11.0	0.4	0.095	0.174	0.174	0.195	0.093	0.093	0.289	0.238	0.238
2-c	11.0	0.3	0.121	0.119	0.119	0.122	0.097	0.097	0.323	0.340	0.340
2-d	11.0	0.2	0.150	0.190	0.190	0.109	0.087	0.087	0.306	0.238	0.238
2-e	11.0	0.1	0.173	0.191	0.191	0.083	0.087	0.087	0.306	0.221	0.221
3-a	12.07	0.03	0.099	0.162	0.161	0.084	0.100	0.099	0.578	0.204	0.204
3-b	12.07	0.08	0.104	0.271	0.270	0.104	0.080	0.080	0.544	0.136	0.136
3-c	12.07	0.16	0.087	0.300	0.299	0.135	0.078	0.078	0.527	0.136	0.136
3-d	12.07	0.2	0.073	0.257	0.256	0.148	0.084	0.084	0.493	0.170	0.170
4-a	13.22	0.01	0.061	0.115	0.115	0.111	0.183	0.182	0.816	0.204	0.204
4-b	13.22	0.03	0.072	0.329	0.328	0.089	0.075	0.075	0.816	0.136	0.136
4-c	13.22	0.08	0.065	0.278	0.277	0.116	0.079	0.079	0.799	0.136	0.136

4.6.5.1. PSF reconstruction performance

Table 4.4 summarizes the best results obtained for each of the observed magnitudes. As the datasets were acquired during a gain characterization study, the observations were not done with the AO loop in the optimal setup that minimized the phase error, which is a key assumption for the PSF reconstruction algorithm.

For bright stars, the difference in the Strehl ratio between the estimated PSF and the sky PSF is less than 7.5%, which is close to the accuracy obtained by Véran et al. (1997) and Jolissaint et al. (2012). For faint stars, the deviation between the real PSF and the estimated PSF is significative and the best estimation occurs for loop gains close to open loop condition. This is mainly because the noise becomes a dominant factor in the WFS measurement.

TABLE 4.4. PSF reconstruction performance.

R Magnitude	Loop Gain		Real PSF	Estimated PSF
		Strehl Ratio (%)	31.79	29.41
8.9	0.34	FWHM (mili-arcsec)	57.91	70.25
		Encircled Energy 50% (mili-arcsec)	203.97	170.0
		Strehl Ratio (%)	12.12	11.89
11.0	0.3	FWHM (mili-arcsec)	122.33	97.04
		Encircled Energy 50% (mili-arcsec)	322.95	339.94
		Strehl Ratio (%)	9.94	16.16
12.07	0.03	FWHM (mili-arcsec)	83.95	99.50
		Encircled Energy 50% (mili-arcsec)	577.90	203.97
		Strehl Ratio (%)	6.14	11.48
13.22	0.01	FWHM (mili-arcsec)	110.057	182.85
		Encircled Energy 50% (mili-arcsec)	815.86	203.97

4.6.5.2. PSF reconstruction for brigth stars: R=8.9 and R=11.0

Figures 4.23 and 4.24 show a cross section comparison of the sky PSF and the estimated PSF. It can be appreciated that the halo slope is well approximated and the maximum error is close to the first lobe of the diffraction limited PSF.

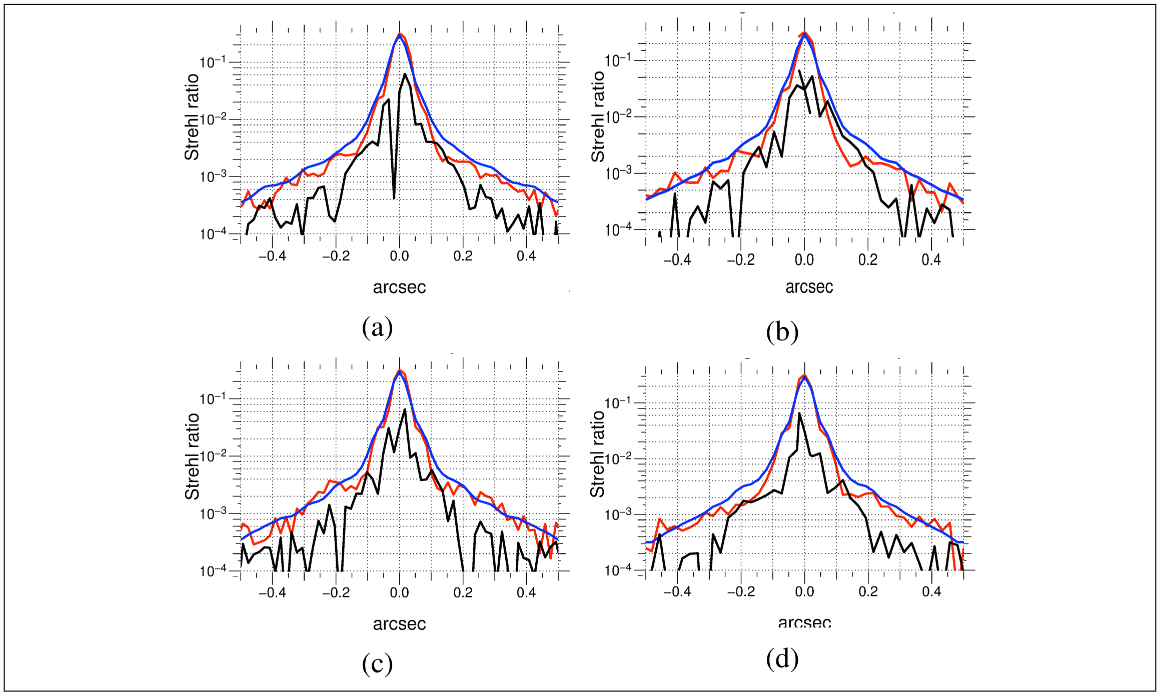

FIGURE 4.23. PSF reconstruction for star of magnitude R=8.9: Cross section comparison between sky PSF (red), estimated PSF (blue) and estimation error (black). (a) y-y cut. (b) 45-225 degress cut. (c) x-x cut. (d) 135-315 degrees cut.

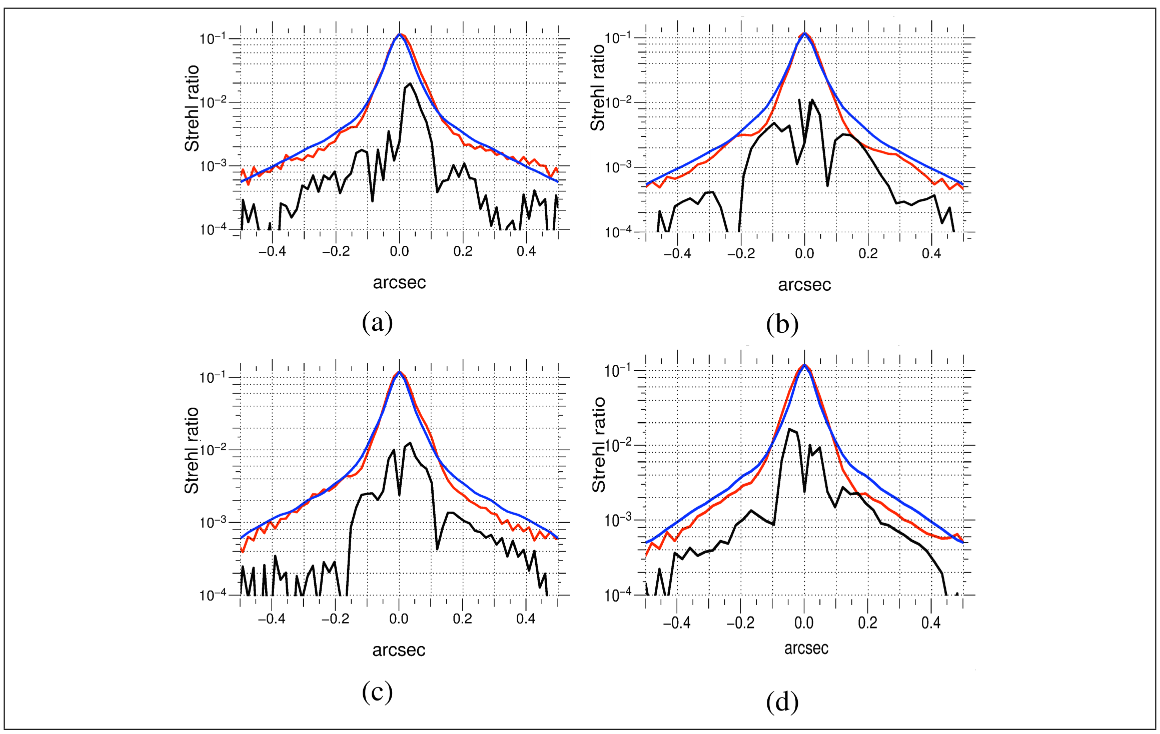

FIGURE 4.24. PSF reconstruction for star of magnitude R=11.0: Cross section comparison between sky PSF (red), estimated PSF (blue) and estimation error (black). (a) y-y cut. (b) 45-225 degress cut. (c) x-x cut. (d) 135-315 degrees cut.

In figures 4.25 and 4.26, the image of the sky PSF and the estimated PSF are shown. It can be seen that the estimated PSF reproduces the sky PSF shape and the halo, however there are some residual speckles that are not properly reproduced. This difference might be due to non-common path aberrations that are not included in this study or due to the presence of a local turbulence in the telescope. The encircled energy has a good agreement for the first 50% of the energy and the difference in the remaining 50 % is mainly due to the noise in the sky PSF image that is more significative for those pixels away from the center.

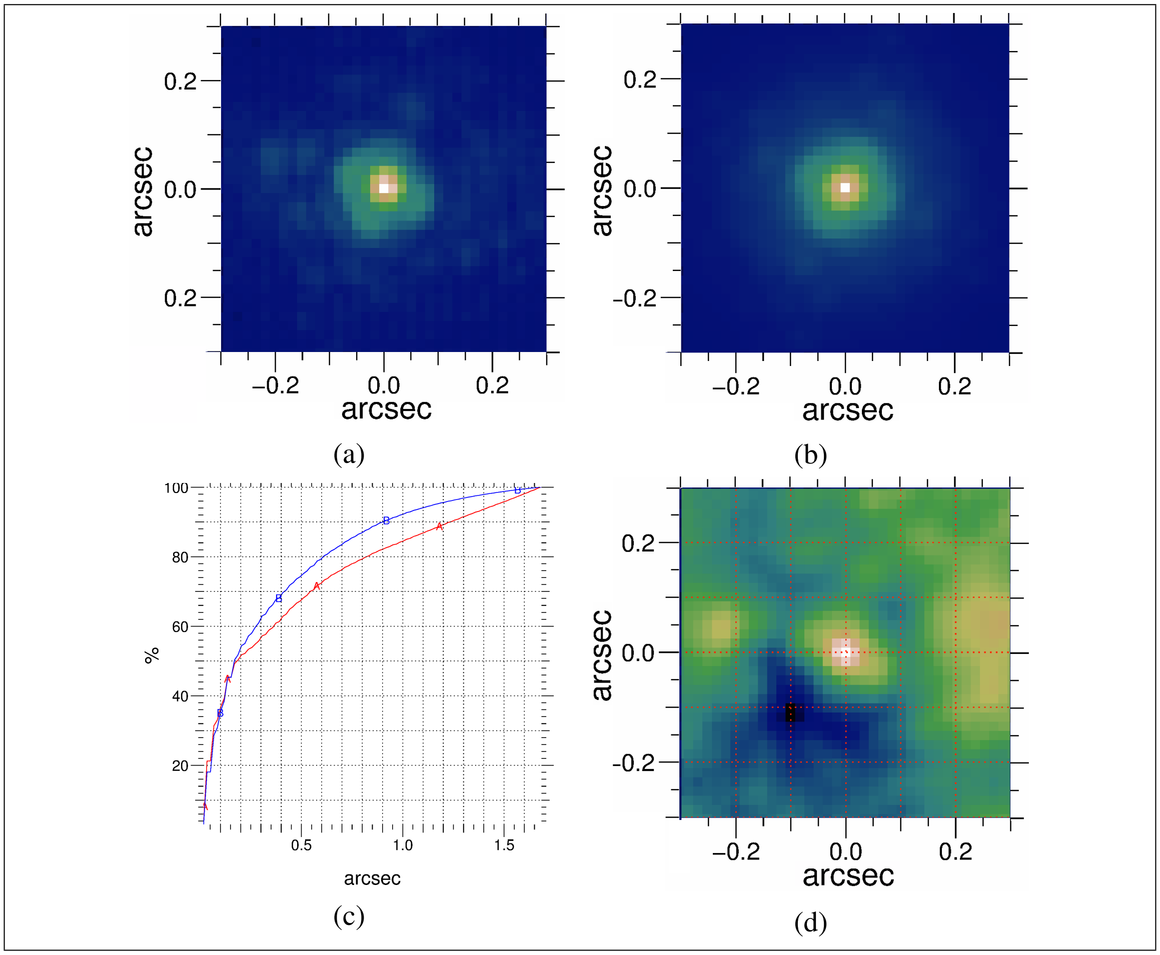

FIGURE 4.25. PSF reconstruction for star of magnitude R=8.9. (a) Science image - Sky PSF. (b) Estimated PSF. (c) Encircled energy comparison: Sky PSF (red), estimated PSF(blue). (d) Deconvolution between sky PSF and estimated PSF.

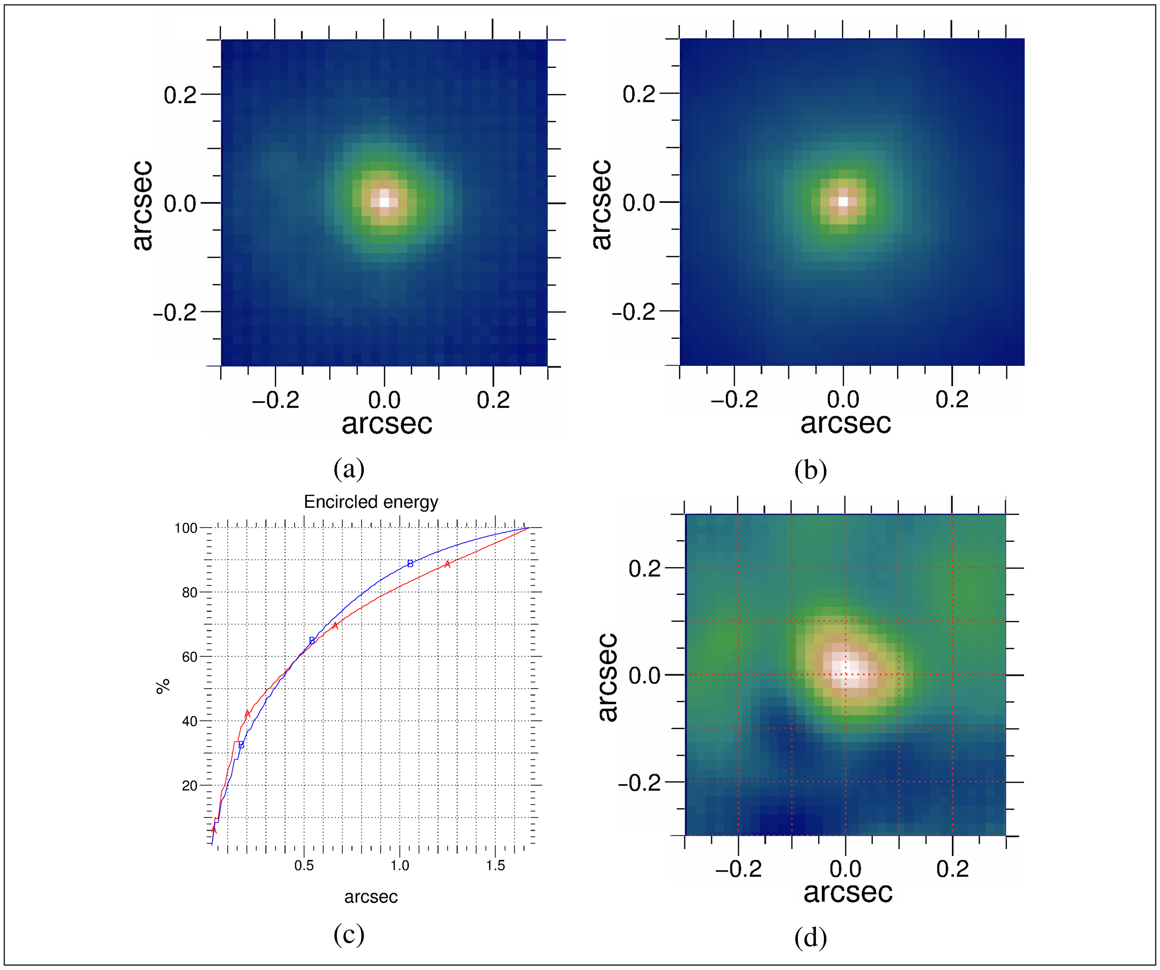

FIGURE 4.26. PSF reconstruction for star of magnitude R=11.0. (a) Science image - Sky PSF. (b) Estimated PSF. (c) Encircled energy comparison: Sky PSF (red), estimated PSF(blue). (d) Deconvolution between sky PSF and estimated PSF.

To deconvolve the sky PSF with the estimated PSF, the Lucy-Richardson algorithm is used. The deconvolution of the sky PSF and the estimated PSF provides the diffraction limited image of the object. The companions present around the image center correspond to the speckles not reproduced by the PSF estimation.

Figures 4.27 and 4.28, display cross section plots of the deconvolved image. Table 4.5 shows the FWHM of the deconvolved images compared to the telescope diffraction limited FWHM.

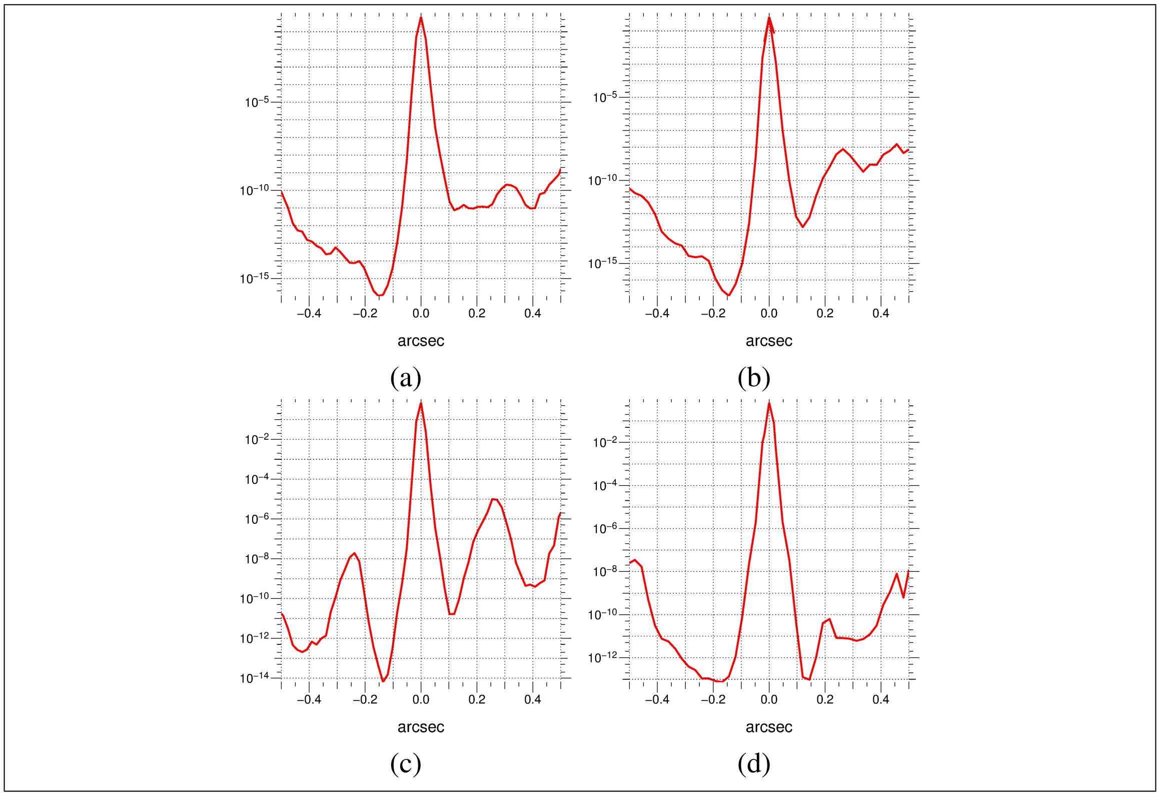

FIGURE 4.27. PSF reconstruction for a star of magnitude R=8.9: Cross sections of devonvolved image. (a) y-y cut. (b) 45-225 degress cut. (c) x-x cut. (d) 135-315 degrees cut.

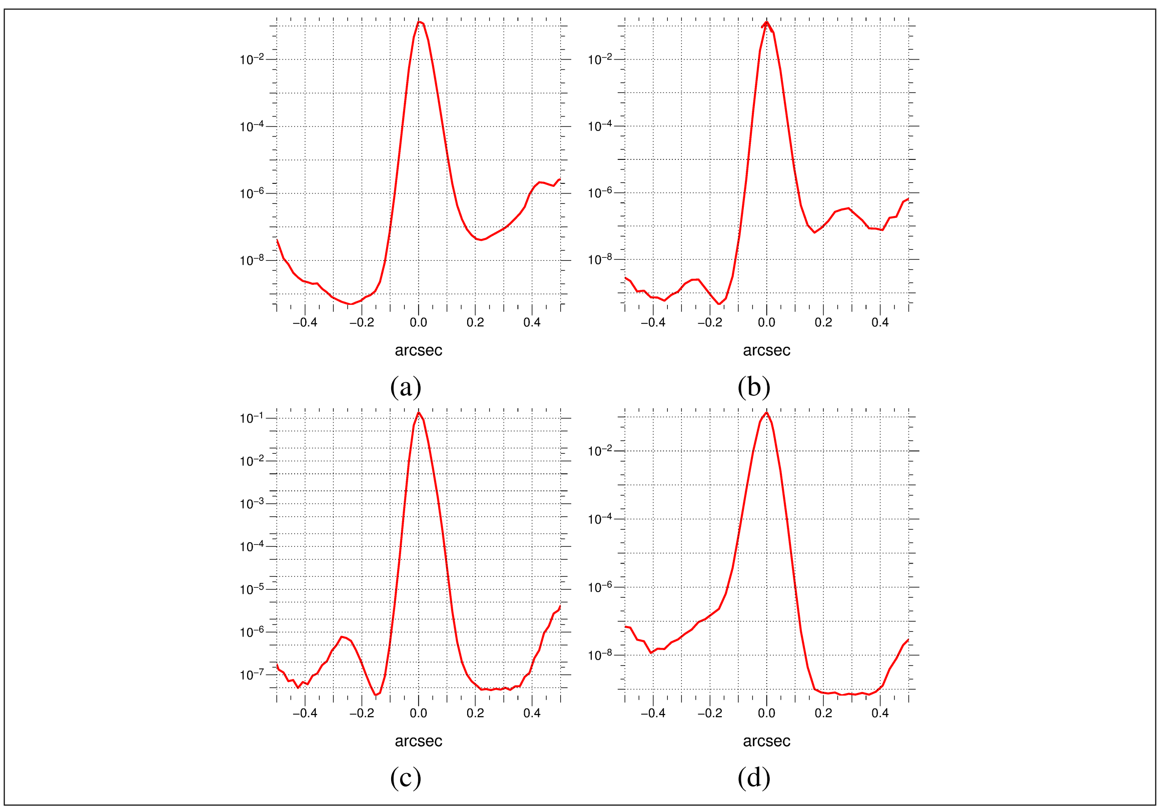

FIGURE 4.28. PSF reconstruction for star of magnitude R=11.0: Cross sections of devonvolved image. (a) y-y cut. (b) 45-225 degress cut. (c) x-x cut. (d) 135-315 degrees cut.

TABLE 4.5. FWHM for deconvolved images.

	Telescope [mili-arcsec]	Magnitude R=8.9 [mili-arcsec]	Magnitude R=11.0 [mili-arcsec]
FWHM	42.22	26.54	43.20

4.6.5.3. PSF reconstruction for faint stars: R=12.07 and R=13.22

For faint objects, the error in the estimations are significantly higher due to the dominance of the noise in the WFS measurement of the phase error. As explained in section 4.6.4, the impact of the noise is felt in the seeing estimation that will provide over-estimated values for both the noise and the low loop gain. Figures 4.29 and 4.30 show cross section comparison plots for the sky PSF and the estimated PSF. It can be seen that the estimation error is higher at the center of the image.

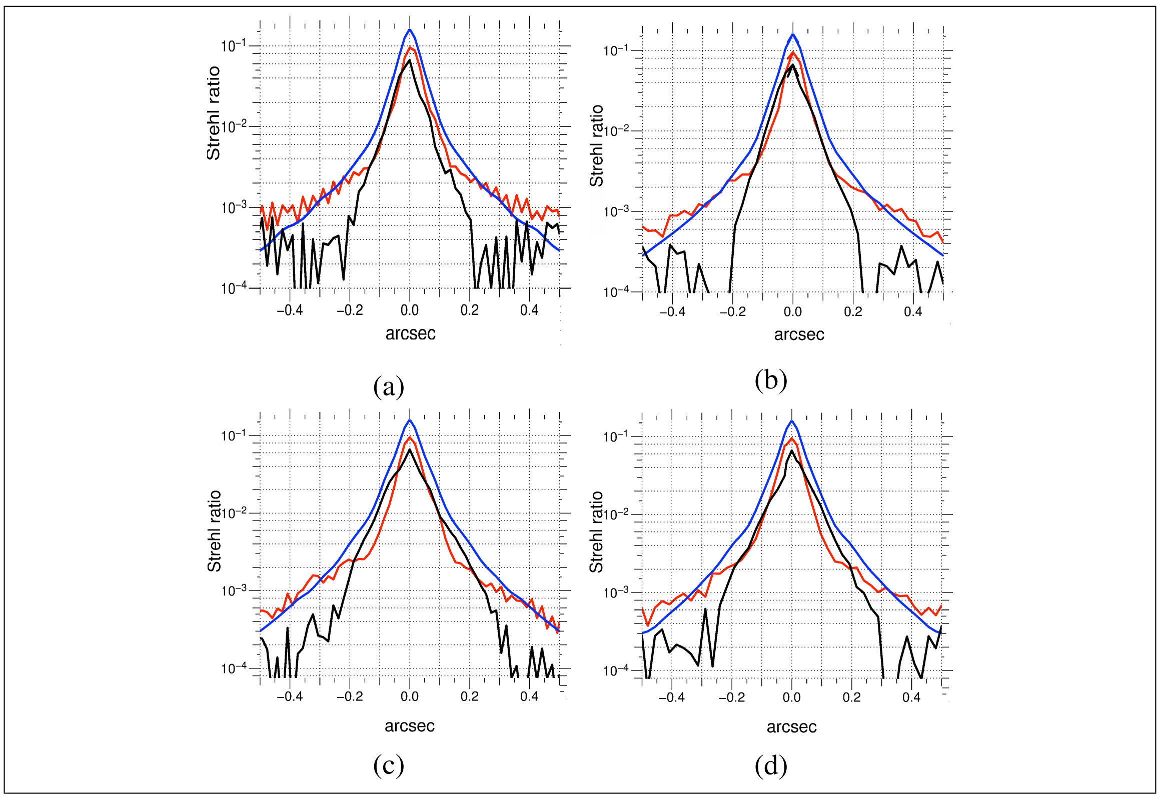

FIGURE 4.29. PSF reconstruction for star of magnitude R=12.07: Cross section comparison between sky PSF (red), estimated PSF (blue) and estimation error (black). (a) y-y cut. (b) 45-225 degress cut. (c) x-x cut. (d) 135-315 degrees cut.

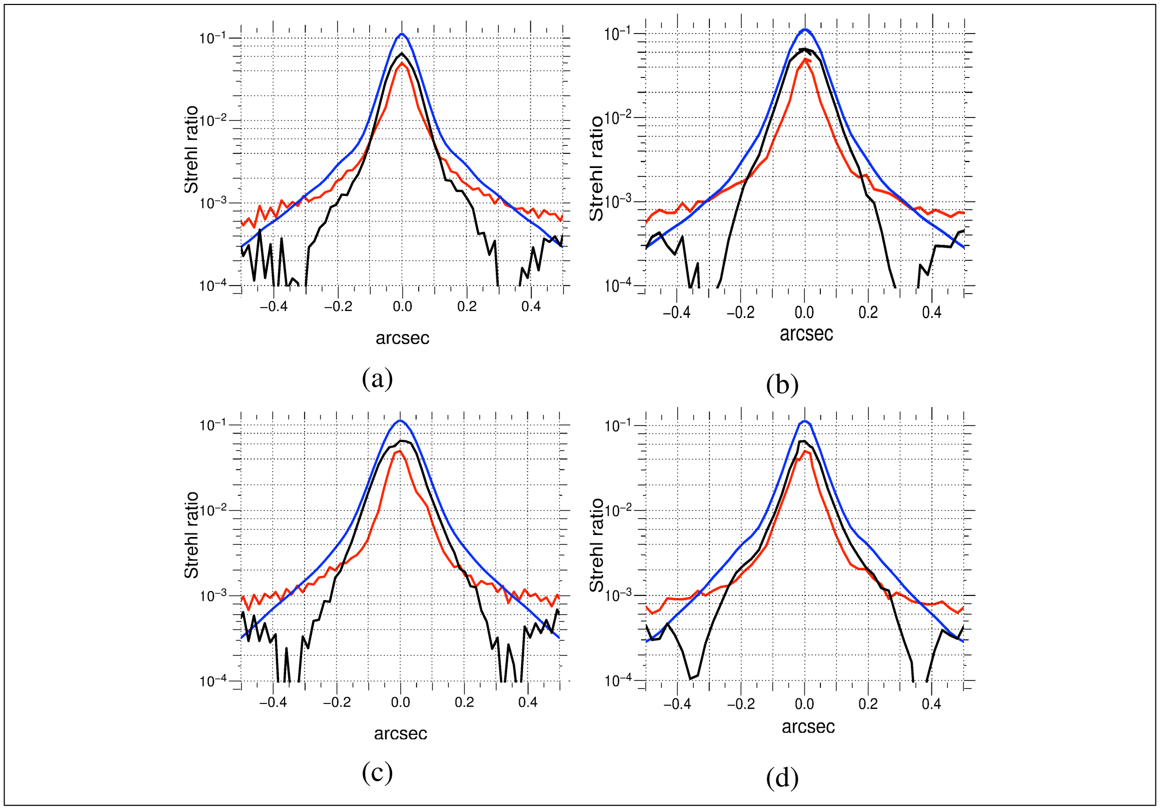

FIGURE 4.30. PSF reconstruction for star of magnitude R=13.22: Cross section comparison between sky PSF (red), estimated PSF (blue) and estimation error (black). (a) y-y cut. (b) 45-225 degress cut. (c) x-x cut. (d) 135-315 degrees cut.

In figures 4.31 and 4.32 is appreciated that the PSF shape is not reproduced. The image of the deconvolved object is surrounded by a noisy halo.

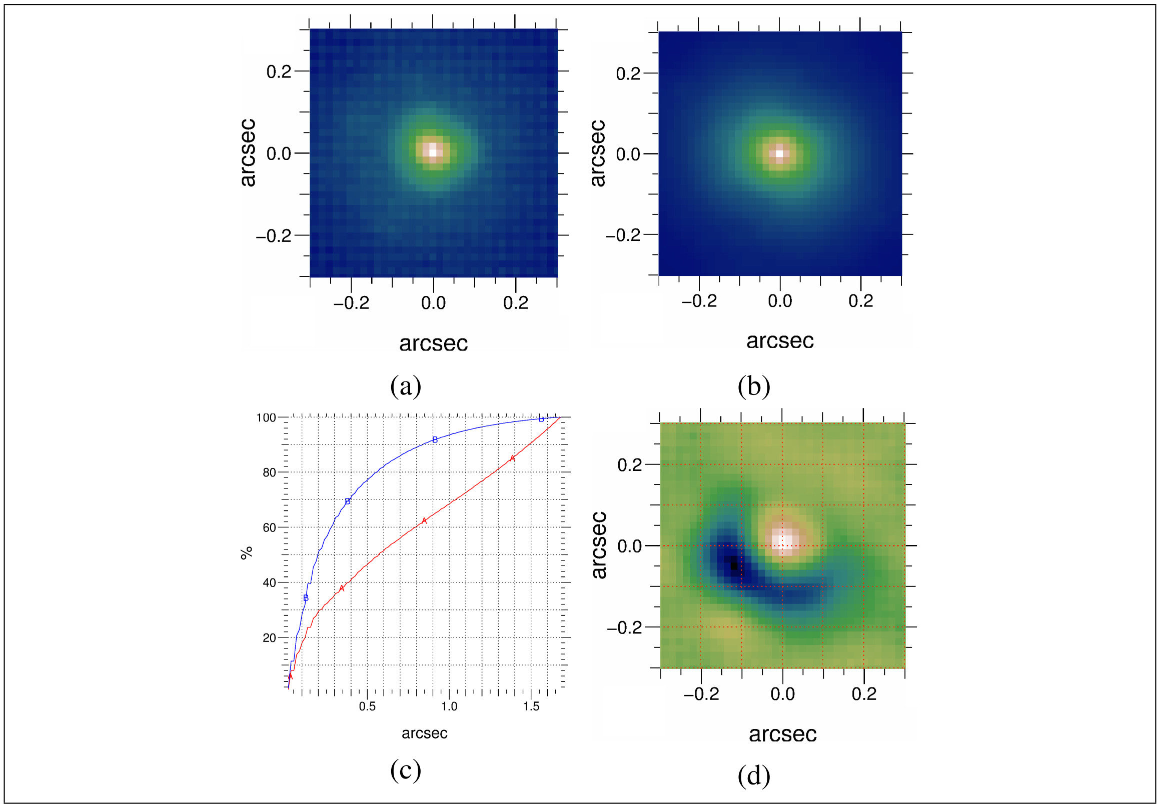

FIGURE 4.31. PSF reconstruction for star of magnitude R=12.07. (a) Science image - Sky PSF (b) Estimated PSF. (c) Encircled energy comparison: Sky PSF (red), estimated PSF(blue). (d) Deconvolution between sky PSF and estimated PSF.

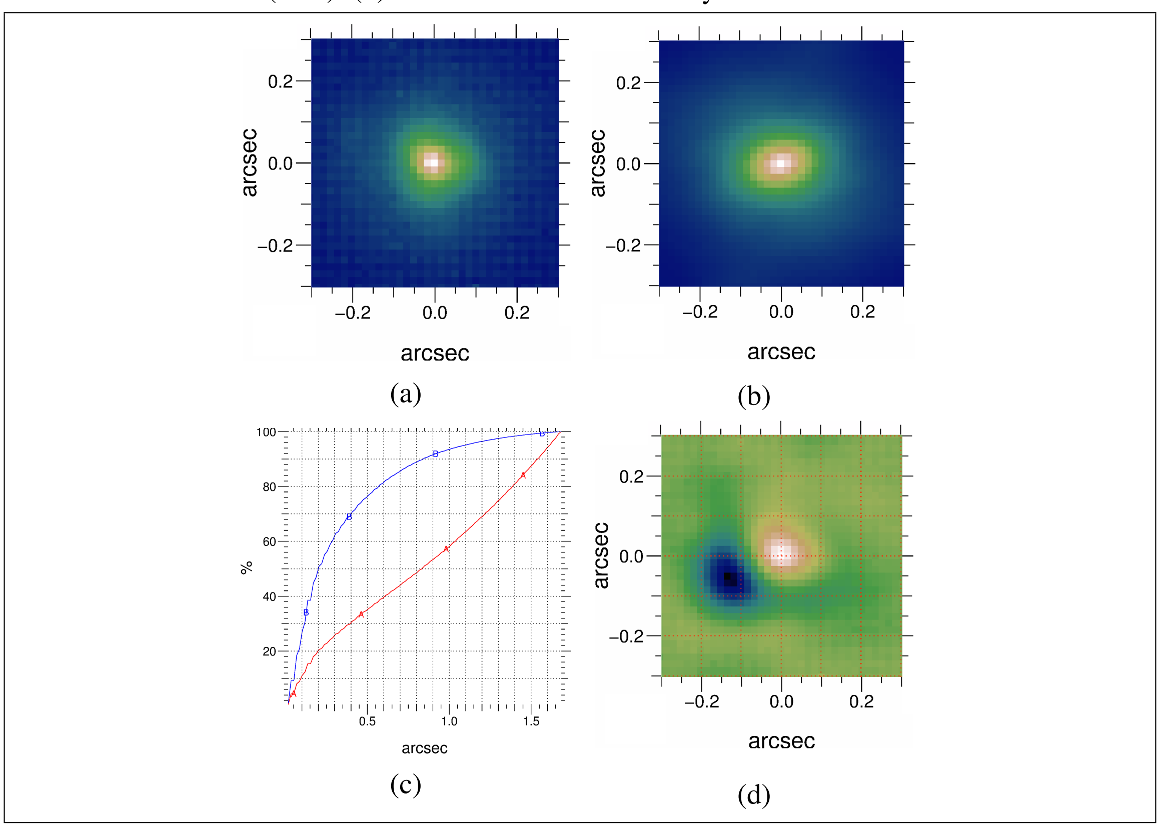

FIGURE 4.32. PSF reconstruction for star of magnitude R=13.22. (a) Science image - Sky PSF. (b) Estimated PSF. (c) Encircled energy comparison: Sky PSF (red), estimated PSF(blue). (d) Deconvolution between sky PSF and estimated PSF.

Figures 4.33 and 4.34 show the cross sections of the deconvolved images and table 4.6 summarizes the FWHM for the deconvolved objects. It can be seen that for R=13.22, the FWHM is higher than the telescope FWHM.

It is possible that the sensitive errors in the PSF estimation are also due to non-common path aberrations and failures in the data acquisition.

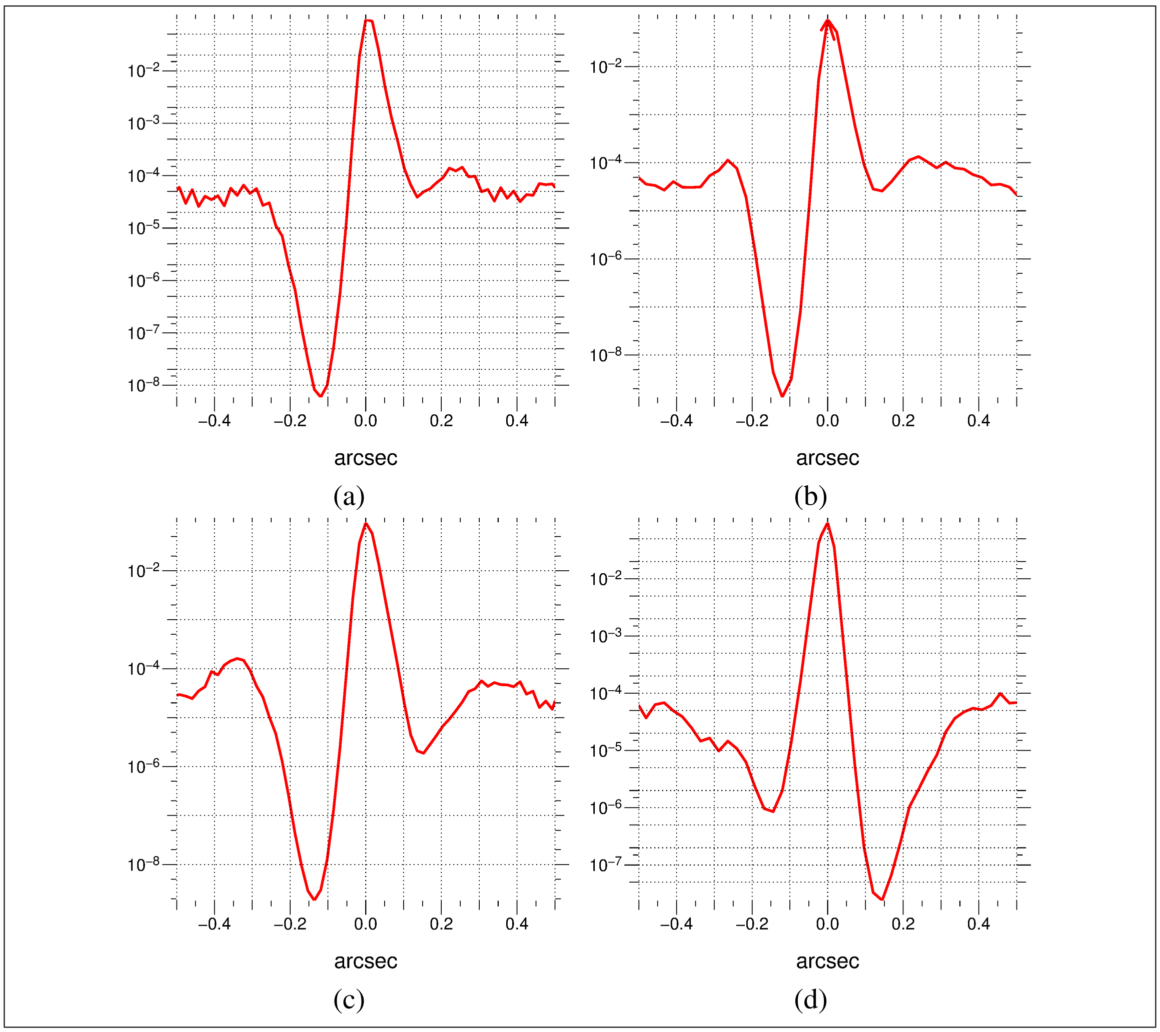

FIGURE 4.33. PSF reconstruction for star of magnitude R=12.07: Cross sections of devonvolved image. (a) y-y cut. (b) 45-225 degress cut. (c) x-x cut. (d) 135-315 degrees cut.

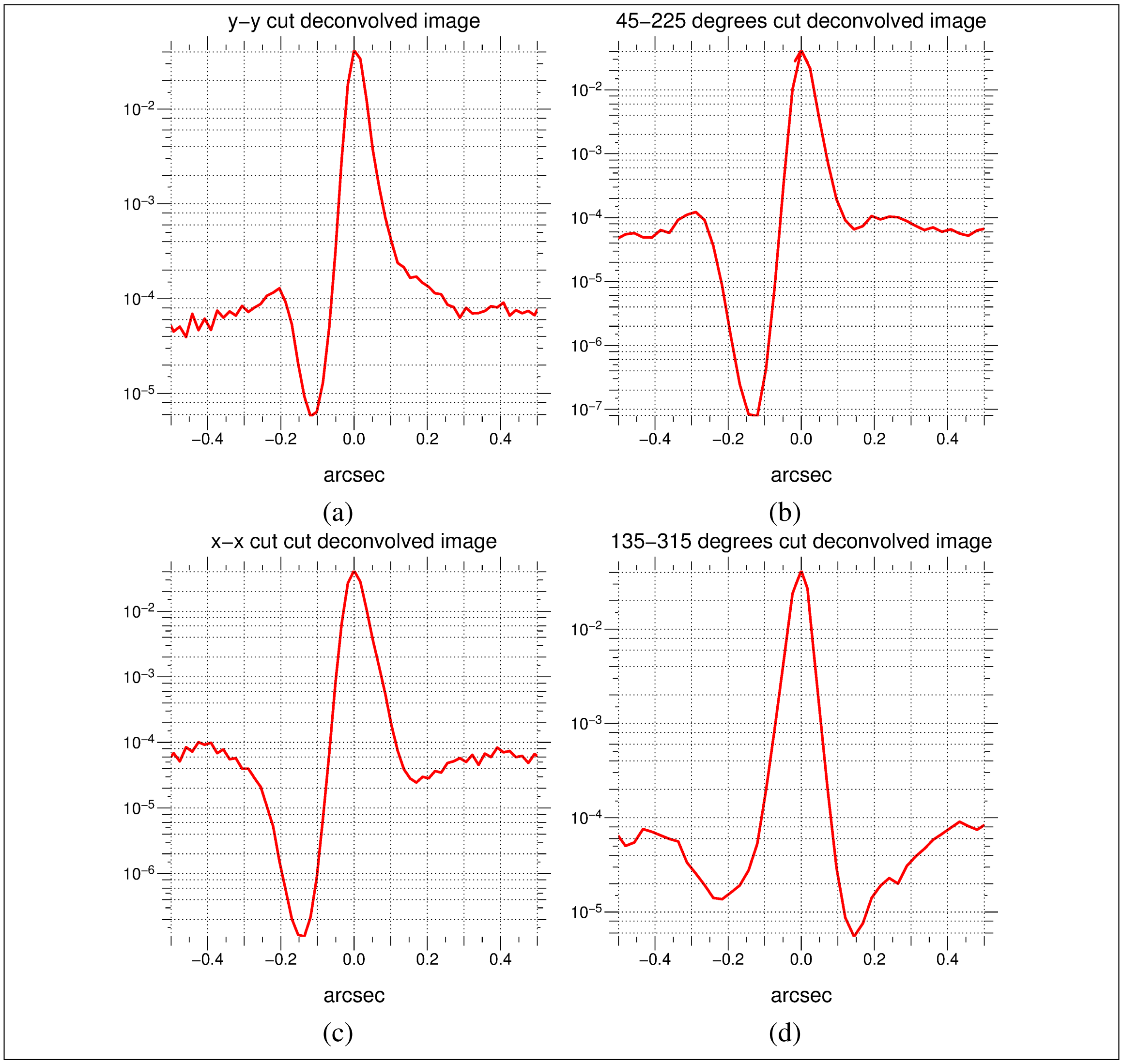

FIGURE 4.34. PSF reconstruction for star of magnitude R=13.22: Cross sections of devonvolved image. (a) y-y cut. (b) 45-225 degress cut. (c) x-x cut. (d) 135-315 degrees cut.

TABLE 4.6. FWHM for deconvolved images.

	Telescope [mili-arcsec]	Magnitude R=12.07 [mili-arcsec]	Magnitude R=13.22 [mili-arcsec]
FWHM	42.22	41.00	50.72

4.6.6. Effect of the AO loop gain in the PSF estimation

Figure 4.35 shows the sky PSF Strehl and the estimated PSF Strehl as function of the loop gain. It can be seen that for bright stars, there is an optimal gain where the PSF estimation converges with the sky PSF. On figure 4.36, the estimation of r_0 was added to the graph, showing that the Strehl of the PSF estimation has a strong dependence on the estimated value of r_0. Knowing that the estimation of r_0 has also a dependence on the loop gain, it might be possible to compensate the estimation of r_0 according to the loop gain.

In the case of faint stars, as shown by Jolissaint et al. (2012), it is necessary to adjust the AO loop gain and AO loop frequency to reach a PSF estimation in good agreement with the sky PSF. The datasets consider only the nominal loop frequency of 1300 Hz, thus proper fitting for faint stars is not possible.

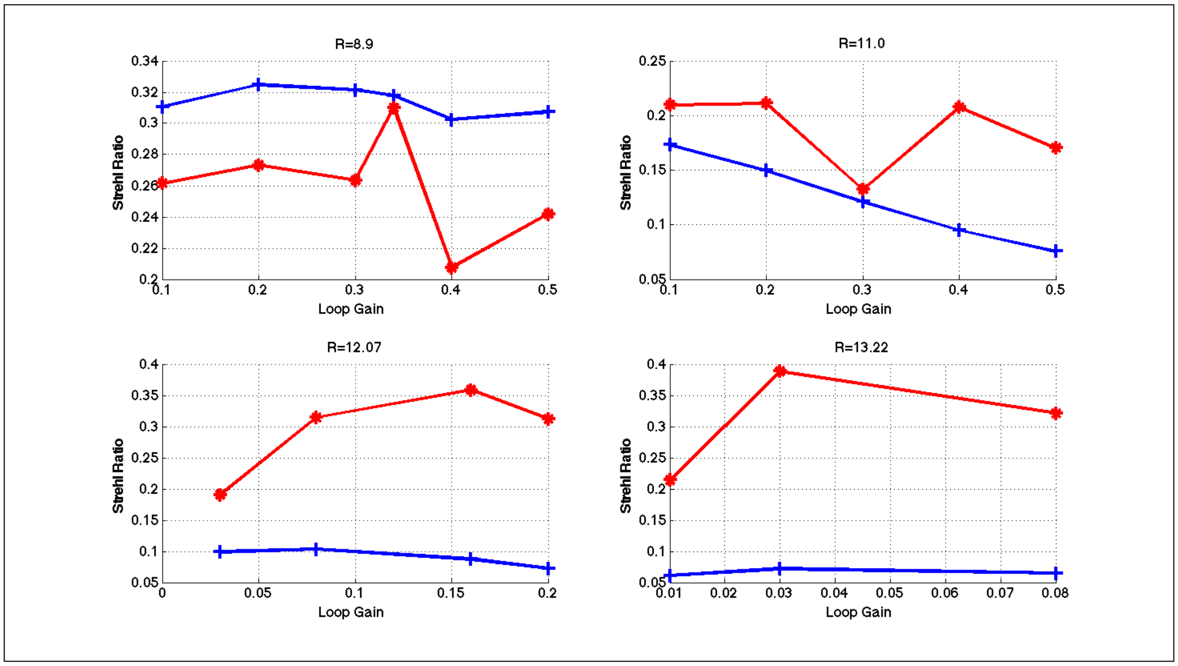

FIGURE 4.35. Sky PSF Strehl (blue) and estimated PSF strehl(red) as function of the loop gain.

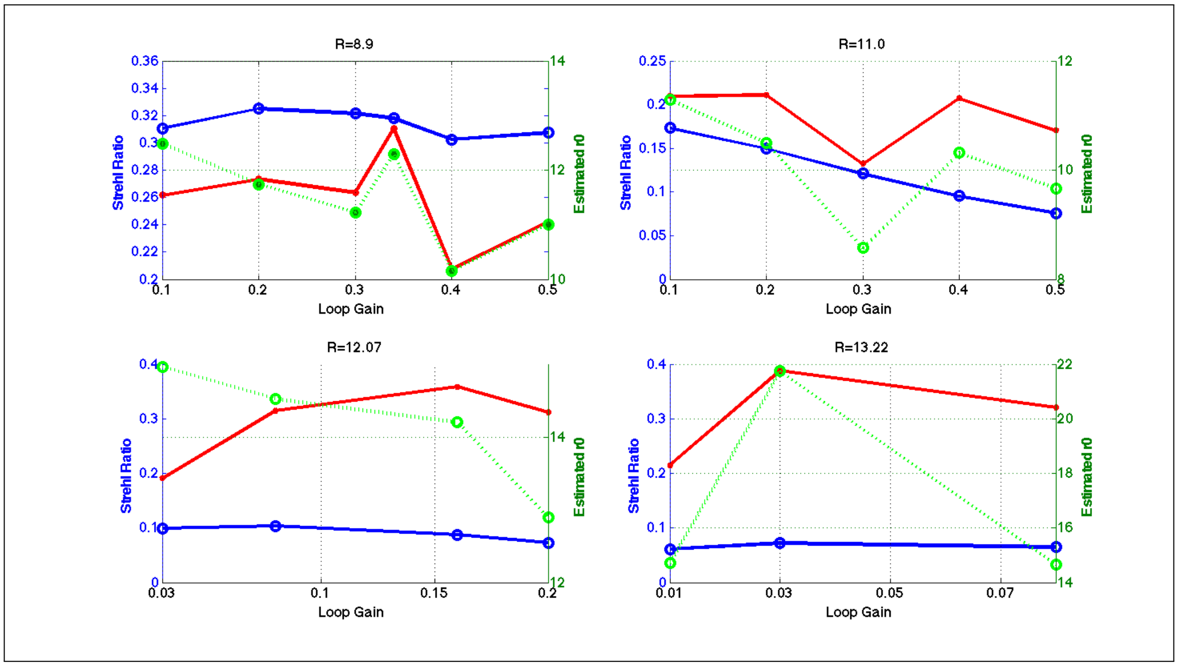

FIGURE 4.36. r_0 estimation (green, right y axis), Sky PSF Strehl (blue) and estimated PSF strehl(red) as function of the loop gain.

4.6.7. PSF reconstruction using V_{ii} algorithm

On Gendron et al. (2006), it was proposed an alternative algorithm to suppress the use of the U_{ij} functions derived from the DM modes and replace them with the V_{ii} functions that are obtained from the diagonalization of the residual parallel phase covariance matrix. This algorithm was explained with detail in section 3.2.8 and was implemented in APETy.

Figure 4.37 presents the relationship between the Strehl, FWHM and EE50 obtained using the U_{ij} method and the V_{ii} method. It can be seen that the results obtained with the V_{ii} algorithm are identical to the results obtained with the U_{ij} functions. In table 4.3 the PSF parameters are presented for both U_{ij} and V_{ii} algorithm.

Regarding the execution time, the U_{ij} algorithm takes in average 260 seconds to complete the PSF reconstruction for NICI. The V_{ii} algorithm is almost 4 times faster completing the PSF reconstruction (70 seconds in average). As reference APETy was implemented in a computer with a processor speed of 2.4 GHz and 10 GB of RAM. The speed of the algorithm is mainly limited by the speed of the processor.

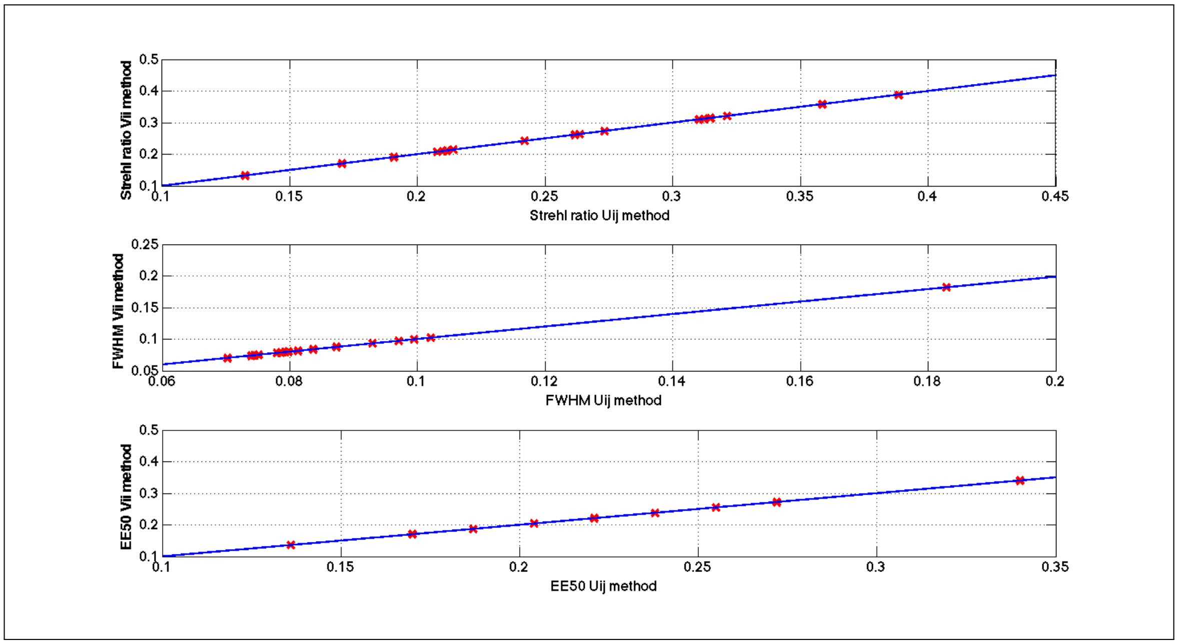

FIGURE 4.37. Comparison for PSF estimated with U_{ij} method and V_{ii} method.

4.6.8. Non-Common path aberrations

The calibration of the telescope PSF through the measurement of the static aberrations and the calibration of the AO system through the measurement of the non-common path aberrations are an important step to obtain accurate estimations of the PSF that allows for photometry and astrometry as it has been reported in Jolissaint et al. (2011). For this study the telescope static aberrations was not available. However, an static image of NICI internal PSF taken with the Fiber Optics Calibration system (FOCS) will help to the purpose of introducing the effect of non-common path aberrations in the PSF estimation. Unfortunately, this image was acquired in the context of a focus characterization study, so it has Strehl ratio of 46.65% and a FWHM of 110.24 mili-arcseconds, thus it is not properly calibrated for PSF reconstruction. However, it will be useful as reference to watch the effects of non-common path aberrations in the deconvolution with the sky PSF.

Only the cases indicated in table 4.4 were tested for the static aberrations. Table 4.7 present the results after the inclusion of NICI internal PSF. In general, the estimation error increased for all the parameter in all the cases.

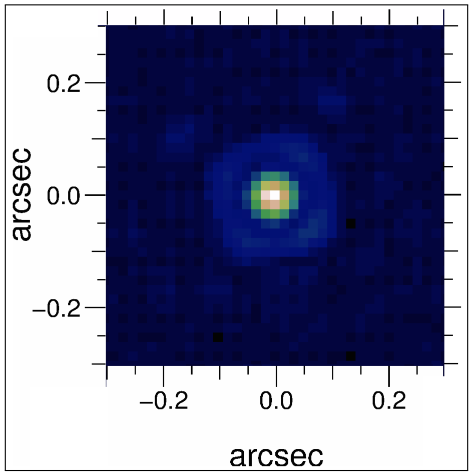

FIGURE 4.38. Static PSF acquired with FOCS.

TABLE 4.7. PSF reconstruction including non-common path aberrations.

R Magnitude	Loop Gain		Real PSF	Estimated PSF	PSF with aberrations
8.9	0.34	Strehl Ratio (%)	31.79	29.41	40.11
		FWHM (mili-arcsec)	57.91	70.25	167.47
		Encircled Energy 50% (mili-arcsec)	203.97	170.00	118.98
11.0	0.3	Strehl Ratio (%)	12.12	11.89	32.97
		FWHM (mili-arcsec)	122.33	97.04	188.43
		Encircled Energy 50% (mili-arcsec)	322.95	339.94	118.98
12.07	0.03	Strehl Ratio (%)	9.94	16.16	41.08
		FWHM (mili-arcsec)	83.95	99.50	165.35
		Encircled Energy 50% (mili-arcsec)	577.90	203.97	118.98
13.22	0.01	Strehl Ratio (%)	6.14	11.48	40.76
		FWHM (mili-arcsec)	110.57	182.85	166.36
		Encircled Energy 50% (mili-arcsec)	815.86	203.97	118.98

It was found that when the estimated PSF is used to deconvolve the sky PSF with the Lucy-Richardson algorithm, the algorithm has a faster convergence and can degenerate the image into a single pixel point. This suggest that the estimated PSF is closer to the sky PSF in terms of remanent speckles and other PSF artifacts that are not reproduced by the PSF estimation without non-common path aberrations.

In figure 4.39, the estimated PSF and the deconvolved image are shown for the bright star case (R=8.9) and the faint star case (R=12.07). For R=8.9, figure 4.39b, shows that the companion appearing in figure 4.25d has vanished and the star appears surrounded by small remnants of noise. For R=12.07, the deconvolved image in 4.31d has now an uniform background, as can be seen in figure 4.39d.

Table 4.8 summarizes the FWHM value for the images deconvolved using static aberrations. It can be seen that the FWHM is worse than the free aberrations case, but it takes the result closer to the diffraction limited image. These examples show that the blurred sky image can be improved by the deconvolution, but not having a properly calibrated image purposely acquired for PSF reconstruction, will not allow to get acceptable accuracy for photometry and astrometry.

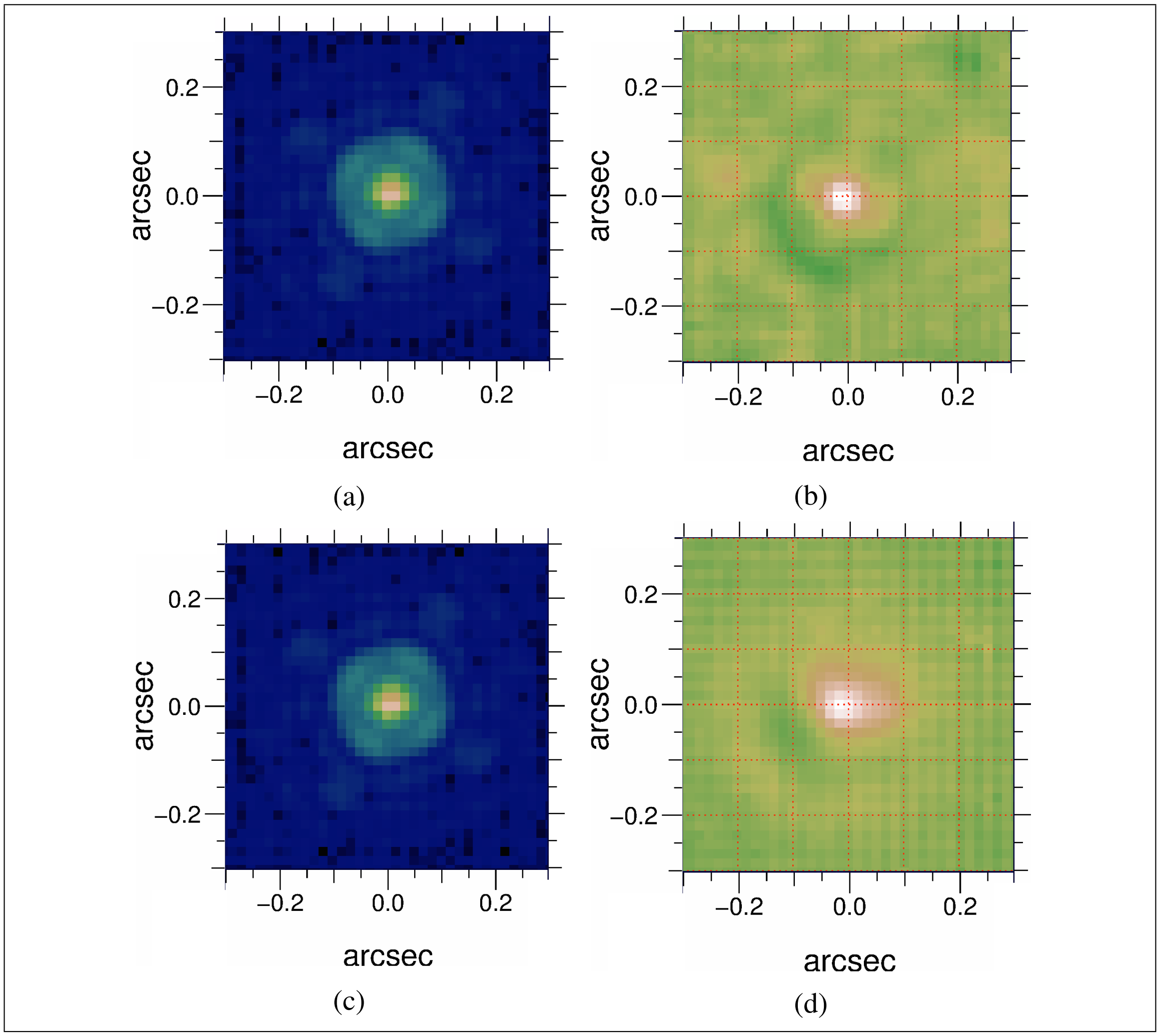

FIGURE 4.39. PSF reconstruction using non-common path aberrations. (a) Estimated PSF with non-common path aberrations for R=8.9. (b) Image deconvolution for R=8.9. (c) Estimated PSF with non-common path aberrations for R=12.07. (d) Image deconvolution for R=12.07.

TABLE 4.8. FWHM for deconvolved images with non-common path aberrations.

	Telescope (non-common path aberrations) [mili-arcsec]	Magnitude R=8.9 [mili-arcsec]	Magnitude R=11.0 [mili-arcsec]	Magnitude R=12.07 [mili-arcsec]	Magnitude R=13.22 [mili-arcsec]
FWHM	110.24	54.95	77.44	66.62	91.89

5. CONCLUSION AND FUTURE RESEARCH

5.1. Review of the Results and General Remarks

As can be seen on the PSF reconstruction survey chapter, implementation of PSF reconstruction using AO telemetry data is a technique that has a few number of successful cases using on-sky data. For this study, PSF reconstruction was attempted on NICI using APETy and on-sky data. The results presented in this thesis indicate that estimation of the long exposure PSF based on NICI AO telemetry data is feasible for bright stars ($R \leq 11.0$) with accuracies similar to those predicted in the literature (Strehl error $\sim 5\%$). For faint stars, the PSF reconstruction fails with considerable error level in all the PSF parameters (Strehl, FWHM, EE50). This behavior is also reported in the literature and is related to the dominance of noise in the WFS measurements and the AO loop bandwidth. For faint stars, both loop gain and loop frequency have to be adjusted (Jolissaint et al., 2012).

It is necessary to recall that the datasets provided to implement the PSF reconstruction were obtained during an AO loop gain characterization campaign. Therefore it is possible that the NICI system was not completely optimized for astronomical observations.

Unfortunately, due to time availability and weather conditions, obtaining astronomical data and AO circular buffers specially for PSF reconstruction was not possible. To completely explain the causes of the PSF reconstruction failure, it is necessary to carry out a dedicated campaign for this objective, in order to attain a complete characterization of the system.

Estimation of the seeing or Fried's parameter, r_0, via the DM commands was in good agreement with DIMM measurements and estimations from Gemini quality image software. It has been seen that the r_0 estimation is influenced by the loop gain that tends to over-estimated this value for faint sources. A good knowledge of the characteristics might provide solutions to counteract these error sources.

A key aspect in the PSF reconstruction implementation is the use of Montecarlo simulations. Firstly to predict the performance of the algorithm and secondly, to determine the high order phase contribution of the system. The structure function of the orthogonal phase $D_{\phi\perp}$, and the structure function of the aliasing effect are determined by simulations and are used to determinate of the turbulent OTF. As was reported in the results of Hartung et al. (2011), having an accurate model of the high order phase, or equivalently knowing the spatial cut-off frequency of the system, is critical for a successful PSF reconstruction. In this thesis, the spatial cut-off frequency was estimated by analysis of the WFS spatial frequency response. The high order phase contributions were evaluated using phase screens filtered to the spatial cut-off frequency. It was found that the high order phase contribution has a dependence on the loop gain, thus for every loop gain a Montecarlo simulation is needed. Although, simulations are time consuming, they need to be done once.

5.2. Evaluation of the Solution

From the survey chapter we know that the results obtained with APETy are close to other successful cases for bright stars. For the Fried's parameter estimation, a good agreement with DIMM and Gemini image quality software was found.

Inside the APETy implementation, the use of filtered phase screens allowed to remove the error in the base case for simulations. The original method used by APETy, determined the high order phase by subtraction of the projection of the corrected phase in the residual error phase. The use of filtered phase screens allowed to reduce the time to obtain the high order contributions by 50% (1 hour per 1000 AO loop iterations). The time required for simulations is mainly limited by the speed of the processor, thus alternatives as the use of parallel computing should be considered in order to reduce the required time.

APETy included implementations for PSF estimation using the U_{ij} and V_{ii} methods. It was found that both techniques provide the same results, but the V_{ii} method is almost 4 times faster.

Inclusion of the non-common path aberrations or static aberrations have a significative impact in the estimated PSF and in the quality of the deconvolved image. It was seen that including non-common path aberrations removed artifacts in the deconvolved image.

However, as the telescope PSF was not calibrated, the accuracy of the image for astrometry and photometry is not reliable.

5.3. Future Research

PSF Reconstruction is a complex task that requires a full and deep characterization of the telescope and the AO system, a rigorous system modeling and extensive simulations. Among future topics for future work, it is suggested to:

- Characterization of AO systems in order to implement PSF reconstruction for faint stars.
- Define parameters to compensate for AO loop gain and star magnitude influence in the estimation of r_0.
- Study of techniques to determine static aberrations and non-common path for improvement in the PSF estimation.

For future developments of PSF reconstruction algorithms, the efforts should be oriented to wide field AO systems for ELTs, where the main problems to solve will be related to the big amount of data to process because of the increased number of actuators in the new AO systems. For the case of study in this thesis (NICI), the 85x85 control matrices and 3570 U_{ij} functions occupied 10 gigabytes of storage. In an ELT, matrices will grow to the order of 1000 x 1000 and U_{ij} functions will be about 500,000, meaning approximately 1.4 Terabytes and a huge calculation time. Therefore, optimized versions of the algorithm, as the V_{ij} functions approach, will be needed in order to reduce the time needed for simulations in this the next generation of telescopes. Then, on the topics for future research it can be mentioned:

- Implement AO system simulations and PSF reconstruction algorithm using GPU.
- Pursue PSF reconstruction development using the V_{ii} method.
- Continuing research on PSF reconstruction algorithm for wide field AO.

REFERENCES

Allen, R. L., & Mills, D. W. (2004). *Signal Analysis: Time, Frequency, Scale, and Structure* (1^{st} ed.). Piscataway, NJ: Wiley-IEEE Press.

Andersen, T., & Enmark, A. (2011). *Integrated Modeling of Telescopes* (1^{st} ed.). New York, USA: Springer.

Andrews, L. C. (2004). *Field Guide to Atmospheric Optics* (1^{st} ed.). Bellingham, Washington: SPIE Press.

Andrews, L. C., & Phillips, R. L. (2005). *Laser Beam Propagation Through Random Media* (1^{st} ed.). Bellingham, Washington: SPIE press.

Artigau, E., Biller, B. A., Wahhaj, Z., Hartung, M., Hayward, T., Close, L. M., et al. (2008). NICI: Combining Coronagraphy, ADI, and SDI. In *Proc. SPIE* (Vol. v. 7014 - Ground-based and Airborne Instrumentation for Astronomy I).

Born, M., & Wolf, E. (1970). *Principles of Optics* (4^{th} ed.). Cambridge: Cambridge University Press.

Britton, M. C. (2006). The Anisoplanatic Point-Spread Function in Adaptive Optics. *Publications of the Astronomical Society of the Pacific*, *v. 118*, 885–900.

Clénet, Y., Kasper, M., Gendron, E., Fusco, T., Rousset, G., Gratadour, D., et al. (2006). PSF Reconstruction for NAOS-CONICA. In *SPIE conference series* (Vol. v. 6272 - Advances in adaptive optics).

Clénet, Y., Lidman, C., Gendron, E., Rousset, G., Fusco, T., Kornweibel, N., et al. (2008). Tests of the PSF Reconstruction Algorithm for NACO/VLT. In *Proc. SPIE* (Vol. v. 7015 - Adaptive Optics Systems).

Connors, T. W. (2008). *Dome Air Conditioning Effects on the Seeing as a Function of the Mirror, Dome and External Temperatures and Weather Conditions* (Report). Australian Astronomical Observatory.

Costille, A. (2009). *Les Optiques Adaptatives Grand Champ: Stratégie de Correction et Validations Expérimentales*. Unpublished doctoral dissertation, Université Paris Diderot (Paris 7), Paris, France.

Ersoy, O. K. (2007). *Diffraction, Fourier optics and imaging* (1^{st} ed.). Hoboken, New Jersey: Wiley.

Exposito, J., Gratadour, D., Rousset, G., Clénet, Y., Gendron, E., & Mugnier, L. (2013). A New Method For Adaptive Optics Point-Spread Function Reconstruction. In *Proceedings of AO4ELT3*.

Fitzgerald, M. (2004). *Status of PSF Reconstruction at Lick Observatory for Workshop on AO PSF Reconstruction* (report). Lick Observatory.

Flicker, R., & Rigaut, F. (2001). Tilt Anisoplanatism and PSF Retrieval for a Multi-Conjugated Adaptive Optics System using Laser Guide Stars. In *proceedings of Beyond conventional adaptive optics conference, Venice.*

Flicker, R., Rigaut, F. J., & Ellerbroek, B. L. (2003). Tilt Anisoplanatism in Laser Guide Star based Multi-Conjugate Adaptive Optics: Reconstruction of the Long Exposure Point-Spread Function from Control Loop Data. *Astronomy & Astrophysics*, *v. 400*, 1199–1207.

Gal, R., Kiryati, N., & Sochen, N. (2014). Progress in the Restoration of Image Sequences Degraded by Atmospheric Turbulence. *Pattern Recognition Letters*.

Gendron, E., Clénet, Y., Fusco, T., & Rousset, G. (2006). New Algorithms for Adaptive Optics Point-Spread Function Reconstruction. *Astronomy & Astrophysics*, *v. 457*(n. 1), 359–363.

Gendron, E., & Lena, P. (1994). Astronomical Adaptive Optics. 1: Modal Control Optimization. *Astronomy & Astrophysics*, *v. 94*(n. 1), 337–347.

Gendron, E., Vidal, F., Brangier, M., Morris, T., Hubert, Z., Basden, A., et al. (2011). MOAO First On-Sky Demonstration with CANARY. *Astronomy & Astrophysics*, *v. 529*, L2.

Gilles, L., B.Neichel, J.P.Véran, & Ellerbroek, B. (2013). Point-Spread Function Reconstruction on the Gemini Canopus Bench. In *Proceedings of AO4ELT3*.

Gilles, L., Correia, C., Veran, J., Wang, L., & Ellerbroek, B. (2012). Tip/Tilt Point Spread Function Reconstruction for Laser Guide Star Multi-Conjugate Adaptive Optics. In *Proc. SPIE* (Vol. v. 8447 - Adaptive Optics Systems III).

Gladysz, S., Louarn, M. L., N, Y., Garcia-Rissmann, A., Kann, L., Drummond, J. D., et al. (2012). Size of the Halo of the Adaptive Optics PSF. In *Proc. SPIE,* (Vol. v. 8447 - Adaptive Optics Systems III).

Glindeman, A. (2011). *Principles of Stellar Interferometry* (1^{st} ed.). Berlin Heidelberg: Springer.

Glindemann, A., Hippler, S., Berkefeld, T., & Hackenberg, W. (2000). Adaptive Optics on Large Telescopes. *Experimental Astronomy*, *v. 10*, 5–47.

Goodman, J. W. (2005). *Introduction to Fourier Optics* (3^{rd} ed.). Englewood, Colorado: Roberts.

Harder, S., & Chelli, A. (2000). Estimating the Point Spread Function of the Adaptive Optics System ADONIS using the Wavefront Sensor Measurements. *Astronomy & Astrophysics*, *v. 142*(n. 1), 119–135.

Hartung, M., Gratadour, D., Chun, M., & Hayward, T. (2011). The PSF Reconstruction Effort for NICI, the High-Contrast Coronagraphic Imager of Gemini Observatory: a snapshot. In *Proceedings of AO4ELT2.*

Hespanha, J. P. (2009). *Linear Systems Theory* (1^{st} ed.). Princeton, NJ: Princeton University Press.

Hinnen, K. J. G. (1997). *Data-Driven Optimal Control for Adaptive Optics*. Unpublished doctoral dissertation, Technische Universiteit Delft, Netherlands.

Jacoby, G. H., Bouchez, A., Colless, M., DePoy, D., Fabricant, D., Hinz, P., et al. (2012). The Instrument Development and Selection Process for the Giant Magellan Telescope. In *Proc. SPIE* (Vol. v. 8446 - Ground-based and Airborne Instrumentation for Astronomy IV).

Johns, M., McCarthy, P., Raybould, K., Bouchez, A., Farahani, A., Filgueira, J., et al. (2012). Giant Magellan Telescope: overview. In *Proc. SPIE* (Vol. v. 8444 - Ground-based and Airborne Telescopes IV).

Jolissaint, L., Carfantan, H., & Anterrieu, E. (2008). Exploring the Impact of PSF Reconstruction Errors on the Reduction of Astronomical Adaptive Optics Based Data. In *Proceedings of the SPIE* (Vol. v. 7015 - adaptive optics systems).

Jolissaint, L., Neyman, C., Christou, J., Mugnier, L., & Wizinowich, P. (2011). First Successful Adaptive Optics PSF Reconstruction at W. M. Keck Observatory. In *Proceedings of AO4ELT2*.

Jolissaint, L., Neyman, C., Christou, J., & Wizinowich, P. (2012). Adaptive Optics Point-Spread Function Reconstruction Project at W.M. Keck Observatory : First Results with Faint Natural Guide Stars. In *Proceedings of the SPIE* (Vol. v. 8447 - Adaptive Optics Systems III).

Jolissaint, L., Véran, J. P., & J.Marino. (2004). OPERA, an Automatic PSF Reconstruction Software for Shack-Hartmann AO systems: application to Altair. In *Proc. SPIE* (Vol. v. 5490 - Advancements in Adaptive Optics, pp. 151–163).

Kenyon, I. R. (2008). *The Light Fantastic, A Modern Introduction to Classical and Quantum Optics* (1^{st} ed.). Oxford, UK: Oxford University Press.

Keskin, O., Conan, R., & Bradley, C. (2006). Point Spread-Function Reconstruction from Woofer-Tweeter Adaptive Optics Bench. In *SPIE conference series* (Vol. v. 6272 - Advances in adaptive optics).

Kolmogorov, A. N. (1941). The Local Structure of Turbulence in Incompressible Viscous Fluid for Very Large Reynolds' Numbers. In *Doki. acad. sci. ussr* (Vol. v. 30, pp. 301–305).

Lawson, P. R. (2000). *Principles of Long Baseline Stellar Interferometry: course notes from the 1999 Michelson Summer School* (1^{st} ed.). New York, USA: National Aeronautics and Space Administration, Jet Propulsion Laboratory, California Institute of Technology.

Liske, J., Padovani, P., & Kissler-Patig, M. (2012). Science with the re-baselined European Extremely Large Telescope. In *Proc. SPIE* (Vol. v. 8444 - Ground-based and Airborne Telescopes IV).

Lloyd-Hart, M., & Milton, N. (2003). Fundamental Limits on Isoplanatic Correction with Multiconjugate Adaptive Optics. *Journal of the Optical Society of America*, *v. 20*(n. 10), 1949–1957.

Noll, R. J. (1976). Zernike Polinomials and Atmospheric Turbulence. *Journal of the Optical Society of America*, *v. 66*(n. 3), 207–211.

Obukhov, A. M. (1949). Structure of the Temperature Field in a Turbulent Flow. *Izv. Akad. Nauk SSSR, Geographical and Geophysical Ser.*, *13*, 58–69.

Perryman, M., Hainaut, O., Dravins, D., Leger, A., Quirrenbach, A., Rauer, H., et al. (2005). *Report by the ESA-ESO Working Group on Extra-Solar Planets* (Tech. Rep.). European Space Agency.

Peter, D., & Gässler, W. (2010). Point-Spread Function Reconstruction for the Ground Layer Adaptive Optics System ARGOS. In *Proc. SPIE* (Vol. v. 7736 - Adaptive Optics Systems II).

Roddier, F. (1981). The Effects of Atmospheric Turbulence in Optical Astronomy. *Progress in optics. Volume 19. Amsterdam, North-Holland Publishing Co.*, *v. 19*, 281–376.

Roddier, F. (1999). *Adaptive Optics in Astronomy* (1^{st} ed.). Cambridge, UK: Cambridge University Press.

Schmidt, J. D. (2010). *Numerical Simulation of Optical Wave Propagation with Examples in MATLAB* (1^{st} ed.). Bellingham, Washington: SPIE Press.

Schodel, R., Yelda, S., Ghez, A., Girard, J., Labadie, L., Rebolo, R., et al. (2013). Holographic Imaging of Crowded Fields: High Angular Resolution Imaging with Excellent Quality at Very Low Cost. *Monthly Notices of the Royal Astronomical Society*, *v. 429*, 1367.

Sheehy, C. D., McCrady, N., & Graham, J. R. (2006). Constraining the Adaptive Optics Point-Spread Function in Crowded Fields: Measuring Photometric Aperture Corrections. *The Astrophysical Journal*, *v. 647*, 1517–1530.

Simard, L., Crampton, D., Ellerbroek, B., & Boyer, C. (2012). The Instrumentation Program for the Thirty Meter Telescope. In *Proc. SPIE* (Vol. v. 8446 - Ground-based and Airborne Instrumentation for Astronomy IV).

Stepp, L. (2012). Thirty Meter Telescope project update. In *Proc. SPIE* (Vol. v. 8444 - Ground-based and Airborne Telescopes IV).

Sweeney, D. W. (2012). Overview of the Large Synoptic Survey Telescope Project. In *Proc. SPIE* (Vol. v. 8446 - Ground-based and Airborne Instrumentation for Astronomy IV).

Tatarskii, V. I. (1968). *Wave Propagation in a Turbulent Medium* (1^{st} ed.). Michigan: Dover.

Tian, Y., Rao, C., & Wei, K. (2009). Adaptive Optics Image Restoration Based on Frame Selection and Multi-frame Blind Deconvolution. *Chinese Astronomy and Astrophysics*, *v. 33*(n. 2), 223–230.

Tokovinin, A., & Kornilov, V. (2007). Accurate Seeing Measurements with MASS and DIMM. *Monthly Notices of the Royal Astronomical Society*, *v. 381*(n. 3), 1179–1189.

Tyler, D. W. (2001). Deconvolution of Adaptive Optics Image Data. In *Proceedings of the center for adaptive optics.*

Tyson, R. K. (2000). *Introduction to Adaptive Optics* (1^{st} ed.). Bellingham, Washington: SPIE press.

Vazquez, M., Palle, E., & Rodriguez, P. M. (2010). *The Earth as a Distant Planet : A Rosetta Stone for the Search of Earth-Like Worlds* (1^{st} ed.). New York: Springer.

Véran, J. (2001). *MCAO PSF Reconstruction* (Report). Herzberg Institute of Astrophysics, National Research Council of Canada.

Véran, J., Rigaut, F., Maître, H., & Rouan, D. (1997). Estimation of the Adaptive Optics Long Exposure Point-Spread Function using Control Loop Data. *Journal of the Optical Society of America*, *A 14*, 3057–3069.

Villecroze, R., Fusco, T., Bacon, R., & Madec, P. (2012). PSF Reconstruction for MUSE in Wide Field Mode. In *Proc. SPIE* (Vol. v.v8447 - Adaptive Optics Systems III).

Wang, J. Y., & Markey, J. K. (1978). Modal Compensation of Atmospheric Turbulence Phase Distortion. *Journal of the Optical Society of America*, *v. 68*(n. 1), 78–87.

Weiss, R. (2003). *Point-Spread Function Reconstruction for the Adaptive Optics System ALFA and its Application to Photometry*. Unpublished doctoral dissertation, Combined Faculties for the Natural Sciences and for Mathematics, Ruperto-Carola University of Heidelberg, Stuttgart, Germany.

Williams, C., & Becklund, O. A. (1989). *Introduction to the Optical Transfer Function* (1^{st} ed.). Bellingham, Washington: SPIE Press.